

Predicting Wind Noise Inside Porous Dome Filters for Infrasound Sensing on Mars

A Thesis

Presented to the

Graduate Faculty of the

University of Louisiana at Lafayette

In Partial Fulfillment of the

Requirements for the Degree

Masters of Science

Kevin M. Pitre

Fall 2016

ProQuest Number: 10244134

All rights reserved

INFORMATION TO ALL USERS

The quality of this reproduction is dependent upon the quality of the copy submitted.

In the unlikely event that the author did not send a complete manuscript and there are missing pages, these will be noted. Also, if material had to be removed, a note will indicate the deletion.



ProQuest 10244134

Published by ProQuest LLC (2017). Copyright of the Dissertation is held by the Author.

All rights reserved.

This work is protected against unauthorized copying under Title 17, United States Code
Microform Edition © ProQuest LLC.

ProQuest LLC.
789 East Eisenhower Parkway
P.O. Box 1346
Ann Arbor, MI 48106 – 1346

© Kevin M. Pitre

2016

All Rights Reserved

Predicting Wind Noise Inside Porous Dome Filters for Infrasound Sensing on Mars

Kevin M. Pitre

APPROVED:

Andi Petculescu, Chair
Associate Professor of Physics

Gabriela Petculescu
Associate Professor of Physics

Natalia A. Sidorovskaia
Professor and Head of Physics

Mary Farmer-Kaiser
Dean of the Graduate School

Dedication

This work is dedicated to my wife, Jodie, and parents, Louis and Monica.

Acknowledgments

I would like to give my most sincere gratitude to my research advisor and mentor, Dr. Andi Petculescu, for his guidance and assistance throughout my graduate studies. He has helped me to become a better researcher. Also, along the way, he has provided me with the proper foundational knowledge and technical assistance to gain a deeper physical understanding of my studies.

I am also thankful for all the time and efforts from the other members of my committee, Dr. Gabriela Petculescu and Dr. Natalia Sidorovskaia, who not only oversaw both my writing and research efforts but provided other invaluable knowledge through coursework I utilized on a daily basis in my research work.

I am grateful for the additional financial support provided by the Louisiana Space Consortium through the Graduate Student Research Assistance Program. Through their assistance, I was more easily able to pursue research in a particular area of interest of mine: space and aerospace related research.

Finally, I wish to convey a profound appreciation to my wife and my parents, to whom this work is dedicated, for their patience and their support of my decisions throughout life and academia. Without them, my journey would not be as pleasant or easy. I am also thankful for all close friends and family, who provided moments of moderation and support during the pursuit of my academic goals.

Table of Contents

Dedication	iv
Acknowledgements	v
List of Figures	vii
List of Tables	viii
List of Abbreviations and Mathematical Symbols	ix
Chapter 1: Introduction	1
Literature Review	9
Chapter 2: Derivation of Power Spectral Density for Region 3	10
Derivation of PSD for Region 1	19
Derivation of PSD for Region 2	21
Chapter 3: Methods for Determining Region Coefficients	25
Region 3 Parameters	28
Region 1 Parameters	31
Region 2 Parameters	33
Chapter 4: Results of Power Spectral Density Predictions	34
Chapter 5: Discussion and Conclusion	41
Bibliography	49
Appendix	53
ABSTRACT	98
Biographical Sketch	100

List of Figures

Figure 1.1 Energy contained within eddies as a function of wavenumber	5
Figure 1.2 Visual representation of the three regions of turbulence interactions	7
Figure 2.1 Reference coordinate system.....	12
Figure 3.1 An example of wind speeds from 0 to 10 meter altitudes throughout a 25 hour Martian day generated for Region 3 at the Pathfinder location. Here velocity is maximum at the 16 th hour of the day and minimum at roughly the 21 st hour	27
Figure 3.2 Wind speed at the Pathfinder location 10 meters over a 25 hour Martian day. Data points are averaged to determine a mean wind velocity V_{α} for Region 3. The same process is applied at 1 meter for Regions 1 and 2	27
Figure 3.3 Maximum and minimum velocity profile fits to data points for Curiosity, Pathfinder, Phoenix, Viking Lander 1, and Viking Lander 2	29
Figure 4.1 Velocity as a function of time and height above Martian surface modeled at each mission location over a 25 hour Martian day	34
Figure 4.2 Power Spectral Density predictions of noise floor for Curiosity landing site with maximum velocity predictions utilized for fitting the velocity gradient	37
Figure 4.3 Comparisons of total wind noise contributions at center of domes of varying porosities	40

List of Tables

Table 3.1 Fit parameters a and z_0 (meters) for Region 3 $V(z)$	30
Table 3.2 Average flow velocity in Region 3 at 10 meters over one Martian day	30
Table 3.3 Fit parameters to measure velocity spectrums on Earth	31
Table 3.4 Values of v_0 calculated for varying porosities of filter and max/min wind conditions per mission	32
Table 3.5 Fit parameters for Region 1 PSD velocity profiles measured by Abbott	32
Table 3.6 Parameters for Regions 1 and 2 calculations	33
Table 4.1 GPS coordinates for each mission	34

List of Abbreviations and Mathematical Symbols

*	Denotes correlated quantity
η	Dissipation length (meters)
$\partial_t \equiv \partial/\partial t$	Partial derivative with respect to time
$\partial_i \equiv \partial/\partial x_i$	Partial derivative with respect to direction
f	Frequency (Hertz or s^{-1})
g	Acceleration due to gravity (m/s^2)
GCM	General Circulation Model
k, \vec{k}	Wavenumber and vector respectively (m^{-1})
$\kappa, \vec{\kappa}$	2-D wavenumber and vector respectively, parallel to surface of Mars
λ	Fit parameter to von Kármán spectrum
MCD	Mars Climate Database
N	Brunt-Väisälä frequency
$\vec{\nabla}$	Gradient operator
∇^2	Laplacian operator
ω	Frequency ($2\pi \cdot \text{Hz}$ or $2\pi \cdot s^{-1}$)
Ω	Solid angle
p	Total pressure (Pa)
p_1	Fluctuating pressure (Pa)
P	Mean pressure (Pa)

PBL	Planetary Boundary Layer
PSD	Power Spectral Density ($\text{Pa}^2 \cdot \text{s}$)
R1, R2, R3	Regions within vicinity of dome filter
\vec{r}	Radial distance
ρ	Air density (kg/m^3)
R	Radius of filter (meters)
Ri	Richardson Number
Σ	Summation
ϑ	Kinematic viscosity (m^2/s)
T-S	Turbulence-shear interaction
T-T	Turbulence-turbulence interaction
T-F	Turbulence-filter interaction
t	Time (s)
τ	Correlation time (s)
\sim	Denotes Fourier transformed value
\vec{v}	Total velocity (m/s)
\vec{v}_1	Fluctuating velocity (m/s)
\vec{V}	Mean velocity (m/s)
V_α	Wind velocity in region $\alpha = 1,2,3$
v_0	Fit to velocity profile for Region 1
z	Height above surface (meters)
z_0	Roughness length (meters)

Chapter 1: Introduction

Infrasound covers the acoustic frequency spectrum below ~20 Hz. Because of long wavelengths, infrasonic waves in the atmosphere can travel over vast distances (~1000 km) with relatively small attenuation. Properties of infrasound signals such as absorption, dispersion, and direction of propagation contain information on both acoustic wave generation mechanisms and the propagation medium. On Earth, they have been studied extensively in the context of quantifying the various sources of infrasound such as bolide impacts and/or airbursts, lightning, strong storms, tornados, volcanos, earthquakes, ordnance explosions and nuclear testing (Walker 2010). Furthermore, they are considered as a potential tool for assessing the thermodynamics of the stratosphere and lower-thermosphere by studying arrivals from temperature inversion layers (de Groot-Hedlin et al. 2010).

The present study addresses infrasound in the atmosphere of Mars. Potential uses of infrasound measurements in the Martian atmosphere include locating and quantifying bolide impacts, monitoring subsurface activity, and studying the dynamics of dust storms and dust devils. Thus, infrasonic sensing would complement the array of instruments needed for a projected manned mission to the planet.

Infrasound measurements are hampered by noise, the most prevalent of which is that generated by wind blowing in the vicinity of the sensor (Walker 2010). The exact mechanisms of wind-generated infrasonic noise are still being investigated. Nevertheless, theoretical, computational, and experimental efforts point to an explanation of wind noise as turbulence interactions causing pressure fluctuations in the same frequency range as – albeit

incoherent with – the actual infrasonic signals arriving from a remote source. Thus, the justification of this study is the unavoidable infrasonic wind noise produced by turbulence in the Martian environment. Once these contributions are known/predicted, they can simply be subtracted from the spectrum of the received “raw” signal, leaving the pure infrasonic signal. This work could serve as preliminary framework to guide the development of future infrasonic sensors for the Martian environment. Turbulent wind noise is examined within the Martian planetary boundary layer (PBL) only. This is where turbulent eddies that are the sources of this noise are primarily located. There is no hard definition as to where a planet’s boundary layer ends. Boundary layers begin at the surface, and they are generally defined as ending at the first temperature inversion in the atmosphere. For Mars, the planetary boundary layer is defined as the lowest 1 to 10 kilometers of its atmosphere (Petrosyan 2011). Inside the PBL, the thermal balance is determined by heat released from the surface in the presence of turbulent eddies formed from convective mixing. Often, studies break the boundary layer down even further into multiple sections such as the surface layer, the mixed layer, and the entrainment zone (Petrosyan 2011). The surface layer is defined by $z/h \leq 0.1$, where z is the upward vertical coordinate examined and h is the height of the boundary layer. Located above the surface layer is the bulk or mixed layer formed by a sharp increase in potential temperature $\Delta\theta$ toward the free atmosphere. The entrainment zone pulls air downward from the free atmosphere above as mixing from below rapidly decays (Petrosyan 2011). This entrainment mechanism generates eddies of sizes that are large enough not to be dissipated by viscosity. This turbulent mixing arises from the combined effect of two main processes: the first process involves the buoyancy force from an upward moving heat flux released by the planet’s surface while the second process is a shearing effect from vertical wind velocity

gradients in opposing horizontal directions. These two sources of turbulent generation are often at odds with one another as to which plays the major role in eddy formation. One way to observe these sources and how turbulence is generated from them is through use of the dimensionless Richardson number (Ri), representing the ratio of buoyancy to shear effects. The buoyancy term is represented by temperature gradients through the Brunt-Väisälä frequency (N) while the shear effects are presented through average vertical gradients of the wind speed. The Brunt- Väisälä frequency is defined as

$$N = \sqrt{g\beta \frac{\partial\theta}{\partial z}}.$$

where g is the acceleration due to gravity, β is the thermal expansion coefficient, and $\frac{\partial\theta}{\partial z}$ is the vertical gradient of the ambient potential temperature, which represents the degree of convective stability in the layer being examined. The mean vertical shear of the horizontal flow (S) is defined as the velocity gradient with respect to height above surface

$$S \equiv \frac{\partial V}{\partial z}. \tag{1}$$

Squaring the ratio of these two terms yields the Richardson number (Petrosyan 2011),

$$Ri = \frac{\left(g\beta \frac{\partial\theta}{\partial z}\right)}{\left(\frac{\partial V}{\partial z}\right)^2}.$$

The Ri number describes the rippling by shear and the smoothing by convective stability of the sheared layer. Small or negative values of Ri , correspond to weakly stable or unstable atmosphere and/or large velocity gradients; in these conditions turbulence is very likely through either of the two processes. Large or positive values of Ri , associated with higher stability and/or weak gradients, indicate intermittent turbulence. Turbulence often appears when the Richardson number falls below 0.25 (McIlveen 1992). For more stable conditions the only significant source of turbulence is that from the shear processes.

As for turbulence, no fixed definition exists. Instead, there are only general ways in which it is described. Panofsky and Dutton (Panofsky and Dutton 1984, p.5) describes turbulence in the following way:

1. The fluid velocity is chaotic and apparently random function of both space and time.
2. The flow is strongly rotational and three-dimensional, with gradients occurring in all directions.
3. Nonlinearity is essential to turbulence and responsible for energy being distributed smoothly with wavelength.
4. Gradients are created in the turbulent flow by the stretching of vortices, a process that moves kinetic energy to smaller wavelengths.
5. Turbulent flows are diffusive and intermittent.

Studies of turbulent flow involve a statistical treatment of fluctuating velocity gradients and shear stresses that describe the motion of these eddies. The velocity gradients can be inferred experimentally from direct measurements of the velocity fields using hot-wire or ultrasonic anemometers or, indirectly by detecting the fluctuating pressure (i.e. using microphones). The vortices or eddies are often viewed conceptually as three-dimensional swirling spheres of varying sizes. As these eddies interact, they break down in size. They lose kinetic energy in the process as the velocity gradients decrease in magnitude. This cascading process continues until eddies are small enough (on the order of molecular sizes) to dissipate

completely due to viscosity. The heat released from this dissipation process affects the surface temperature of the planet.

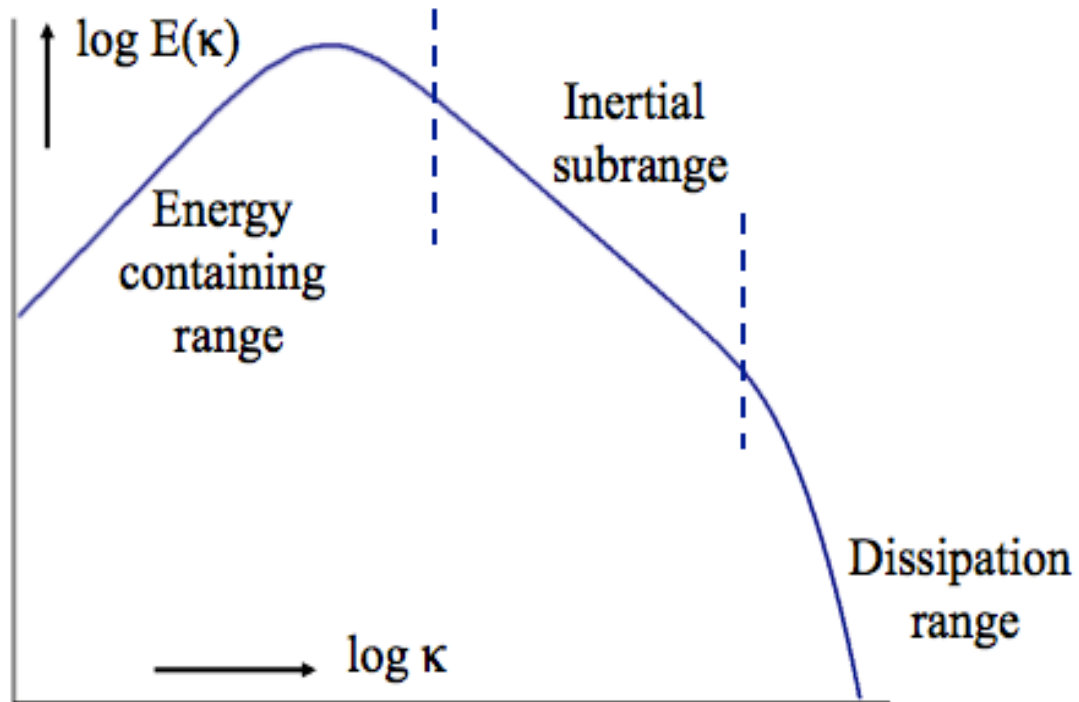


Figure 1.1. Energy contained within eddies as a function of wave number.

Figure 1.1 shows a typical spectrum of turbulence. Most of the turbulent energy is carried by the larger eddies, corresponding to the lowest wavenumbers (frequency) and forming the so-called “energy-containing range”. Mid-sized eddies make up the “inertial sub-range” while the smallest eddies, losing energy by molecular viscosity, form the “dissipation sub-range”, associated with high frequencies. In this study, large eddies will be on the scale of Mars’ boundary layer i.e. 1 to 10 kilometers, medium sized eddies will range from 1 meter up to 1 kilometer, and small eddies will consist of all sizes below 1 meter in diameter. A clever rhyme for describing this cascading process was created by English scientist Lewis

Richardson. The *Richardson Numbers*, relating turbulence and convective stability, are used to describe many atmospheric processes (Monin and Yaglom 1971). His rhyme reads:

*Big whorls have little whorls,
Which feed on their velocity;
And little whorls have lesser whorls,
And so on to viscosity
(in the molecular sense).*

The following study focuses on use of porous hemispherical dome filters. They are 2 meters in height and used to filter measured wind noise. After passing through the filter, theoretical pressure contributions will be plotted as a function of frequency within the infrasonic range. The idea for this research spawned from a report by Noble et al. (2014). In the report, researchers studied the effects of using dome filters to filter measured wind noise at infrasonic frequencies on Earth. Filters currently being used are mainly comprised of rosette and linear pipe array filters (Walker 2010). While these kinds of geometries have proven quite efficient on Earth, the problems associated with deploying and maintaining them in the Martian environment overcomes their operational benefits. Specifically, the problems with these filters are size, mobility, and set-up. Rosettes can range upwards of 70 meters in diameter leading to no mobility and requiring careful set-up. A linear pipe array, sometimes referred to as a Daniels filter, can range up to 600 meters in length and must be placed so that the open face is normal to the received sound wave for optimal performance (Walker 2010). Better space travel options are needed in lieu of current filters used on Earth. The dome filters could be constructed of lightweight material that would make them easily compactable, transportable, and effortlessly deployable. A simple example of this would be that of a “pop-up” tent surrounding the microphone, which could be designed to be autonomously deployable. These factors are all crucial for space travel and deployment on

another planet. The use of this filter will mitigate the magnitude and amount of pressure fluctuations read by a sensor located at ground level in the center of the dome. The filter will do this by homogenizing the flow inside its walls. The porosity of the dome will be varied throughout the analysis by 30%, 40%, 55%, 65%, and 80%. This percent represents the amount of open space of the material formed into the shape of our dome. The larger the porosity, the more flow allowed through the walls of the dome. In order to predict the net pressure power spectrum that would be measured at the center of the dome, the study will be divided into three regions, following the framework of Abbott and Raspert (2015) and Noble et al. (2014). Region 1 lies within the dome and away from any small boundary layer that forms along the wall of the dome. Region 2 describes interactions at the surface of the dome wall. Region 3 consists of the entire outside of the dome filter so that large scale eddies are mostly unaffected by the presence of the dome. The three regions are shown schematically in Figure 1.2.

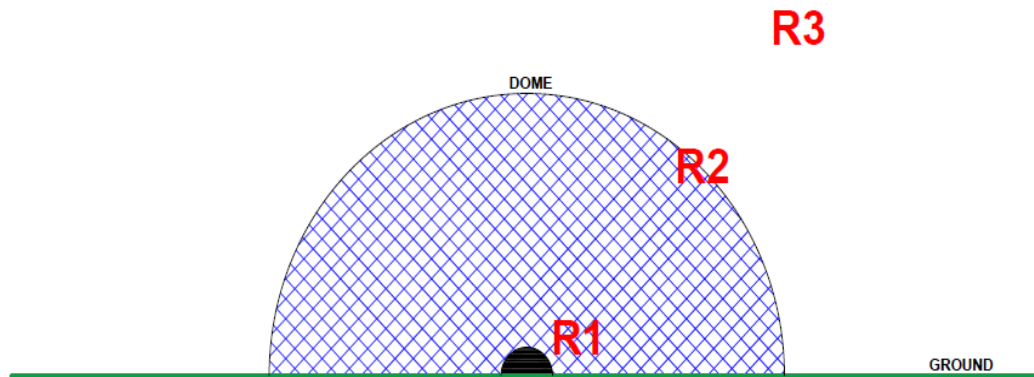


Figure 1.2. Visual representation of the three regions of turbulence interactions.

For predicting wind noise due to turbulence, we must first identify what physical mechanisms create these pressure fluctuations. During this process we acknowledge three different types of physical interactions that take part over the three regions of study.

The first type of interaction is one where turbulent eddies are distorted by the ambient wind velocity gradient. This mechanism is called “turbulence-mean-shear” interaction. This type of interaction dominates the energy containing sub-range denoted in Figure 1.1 (George 1984).

The second type of interaction is one in which turbulent eddies interact with each other. In this type of interaction, turbulent eddies can combine to become larger, pass through one another, or cause a dissipation of large eddies into smaller ones. This mechanism is termed “turbulence-turbulence” interaction and dominates the inertial sub-range in Figure 1.1 (George 1984). These two mechanisms comprise interactions experienced in a free atmosphere outside and unaffected by the dome filter.

The final type of interaction arises from the interaction of the fluctuating pressure field with the dome structure via the stagnation pressure (Raspert 2006). Turbulent eddies of sizes comparable to that of the filter create a fluctuating stagnation pressure normal to the surface of the dome. This fluctuating pressure has a buffeting effect on the structure. This buffeting effect can be explained as one similar to that experienced by placing a hand outside of a moving car window; the effect of increasing porosity on the flow past the hand is similar to that of gradually separating the fingers. This mechanism will be referred to as turbulence-filter interaction.

In the three regions denoted previously in Figure 1.2, we experience all three of these mechanisms for creating wind noise. Regions 1 and 3 are dominated by turbulence-turbulence and turbulence-shear interactions while Region 2 is where we experience turbulence-filter interaction. Equations for calculating pressure fluctuation contributions in these three regions are derived in the next chapters.

Literature Review

The initial catalyst behind the idea for the present study is gained from an article written for the Army Research Labs (Noble 2014). The investigation presented in the article is centered around testing porous domes as infrasound sensors on Earth. The study uses previously developed theories for measuring wind noise with wind barriers and adapts them to the geometry of the dome shaped filters. The goal is to investigate whether the dome style filters could be comparable replacements for current infrasound measuring devices in use that are less mobile, compact, and user friendly in regards to setting up. As a consequence, this also lends to the domes being ideal for use on other planets via space travel, which requires minimization of weight and ease of use and deployment. It is this idea that is explored in the present study within Mars' atmosphere.

Expressions for outputting a theoretical wind noise prediction were developed previously in works by Yu (2009) and Abbott (2014). These expressions give predictions for various types of wind noise generating mechanisms in the form of power spectral densities. The three sources of turbulence production focused on throughout these works were that of turbulence-turbulence, turbulence-shear, and turbulence-sensor interactions. Each source of wind noise can be divided into separate locations at which they take place in reference to the applied filter being observed for study. Three main regions are described in research done by

Abbott (2014), who uses porous wind fences in an assortment of different configurations to take wind noise measurements within them. The first region is describes as lying inside of the filter presented for study. The second region is referred to as being at the wall of the filter and immediately inside and outside of that wall. The third and final region is designated as lying some significant distance outside the wall of the filter in an open atmosphere. Abbott alters his wind fences in porosity, length of gap separation from the ground, and inclusion of or lack of a porous top. From this he is able to compare predicted results through use of the expressions for power spectral density and actual measured power spectral densities gathered from measured velocity spectrums. Abbott test porosities of 30%, 40%, 55%, 65%, and 80% with the conclusion that porosities in the mid-range of 40% to 65% are best suited for infrasonic filtering on Earth.

Preceding Abbott's work is that of Yu (2009) who performs calculations for wind noise at the surface of Earth along with taking measured data at ground level. Yu takes these measurements with a pressure sensor placed at the ground level and also repeats the study with a sensor implanted in the ground so that its top is flush with the ground. By placing the sensor flush with the ground Yu hypothesized that this would reduce measured with noise of turbulence-sensor interaction from a stagnation pressure interacting with the surface of the pressure sensor. Yu's work follows closely that of Robert H. Kraichnan (1956a) who performed studies of pressure fluctuations in turbulent flow over a flat plate. Yu goes on to obtain more accurate wind noise predictions by expanding on the work of Kraichnan through use of more accurate velocity profiles in her expressions for predicted wind noise. While Kraichnan uses a simple exponential form of $V(z) = Ae^{-\beta z}$ to fit velocity profiles in the equations for predicting power spectral density, Yu uses a summation of multiple

exponentials expressed as, $V(z) = V_0(1 - \sum_{i=0}^{n-1} A_i e^{-\beta_i z} - (1 - \sum_{i=0}^{n-1} A_i) e^{-\beta_n z})$ to more accurately fit the velocity profile close to the surface.

William K. George (1984) expands upon the theory presented for predicting a fluctuating pressure spectrum by obtaining more explicit expressions for predicted power spectral densities due to turbulence-turbulence and turbulence-shear interactions. Upon generating these expressions George continues on to test their validity in comparison to measured spectral densities through use of a static-pressure probe. George ultimately concludes that predictions do not exactly match those of measured spectrums but are rather slightly lower which is expected due to conservative assumptions in development of theoretical equations for fluctuating pressure spectrums. George goes on to note that these discrepancies in measured values to those of predicted values is likely due to the following sources of error: velocity contamination of the pressure probe used in gathering data and deviations from Taylor's Hypothesis at low wave numbers due to breakdown in isotropic assumptions of the fluid. Even with the given differences, George concludes that theoretical expressions for predicting pressure fluctuations due to turbulence-turbulence and turbulence-shear mechanisms are in overall good agreement with empirical measurements and therefore useful in the field of aeroacoustics and atmospheric studies.

Kraichnan (1956a) provides a description of vital qualitative features that contribute most to pressure fluctuations experienced at the surface. To generate equations for predicting pressure fluctuations at a surface Kraichnan imparts assumptions of adiabatic conditions, small or no compressibility, and slow rate of growth of the boundary layer in the atmosphere. It is through these features that Kraichnan generates equations utilized throughout the above listed and present studies. Kraichnan presents this procedure at the time of publishing due to

the lack of knowledge about boundary layer flow in the atmosphere. In doing so Kraichnan is able to generate equations that produce respectable predicted values in comparison to measured values of pressure fluctuations experienced at the surface.

Contributions in predicting pressure fluctuations due to turbulence in the atmosphere are also given by G. K. Batchelor (1951). Batchelor takes a different approach to developing equations for predicting pressure fluctuations in that he makes the connection that fourth moments are connected to second moments by normal joint distribution of velocities at any two points and all odd order moments are taken to be zero. This is acceptable since the measured velocities are real valued random variables and the measurements can be viewed as a probability distribution where the fourth moment is the square of the second moment times the number of possible values for velocity. Batchelor test his predictions with reasonable results and attributes discrepancies to the fact that odd ordered moments, though very small, are not exactly zero.

Work done by Theodore von Kármán (1948) proved to be vital in the theory of turbulence predictions performed in many of the aforementioned studies. von Kármán expanded upon previous studies done by Taylor in the sense that he aimed to provide a more general expression for the behavior of measured velocity spectrums in turbulent flow. While Taylor and others utilized the kinetic theory of gases and mean motion in their work von Kármán followed a different approach through use of similarity principle. By use of this von Kármán generated the following function,

$$\Phi(\zeta) = const. \frac{\zeta^4}{(1 + \zeta^2)^{17/6}}$$

which fits measure velocity spectra quite well. A revised version of the function given above is commonly used in present day studies including the one presented herein.

Another prominent figure in the field of turbulence studies is G. I. Taylor. Taylor is the originator of the Taylor Hypothesis (1937) used in a multitude of studies including the present one. Taylor formed his hypothesis through observations that show the spectrum of time varied wind at one point is tied to the correlation of wind spectrums at two different locations. Taylor shows that the spectrum curve from one location is the Fourier transform of the correlation curve from two different points. In essence this allows an experimenter to take measurements at one fixed location over some period of time and treat it as if it were a measurement of multiple locations at a fixed time.

Chapter 2: Derivation of Power Spectral Density for Region 3

Following closely the work of Kraichnan (1956), we develop an expression for Region 3, where we experience mechanisms of turbulence-shear and turbulence-turbulence interactions. For this region, the total velocity, \vec{v} , and total pressure, p , are given by

$$\vec{v} = \vec{V} + \vec{v}_1 \quad \text{and} \quad p = P + p_1$$

where V and P are mean values while v_1 and p_1 are turbulent fluctuations, of velocity and pressure, respectively. Beginning with the Navier-Stokes momentum equation for fluid motion with constant Martian surface density ρ , we have

$$\rho \partial_t \vec{v} + \vec{v} \cdot \vec{\nabla} \vec{v} = -\vec{\nabla} p + \eta \nabla^2 \vec{v}$$

$$\vec{\nabla} \cdot \vec{v} = 0.$$

Letting $\vartheta = \eta/\rho$ (kinematic viscosity) and taking the divergence of this Navier-Stokes equation one obtains

$$\vec{\nabla} \cdot \partial_t \vec{v} + \vec{\nabla} \cdot (\vec{v} \cdot \vec{\nabla} \vec{v}) \simeq -\frac{1}{\rho} \nabla^2 p + \vartheta \vec{\nabla} \cdot (\nabla^2 \vec{v}),$$

where $\partial_t \vec{\nabla} \cdot \vec{v} = 0$ and $\vartheta \nabla^2 (\vec{\nabla} \cdot \vec{v}) = 0$ for incompressible fluids ($\vec{\nabla} \cdot \vec{v} = 0$). Furthermore we expand the total derivative of the velocity to obtain

$$\begin{aligned} -\frac{\nabla^2 p}{\rho} &= \vec{\nabla} \cdot (\vec{v} \cdot \vec{\nabla} \vec{v}) = \sum_i \partial_i \left(\sum_j v_j \partial_j \right) v_i = \sum_{i,j} \partial_i (v_j \partial_j v_i) \\ &= \sum_{i,j} (\partial_i v_j) (\partial_j v_i) + \sum_{i,j} v_j \partial_i \partial_j v_i = \sum_{i,j} (\partial_i v_j) (\partial_j v_i) + \sum_j v_j \partial_j \left(\sum_i \partial_i v_i \right), \end{aligned}$$

where $(\sum_i \partial_i v_i) = \vec{\nabla} \cdot \vec{v} = 0$, yielding

$$= \sum_{i,j} (\partial_i v_j) (\partial_j v_i),$$

which describes the source equation in terms of shear velocity gradients.

Now starting with the source equation and the substitution of the expanded shear velocity gradient one can write

$$\nabla^2 p(\vec{r}, t) = -\rho \sum_{i,j} (\partial_i v_j) (\partial_j v_i) \equiv -T(\vec{r}, t) \quad (2)$$

and denote the source function as $-T(\vec{r}, t)$.

Our coordinate frame of reference is shown in Figure 2.1.

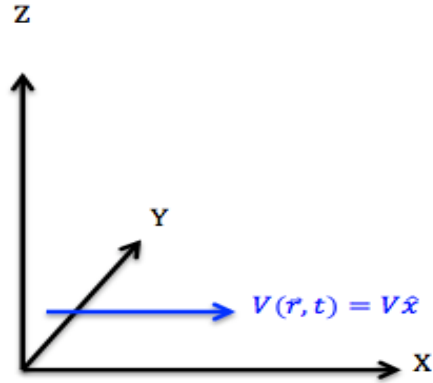


Figure 2.1 Reference coordinate system.

Applying the boundary conditions

$$p(\infty, t) = 0$$

$$\frac{\partial p}{\partial z} \Big|_{z=0} = 0 \quad (\Leftrightarrow v(x, y, 0, t) = 0) \quad (3)$$

Following this, a spatial-temporal Fourier transform is applied to the source function yielding

$$\nabla^2 p(\vec{r}, t) = -T(\vec{r}, t) \Leftrightarrow k^2 \tilde{p}(\vec{k}, \omega) = \tilde{T}(\vec{k}, \omega) \quad (4)$$

where

$$\tilde{p}(\vec{k}, \omega) = \frac{1}{(2\pi)^2} \int d^3r \int_{-\infty}^{\infty} dt p(\vec{r}, t) e^{-i(\vec{k} \cdot \vec{r} - \omega t)}$$

$$\tilde{T}(\vec{k}, \omega) = \frac{1}{(2\pi)^2} \int d^3r \int_{-\infty}^{\infty} dt T(\vec{r}, t) e^{-i(\vec{k} \cdot \vec{r} - \omega t)} \quad (5)$$

denote the Fourier transforms of $p(\vec{r}, t)$ and $T(\vec{r}, t)$, respectively.

Assuming flow of our fluid is homogeneous in the horizontal plane (x, y) and inhomogeneous in the vertical direction (z) where the shear stress is formed, we may then separate out the horizontal wave vector as $\vec{\kappa} = (k_x, k_y) = k_x \hat{x} + k_y \hat{y}$.

This leads to

$$\nabla^2 \rightarrow -\kappa^2 + \frac{\partial^2}{\partial z^2} \equiv -\kappa^2 + \partial_z^2$$

i.e.

$$\partial_z^2 \tilde{p}(z, \vec{\kappa}, \omega) - \kappa^2 \tilde{p}(z, \vec{\kappa}, \omega) = -\tilde{T}(z, \vec{\kappa}, \omega)$$

or

(6)

$$(\partial_z^2 - \kappa^2) \tilde{p}(z, \vec{\kappa}, \omega) = -\tilde{T}(z, \vec{\kappa}, \omega)$$

where

$$\tilde{p}(z, \vec{\kappa}, \omega) = \frac{1}{(2\pi)^{3/2}} \iint_0^\infty dx dy \int_{-\infty}^\infty dt p(\vec{r}, t) e^{-i(k_x x + k_y y - \omega t)}$$

and

(7)

$$\tilde{T}(z, \vec{\kappa}, \omega) = \frac{1}{(2\pi)^{3/2}} \iint_0^\infty dx dy \int_{-\infty}^\infty dt T(\vec{r}, t) e^{-i(k_x x + k_y y - \omega t)}.$$

Solving for $\tilde{p}(z, \vec{\kappa}, \omega)$ in Equation (6), we obtain

$$\tilde{p}(z, \vec{\kappa}, \omega) = A e^{\kappa z} + B e^{-\kappa z} + \frac{1}{2\kappa} \int_{-\infty}^\infty dz' e^{-\kappa|z'-z|} \tilde{T}(z', \vec{\kappa}, \omega). \quad (8)$$

Furthermore, using boundary conditions from Equation (3), we solve for A and B by

denoting that $\tilde{p}(\infty) \rightarrow 0$ so that $A = 0$ and $\frac{\partial \tilde{p}}{\partial z}|_{z=0} = 0$ giving us

$$0 = -\kappa B + \frac{1}{2\kappa} \int_{-\infty}^{\infty} dz' \tilde{T}(z', \vec{\kappa}, \omega) (+\kappa) e^{-\kappa z'},$$

$$0 = -\kappa B + \frac{1}{2} \int_{-\infty}^{\infty} dz' e^{-\kappa z'} \tilde{T}(z', \vec{\kappa}, \omega),$$

$$B = \frac{1}{2\kappa} \int_{-\infty}^{\infty} dz' e^{-\kappa z'} \tilde{T}(z', \vec{\kappa}, \omega).$$

Equation (8) now becomes

$$\tilde{p}(z, \vec{\kappa}, \omega) = \frac{1}{2\kappa} \int_{-\infty}^{\infty} dz' e^{-\kappa z'} \tilde{T}(z', \vec{\kappa}, \omega) + \frac{1}{2\kappa} \int_{-\infty}^{\infty} dz' e^{-\kappa|z'-z|} \tilde{T}(z', \vec{\kappa}, \omega). \quad (9)$$

Examining \tilde{p} at the surface where $z = 0$ we write

$$\tilde{p}_s \equiv \tilde{p}(0, \vec{\kappa}, \omega) = \frac{1}{\kappa} \int_{-\infty}^{\infty} dz' e^{-\kappa z'} T(z', \vec{\kappa}, \omega). \quad (10)$$

In Equations (9) and (10) we examine flow above the surface where $z > 0$ so that the integration can now be performed as $\int_{-\infty}^{\infty} dz' \rightarrow \int_0^{\infty} dz'$.

Imposing the assumption of large-scale homogeneous flow in the horizontal plane (x, y), the power spectral density at the surface (z=0) is given by

$$\begin{aligned}
\langle |\tilde{p}(0, \vec{\kappa}, \omega)|^2 \rangle &= |\tilde{p}(0, \vec{\kappa}, \omega)|^2 = \\
&= \frac{1}{\kappa^2} \left(\int_0^\infty dz' e^{-\kappa z'} \tilde{T}(z', \vec{\kappa}, \omega) \right) \left(\int_0^\infty dz'' e^{-\kappa z''} \tilde{T}^*(z'', \vec{\kappa}, \omega) \right) \\
&= \frac{1}{\kappa^2} \int_0^\infty dz' \int_0^\infty dz'' e^{-\kappa(z'+z'')} \langle \tilde{T}(z', \vec{\kappa}, \omega) \tilde{T}^*(z'', \vec{\kappa}, \omega) \rangle, \tag{11}
\end{aligned}$$

where the correlation quantity $\langle \tilde{T}(z', \vec{\kappa}, \omega) \tilde{T}^*(z'', \vec{\kappa}, \omega) \rangle$ is given by Kraichnan (1955) as

$$\langle \tilde{T}(z', \vec{\kappa}, \omega) \tilde{T}^*(z'', \vec{\kappa}, \omega) \rangle = \frac{A\tau}{(2\pi)^{\frac{3}{2}}} \tilde{S}(z', z'', \vec{\kappa}, \omega), \tag{12}$$

where $\tilde{S}(z', z'', \vec{\kappa}, \omega)$ is the Fourier transform of the space-time auto correlation of $T(\vec{r}, t)$ i.e.

$\langle T(\vec{r}', t') T(\vec{r}'', t'') \rangle = S(z', z'', x' - x'', y' - y'', t' - t'')$. Since the flow is horizontally

homogeneous this leads to

$$\tilde{S}(z' z'', \vec{\kappa}, \omega) = \frac{1}{(2\pi)^{\frac{3}{2}}} \int_{-\infty}^{\infty} d\zeta_1 \int_{-\infty}^{\infty} d\zeta_2 \int_{(0)}^{(\tau)} dt S(z', z'', \zeta_1, \zeta_2, t) e^{-i(\vec{\kappa} \cdot \vec{\zeta} - \omega t)}, \tag{13}$$

where $\vec{\zeta} = (\zeta_1 \hat{x} + \zeta_2 \hat{y})$. We assume the correlation is taken so that the flow is over a large surface area A and a time scale τ long enough to resolve low frequencies in the measured signal (Kraichnan 1956).

In order to analyze the fluctuations of the pressure power spectrum in the \hat{x} direction in Equation (11) we integrate over ω and k_y only. In doing so we obtain the expression (Yu 2011):

$$|\tilde{p}(0, k_x)|^2 = \int_{-\infty}^{\infty} dk_y \int_{-\infty}^{\infty} d\omega |\tilde{p}(0, \vec{k}, \omega)|^2 . \quad (14)$$

Taking the real part of Equation (13) we have

$$\int_{-\infty}^{\infty} dt S(z', z'', \zeta_1, \zeta_2, t) e^{-i(\vec{k} \cdot \vec{\zeta} - \omega t)} = 4\pi^2 \frac{dV}{dz} \Phi_{yy}(\vec{k}) , \quad (15)$$

where

$$\frac{dV}{dz} ,$$

is the velocity gradient for Region 3. In Region 3 the velocity profile is represented by a well know logarithmic function $V(z) = a * \ln(\frac{z+z_0}{z_0})$ where z_0 is the roughness length for the respective region. The gradient is

$$\frac{dV}{dz} = \frac{a}{z + z_0}. \quad (16)$$

Also in Equation (15) we have

$$\Phi_{yy}(\vec{k}) = \frac{E(k)}{4\pi k^4} \kappa^2, \quad (17)$$

where $E(k)$ is a semi-empirical velocity function developed by von Kármán (1948) that matches well the behavior of velocity fluctuations as a function of frequency or wave number given by Yu (2009):

$$E(k) = \frac{55C}{18} \frac{(k\lambda)^4}{[1 + (k\lambda)^2]^{\frac{17}{6}}}. \quad (18)$$

Within the function $E(k)$, “C” and “ λ ” are fitting parameters to what would be a measured velocity spectrum by sensors on Mars. Here $k = \sqrt{k_x^2 + k_y^2 + k_z^2}$ is the wavenumber.

Finally, substituting Equations (15)-(18) into Equation (14) we obtain the result for pressure as a function of wave number. For the presented data the results of pressure fluctuations will be shown as function of frequency by multiplying the final result of $|\tilde{p}(0, k_x)|^2$ by $\frac{2\pi}{V_\alpha}$ (V_α being the horizontal wind velocity component in each region, $\alpha = 1,2,3$) to change the representation from \vec{k} -space to ω -space. This yields, for Region 3,

$$\begin{aligned}
|p_3(0, f)|^2 &= \tag{19} \\
&= \frac{880a^2 C \lambda^4 \rho^2 k_x^2}{9V_3} \int_0^\infty \int_0^\infty \frac{dk_z dk_y}{[1 + (k\lambda)^2]^{17/6}} \int_0^\infty \frac{e^{-\kappa z'} \sin(k_z z') dz'}{z' + z_0} \int_0^\infty \frac{e^{-\kappa z''} \sin(k_z z'') dz''}{z'' + z_0}.
\end{aligned}$$

We may now calculate a final value for pressure by utilizing Taylor's frozen wave hypothesis (Taylor 1938). Taylor states that one would obtain roughly the same data by recording in time at a fixed location as one would by moving rapidly upstream against the mean wind so that

$$k_x = \frac{2\pi f}{V_\alpha}. \tag{20}$$

Derivation of PSD for Region 1

The next region we examine is Region 1. Region 1 is described as being inside the porous dome, away from its surface. Region 1 is quite similar to Region 3 in that the pressure fluctuations arise from the same mechanisms, i.e., turbulence-turbulence and turbulence-shear interactions. However, when analyzing Region 1, we must take into account that flow inside the dome filter has already been affected by passage through the porous walls. The flow in this region is constrained to within the height of the dome hence the integrals are calculated from the surface (or the roughness length) to the dome height. Yu et al. showed that a simple exponential fits poorly the measured velocity profile near the surface due to varying roughness length and the fact that flow has been disturbed by passage through the porous barrier; they determined that the velocity profile in this region are fitted better by a summation of multiple exponentials represented by

$$V(z) = v_0 \left(1 - \sum_{i=1}^n A_i e^{-\beta_i(z-z_0)} \right). \quad (21)$$

Here v_0 , A_i , and β_i are the fit parameters to what would be a measured velocity profile in Region 1 on Mars and z_0 represents the roughness length. In developing a formula for calculating theoretical pressure fluctuation contributions as a function of frequency we follow the same procedure as described in Region 3. The principal difference between Regions 1 and 3 lies in the velocity profile (namely exponential instead of logarithmic), which we substitute in place of the previous Equation (16) and integrate from the roughness length to the height of the dome. The velocity gradient for this region is therefore

$$\frac{dv}{dz} = v_0 \sum_{i=1}^n A_i \beta_i e^{-\beta_i(z-z_0)}, \quad (22)$$

$$s_i = v_0 A_i \beta_i \rightarrow z',$$

$$s_j = v_0 A_j \beta_j \rightarrow z''.$$

Using Equation (22) in Equation (15), one obtains the pressure power spectrum for Region 1 as follows:

$$\begin{aligned} |p_1(0, f)|^2 &= \quad (23) \\ &= \frac{880C\lambda^4\rho^2k_x^2}{9V_1} \times \sum_{i=1, j=1}^{i=n, j=m} s_i s_j e^{z_0(\beta_i + \beta_j)} \times \\ &\times \int_0^\infty \int_0^\infty \frac{dk_z dk_y}{[1 + (k\lambda)^2]^{\frac{17}{6}}} \int_{z_0}^h e^{-(\kappa + \beta_i)z'} \sin(k_z z') dz' \int_{z_0}^h e^{-(\kappa + \beta_j)z''} \sin(k_z z'') dz'' \end{aligned}$$

Derivation of PSD for Region 2

Concluding the derivations for power spectral densities, we turn to Region 2. Here, the dominant contribution to wind noise is from stagnation pressure fluctuations due to turbulence-filter interaction. The goal is to obtain an expression for the pressure fluctuations at the sensor location (i.e. center of the dome) starting from the flow field through the porous wall. To this end, we adopt the method developed by Raspet and Abbott (2014), Noble et al. (2014), and Collier et al. (2014).

The pressure at the center of the dome can be obtained similarly to finding the electric potential at the center of a sphere by knowing the potential on the surface (Abbott and Raspet, 2014, Noble et al., 2014). Thus, the pressure at the center, P_c , is obtained as the solid angle average of the dome-surface pressure over the total solid angle $\Omega' = 4\pi$:

$$P_c \equiv p(0, t) = \langle p_{surface} \rangle_{\Omega=4\pi} = \frac{1}{4\pi} \int p_{surface}(\theta', \varphi', t) d\Omega' \quad (24)$$

From this the pressure, velocity, and density terms, as before, are separated into mean and fluctuating components where upper case designates the mean value and the subscript 1 denotes a fluctuating component:

$$p = P + p_1, \quad \vec{v} = \vec{V} + \vec{v}_1, \quad \rho = \rho_0 + \rho_1. \quad (25)$$

From Equation (25) Abbott and Raspet (2014) derive a semi-empirical expression for the surface assuming that the turbulent velocity field outside the dome is isotropic:

$$p_{surface} \approx -\rho_0 \vec{v}_1^{out} \cdot (\vec{V}_{out} - \vec{V}_{in}) \approx -\rho_0 v_1^{out} (\Delta V), \quad (26)$$

where $\Delta V = V_{out} - V_{in}$ is the difference between mean-flow (wind) velocities outside and inside the dome surface i.e. across the porous surface of the dome (Abbott and Raspet 2014, Abbott, 2015).

The center pressure becomes

$$P_{center}(t) = p(0, t) \approx -\frac{\rho_0}{4\pi} \int_0^{\frac{\pi}{2}} \sin(\theta') d\theta' \int_0^{2\pi} d\varphi' v_1^{out}(\theta', \varphi', t) \Delta V. \quad (27)$$

A Fourier transform is taken to transform Equation (27) into wavenumber space:

$$\tilde{p}(0, k) = -\frac{\rho_0}{4\pi} \int_0^{\frac{\pi}{2}} \sin(\theta') d\theta' \int_0^{2\pi} d\varphi' \tilde{v}_1^{out}(\theta', \varphi', k) \Delta V. \quad (28)$$

The pressure power spectrum for Region 2 is obtained as

$$\begin{aligned} \langle |p_2(0, t)|^2 \rangle &= \langle p(0, t)p^*(0, t) \rangle \\ &\approx + \left(\frac{\rho_0}{4\pi}\right)^2 \int_0^{\frac{\pi}{2}} \sin(\theta') d\theta' \int_0^{\frac{\pi}{2}} \sin(\theta'') d\theta'' \int_0^{2\pi} d\varphi' \int_0^{2\pi} d\varphi'' \langle \tilde{v}_1^{out}(\theta', \varphi', k) \tilde{v}_1^{*out}(\theta'', \varphi'', k) \rangle (\Delta V)^2. \end{aligned} \quad (29)$$

Assuming homogenous turbulence, the Fourier transform of the velocity correlation decays exponentially according to Priestley (1966) ---a fact confirmed experimentally by Shields (2005):

$$\langle \tilde{v}_1^{out}(\theta', \varphi', k) \tilde{v}_1^{*out}(\theta'', \varphi'', k) \rangle = F_{out}(k) e^{-\alpha(k)R\sqrt{(\theta' - \theta'')^2 + (\varphi' - \varphi'')^2 \sin^2(\theta')}} , \quad (30)$$

where, $\alpha(k) = \mu k^a$ is the inverse of the correlation length and μ and k are empirical parameters measured and fit by Abbott (2014), R is the radius of the dome, 2 meters; $F_{out}(k)$ is a measured wind velocity power spectrum for which Noble et al. (2014) suggest a fit with two parameters (C_{out} and λ_{out}) as follows (von Kármán, 1948):

$$F_{out}(k) = |v_1^{out}(k)|^2 = \frac{C_{out}}{(1 + k^2 \lambda_{out}^2)^{\frac{5}{6}}} . \quad (31)$$

The final expression for the pressure power spectrum detected at the center of the dome due to turbulent influences in Region 2 is

$$\begin{aligned}
 \langle |p_2(0, f)|^2 \rangle &\simeq \tag{32} \\
 &\simeq \frac{k_x^2 \rho_0^2 R^2}{8\pi V_2} C_{out} \times \\
 &\times \int_0^{\frac{\pi}{2}} \sin(\theta') d\theta' \int_0^{\frac{\pi}{2}} \sin(\theta'') d\theta'' \int_0^{2\pi} d\varphi' \int_0^{2\pi} d\varphi'' \frac{e^{-\alpha(k)R\sqrt{(\theta' - \theta'')^2 + (\varphi' - \varphi'')^2 \sin^2(\theta')}}}{(1 + k_x^2 \lambda_{out}^2)^{\frac{5}{6}}} \times \\
 &\times (V_{out} - V_{in})^2 .
 \end{aligned}$$

Using Taylors Hypothesis (Taylor 1938), the expression is presented in frequency space rather than wavenumber space through multiplication of the wavenumber result by $\frac{2\pi}{V_\alpha}$, where V_α is the horizontal wind velocity component in Region 2. For the density on the Martian surface environment a mean value is used ($\rho_0 \sim 0.02 \text{ kg/m}^3$) while k_x is expressed as $k_x = 2\pi f / V_\alpha$.

Chapter 3: Methods for Determining Region Coefficients

In previous works by Abbott (2014) and Yu (2009), experimental data was easily attainable through measurement apparatuses for calculating power spectral densities on Earth. This data was then analyzed by plotting and fitting with the appropriate software. A problem faced in this study was a lack of experimental wind data gathered from Mars. Though there have been multiple missions to the Martian planet by various countries and agencies, there is very little information retrieved about the planets' wind profiles. Many missions have taken measurements of wind speed and direction, albeit at only one height and at snippets in time as opposed to continuous measurements at various altitudes. In addition to limited locations of measurement, some apparatuses used were not very sophisticated such as that of the Telltale mechanical anemometer (NASA PDS). These measurement limitations are mostly due to space craft restrictions such as size, weight, and power required for economical space flight, travel, and operation.

Information for the present study is gained through the utilization of general circulation models (GCMs). These GCMs are computational models developed by universities and other public or private organizations which simulate a variety of different planetary environments. They are developed from first principles and incorporate any available empirical data from multiple resources into their models. The GCM utilized in this study is the Mars Climate Database (MCD), developed by Laboratoire de Meteorologie Dynamique in Paris, which is relied on for extracting wind data predictions.

Five different locations were chosen for the analysis of wind noise in the Martian environment. The five locations chosen were landing sites of various Mars missions as follows: Curiosity, Phoenix, Pathfinder, Viking Lander 1, and Viking Lander 2. The motivation for choosing these particular locations were that this initial investigation would spark interest for continuing studies of how wind noise might be related to other commonly measured variables. Many missions to Mars do not include much wind data but all measure variables such as pressure, temperature, and density. Since data sets of these parameters are abundant one would hope to see comparative studies on how they might affect generation and collection of wind noise in the future.

When generating velocity profiles for use in calculations at these five locations, two types of profiles are generated from the GCM. The first profile is a max wind velocity and the second one is a minimum wind velocity. Depending on the region, particular height versus wind speed data points were observed along with time of Martian day. From this, times of day where velocity was maximum and minimum were chosen in generating velocity profiles for the respective region. In doing so a best and worst case scenario is presented in the data in terms of possible maximum and minimum wind noise productions.

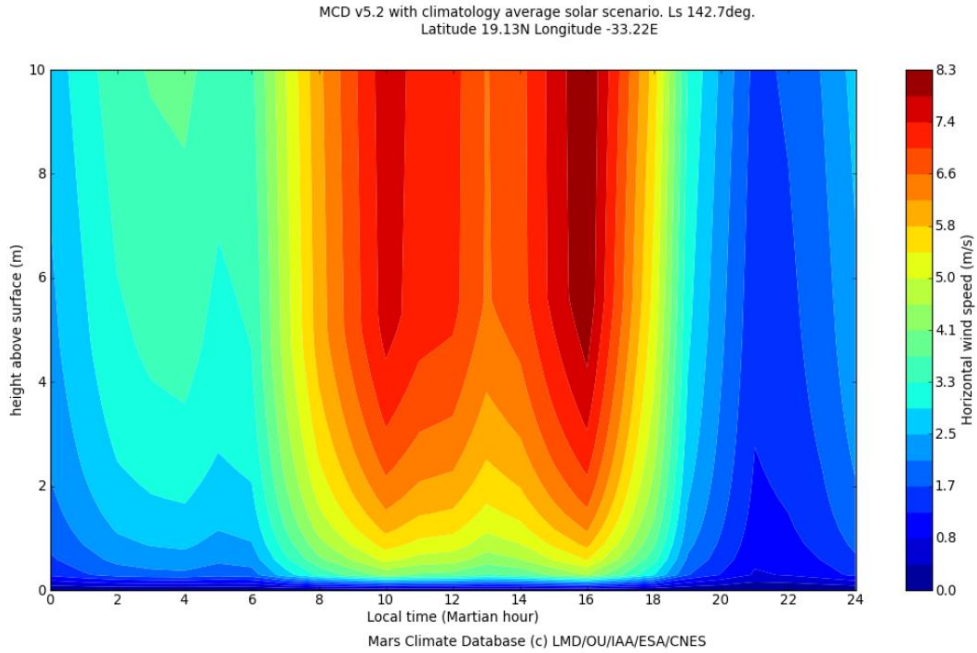


Figure 3.1. An example of wind speeds from 0 to 10 meter altitudes throughout a 25 hour Martian day generated for Region 3 at the Pathfinder location. Here velocity is maximum at the 16th hour of the day and minimum at roughly the 21st hour. *Source:* Mars Climate Database.

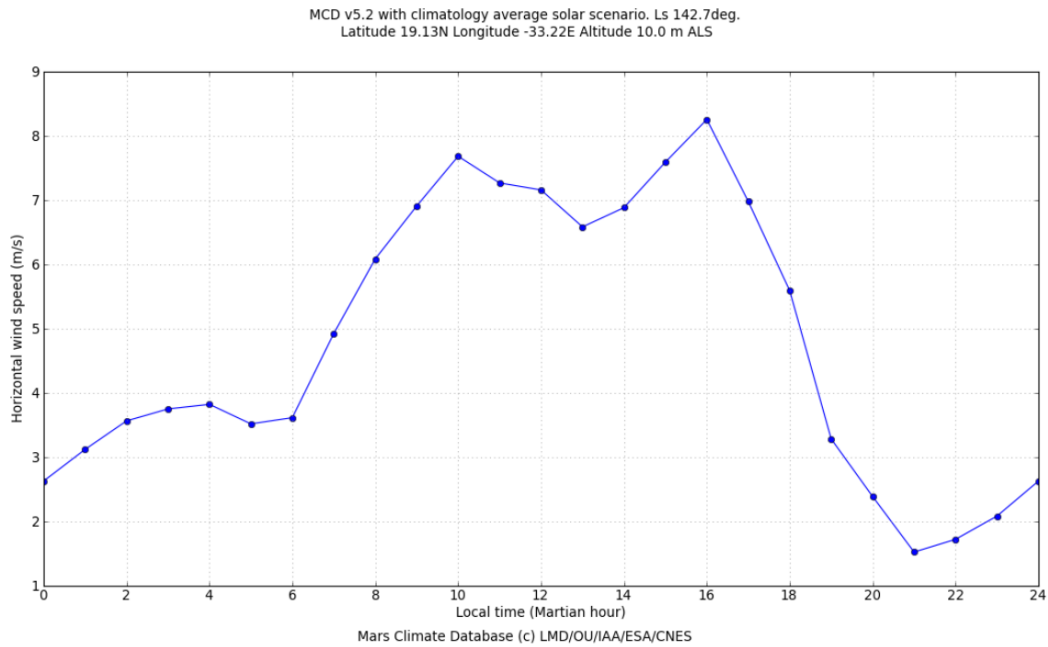
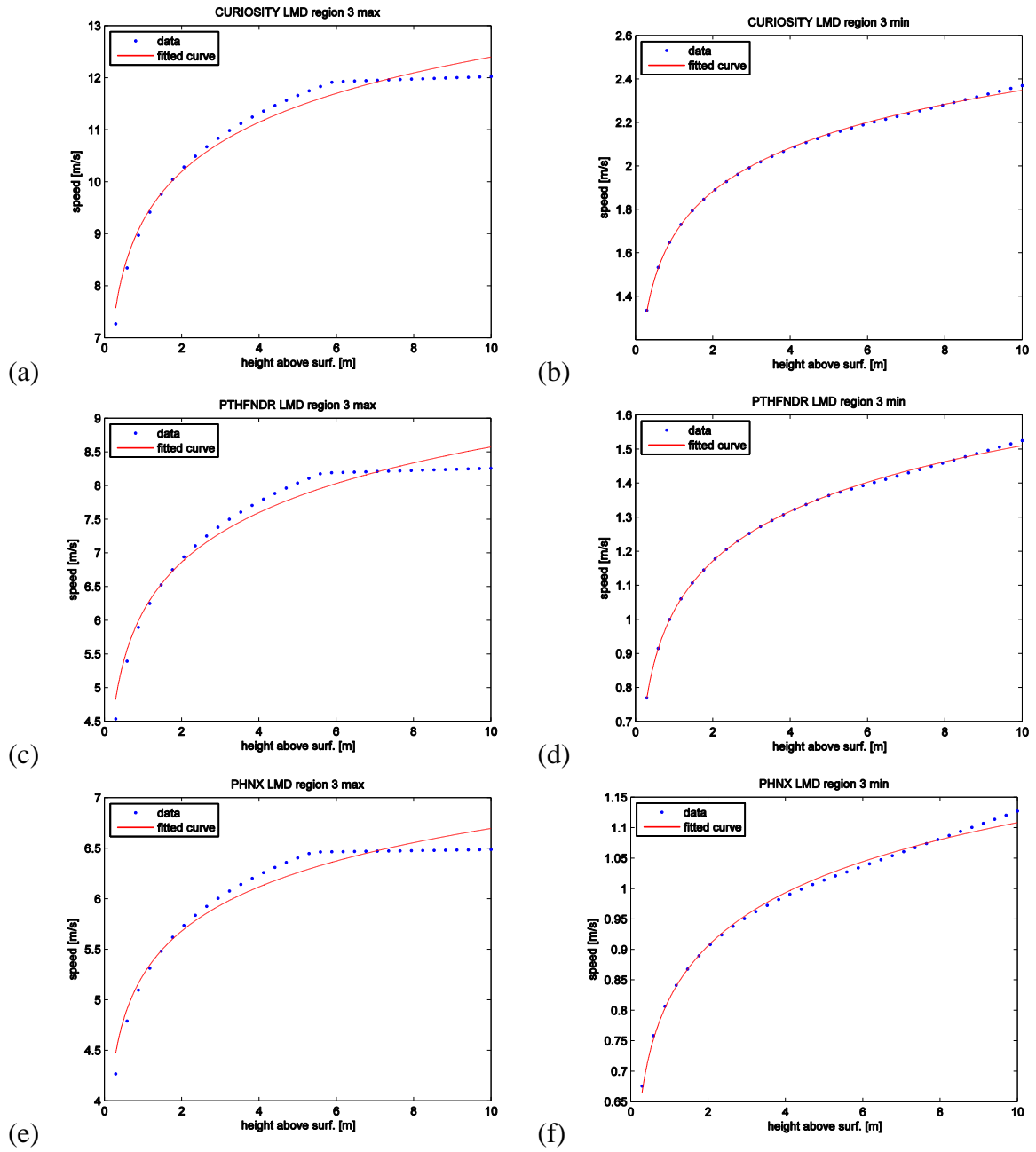


Figure 3.2. Wind speed at the Pathfinder location at 10 meters over a 25 hour Martian day. Data points are averaged to determine a mean wind velocity V_α for Region 3. The same process is applied at 1 meter for Regions 1 and 2. *Source:* Mars Climate Database.

Region 3 Parameters

For Region 3, the first parameter observed in Equation (19) is a . This is a fit parameter from fitting the logarithmic velocity profile $V(z)$. To obtain this value we first use the GCM to plot wind speed as a function of height above surface and Martian time of day, as shown in an example in Figure (3.1). For Region 3, we analyze wind speed from 0 to 10 meters and select times at which velocities are at a minimum and maximum to generate two separate profiles to utilize in generating our pressure spectrums. After selection of these times a second plot is generated with data points for velocity as a function of height and then fitted with the logarithmic function $V(z) = a * \ln(\frac{z+z_0}{z_0})$. Here the value of a is determined from the fit to the data points for each mission location, maximum velocity, and minimum velocity. Profile fits are shown in Figure 3.3 along with their respective R-square values to indicate goodness of fit. Also obtained from the fit is the roughness length for the given region, z_0 . Values obtained from fits for Region 3, heights 0 to 10 meters, maximum and minimum velocities are listed below in Table (3.1).

Region 3 Data Fits



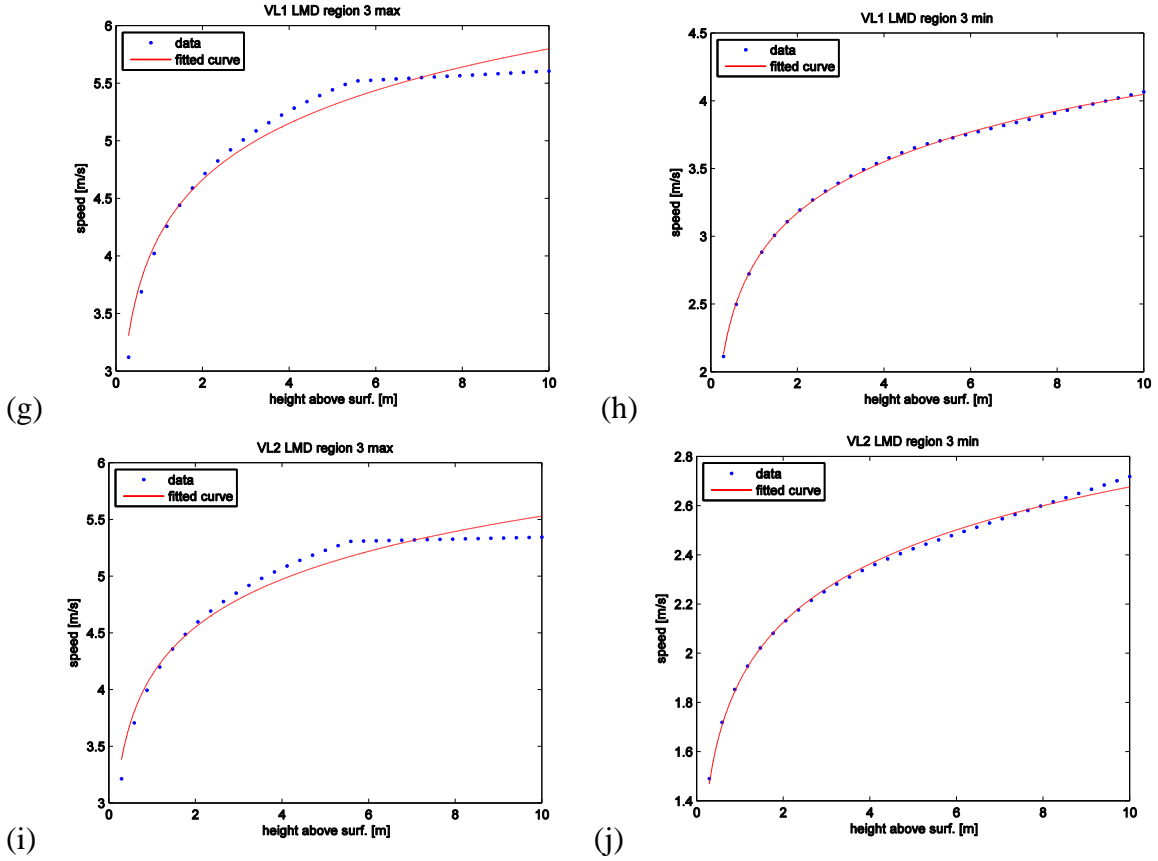


Figure 3.3. Maximum and minimum velocity profile fits to data points for Curiosity, Pathfinder, Phoenix, Viking Lander 1, and Viking Lander 2.

Table 3.1. Fit parameters a and z_0 (meters) for Region 3 $V(z)$

Mission	<i>Curiosity</i>	<i>Phoenix</i>	<i>Pathfinder</i>	<i>VL1</i>	<i>VL2</i>
R-square(max)	0.97	0.96	0.97	0.97	0.97
R-square(min)	0.999	0.995	0.999	0.999	0.997
a (max vel.)	1.368898057	0.631102693	1.064132285	0.706254131	0.60868452
a (min vel.)	0.28929729	0.12571522	0.210511371	0.543679797	0.34224075
z_0 (max vel.)	0.001167719	0.000247	0.003172663	0.002720942	0.001134554
z_0 (min vel.)	0.002988809	0.001484717	0.007678875	0.00584896	0.004020905

The variable V_3 is determined for Region 3 by taking the average velocity at the maximum height of 10 meters over a 25 hour Martian day. Values for V_3 are listed in the table below:

Table 3.2. Average flow velocity in Region 3 at 10 meters over one Martian day

Mission	<i>Curiosity</i>	<i>Phoenix</i>	<i>Pathfinder</i>	<i>VL1</i>	<i>VL2</i>
V_3 [m/s]	6.185742	4.07774852	4.7832176	4.8346736	3.0380488

Values of C and λ would be obtained from fitting a measured velocity fluctuation spectrum at a fixed height on Mars over some time period to the von Kármán (1948) function given in Equation (18). The parameter, λ , determines the location of the peak in the spectrum where a transition from the energy containing sub-range to the inertial sub-range occurs, while C affects the magnitude of the peak. However, since we do not have such measurements we rely on fit parameters from spectrums taken on Earth by Abbott (2015, p.336) based upon the observed porosity of our dome filter. For ρ we use the Martian surface density value of 0.02 kg/m^3 . Finally, for k_x we use Taylor's hypothesis in Equation (20) to solve for its value based on the frequency being examined.

Table 3.3. Fit parameters to measured velocity spectrums on Earth (Abbott 2015).

Porosity	C	λ
30%	26.79	81.41
40%	34.64	110.50
55%	45.88	172.50
65%	257.10	180.40
80%	116.40	154.80

Region 1 Parameters

In using the GCM to generate velocity profiles for Region 1, an issue was incurred where data could not be generated to simulate the decrease in velocity after passage through a porous filter. Due to this, a multiple exponential profile fit could not be readily used for the GCMs given data. In order to address this issue ratios of values measured and fitted for Earth by Abbott (2015) were used to develop a velocity profile expression for Region 1 on Mars. The ratio taken is that of Region 3 to Region 1 where the fit coefficient a from Equation (16) for Earth is divided by the fit coefficient v_0 from Equation (22) for Earth. This ratio is then

multiplied by a from fits generated to Region 3 velocity profiles on Mars to obtain a value of v_0 for Mars. Furthermore, fit values for A_i , β_i , and z_0 used in generating terms s_i and s_j are also obtained from Abbotts (2015) fits to Earth velocity profiles but of course scaled by Mars' v_0 . Results calculated for Mars' v_0 for Equation (22) using Earth ratios are given in the table below:

Table 3.4. Values of v_0 calculated for varying porosities of filter and max/min wind conditions per mission.

Mission:	<i>Curiosity</i>	<i>Phoenix</i>	<i>Pathfinder</i>	<i>Viking 1</i>	<i>Viking 2</i>
30% Max	0.369602465	0.17039772	0.287315717	0.190688616	0.16434482
30% Min	0.078110226	0.033943109	0.056838069	0.146793544	0.092405002
40% Max	0.530797191	0.244713279	0.412622723	0.273853643	0.236020528
40% Min	0.112176439	0.048746717	0.081626857	0.210814614	0.132705596
55% Max	3.46787498	1.598793424	2.69580179	1.789177135	1.542000784
55% Min	0.732886068	0.318478554	0.533295467	1.377322146	0.867009892
65% Max	5.784076134	2.666630989	4.496333601	2.98417239	2.571906423
65% Min	1.222382249	0.531191065	0.889484655	2.297238568	1.446087663
80% Max	6.890893415	3.176906648	5.356733708	3.55521148	3.064055974
80% Min	1.456292344	0.632837626	1.05969282	2.736828796	1.722805116

Table 3.5 Fit parameters for Region 1 PSD velocity profiles measured by Abbott (2015).

Parameter	A_1	A_2	A_3	A_4	A_5	β_1	β_2	β_3	β_4	β_5
30%	-2.26	-2.53	-2.36	-2.11	N/A	0.81	0.75	0.80	0.84	N/A
40%	-0.98	-0.64	-0.86	-0.83	-0.97	0.27	0.26	0.26	0.28	0.28
55%	0.09	0.09	0.09	0.09	0.09	3.56	3.56	3.56	3.56	3.56
65%	0.15	0.15	0.15	0.15	0.15	3.20	3.20	3.20	3.20	3.20
80%	0.13	0.13	0.13	0.13	0.13	1.95	1.96	1.96	1.96	1.96

Values for C and λ are used from Abbott's Earth measurements pertaining to Region 1 and listed in Table (3.6) (Abbott 2015). Also values for ρ , k_x , V_1 were calculated in the same manner described previously for Region 3. For integration bounds, values of z_0 (Table 3.6) are roughness lengths taken to be 0.01 meters and h is the height of our dome filter, 2 meters.

Region 2 Parameters

For Region 2, empirical measurements gathered by Abbott (2015) are heavily utilized in this part of the study due to the inability to simulate wind at the boundary of a porous barrier in the Mars Climate Database General Circulation Models. Predictions for V_α are able to be generated via the MCD for one meter above the ground in free atmosphere at each location. Points for this data are generated at one meter over a 25 hour Martian day and averaged for the speed V_2 , an example is shown in Figure (3.2). Values of C_{out} , ΔV , λ_{out} , μ , and a for varying porosities are taken from Abbott (2015) and listed in the table below.

Table 3.6 Parameters for Regions 1 and 2 PSD calculations (Abbott 2015).

Porosity	C	λ	ΔV	μ	a
30%	0.105	0.885	2.92	1.0304	0.7674
40%	0.006	0.266	2.47	1.4142	0.6545
55%	0.016	0.513	1.82	1.6976	0.6076
65%	0.228	1.846	1.14	1.2786	0.7601
80%	0.371	2.008	0.3	1.5166	0.6681

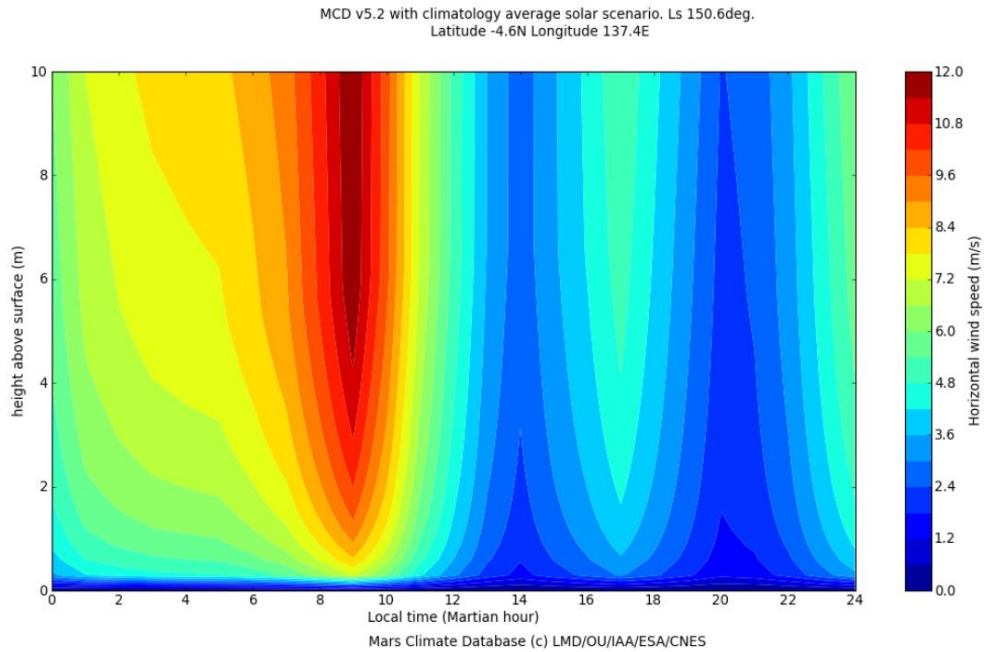
Chapter 4: Results of Power Spectral Density Predictions

A location will be chosen to observe theoretical power spectral density predictions based upon maximum velocity predictions from the MCD. It can be seen that with increased velocity comes increased wind noise and for this reason the location with highest velocity magnitudes will be chosen to observe the effects of our dome filter.

MCD Velocity Predictions

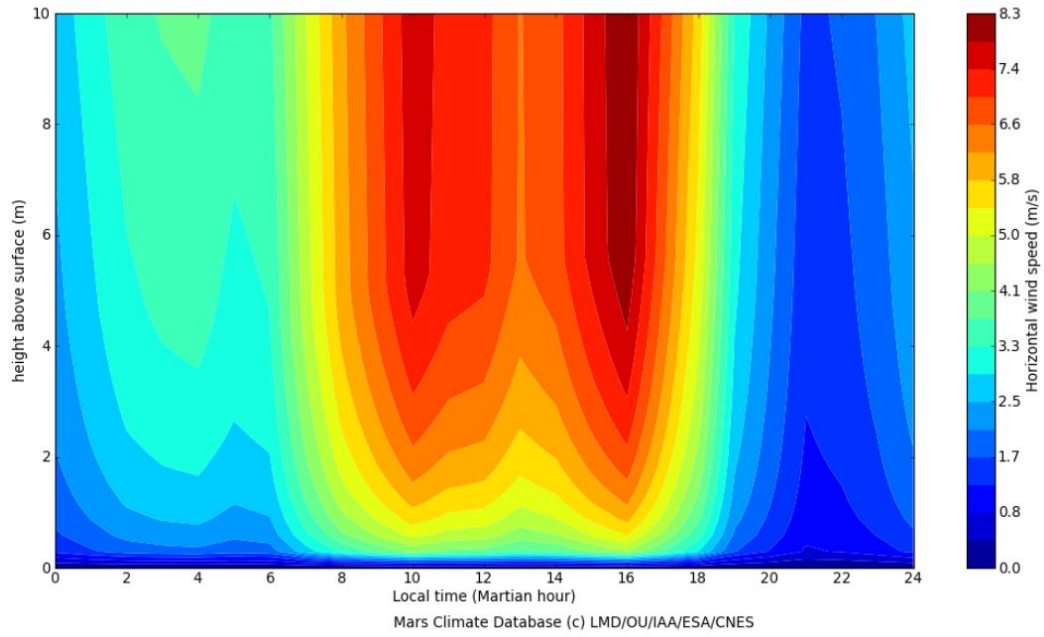
Table 4.1. GPS coordinates for each mission.

Mission	<i>Curiosity</i>	<i>Pathfinder</i>	<i>Phoenix</i>	<i>Viking 1</i>	<i>Viking 2</i>
GPS Location	-4.6 N 137.4 E	19.13 N -33.22 E	68.22 N 234.25 E	22.48 N -49.97 E	47.97 N - 225.74 E



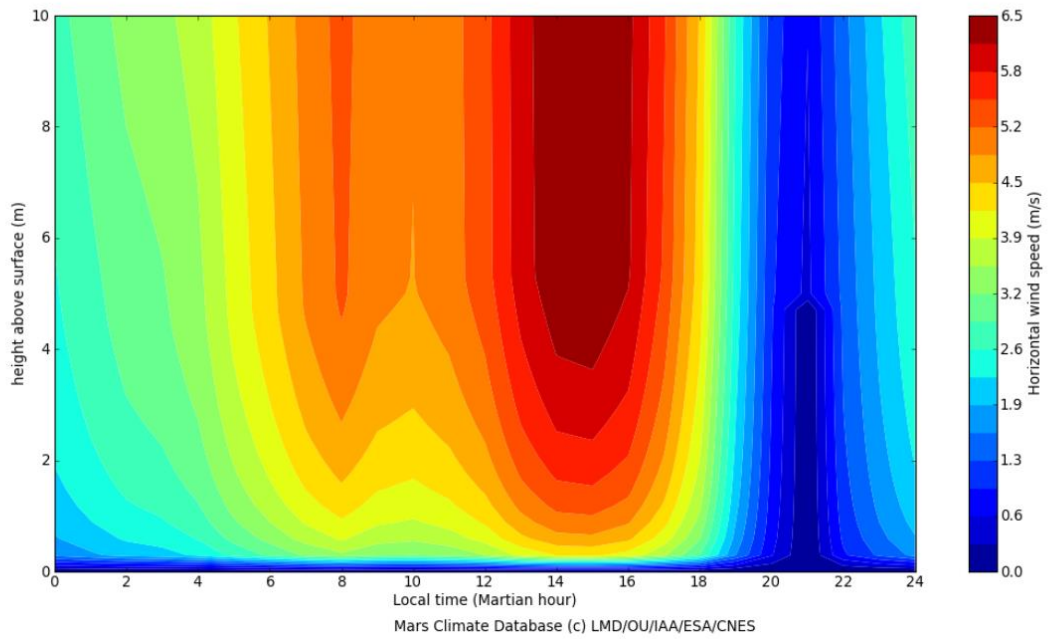
(a)

MCD v5.2 with climatology average solar scenario. Ls 142.7deg.
Latitude 19.13N Longitude -33.22E



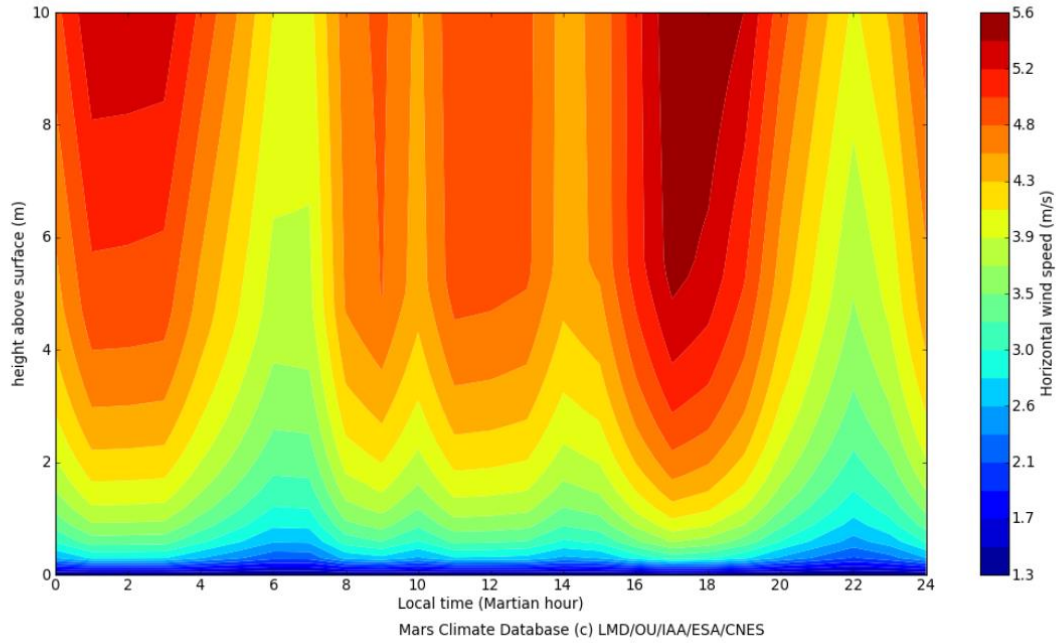
(b)

MCD v5.2 with climatology average solar scenario. Ls 76.6deg.
Latitude 68.22N Longitude 234.25E



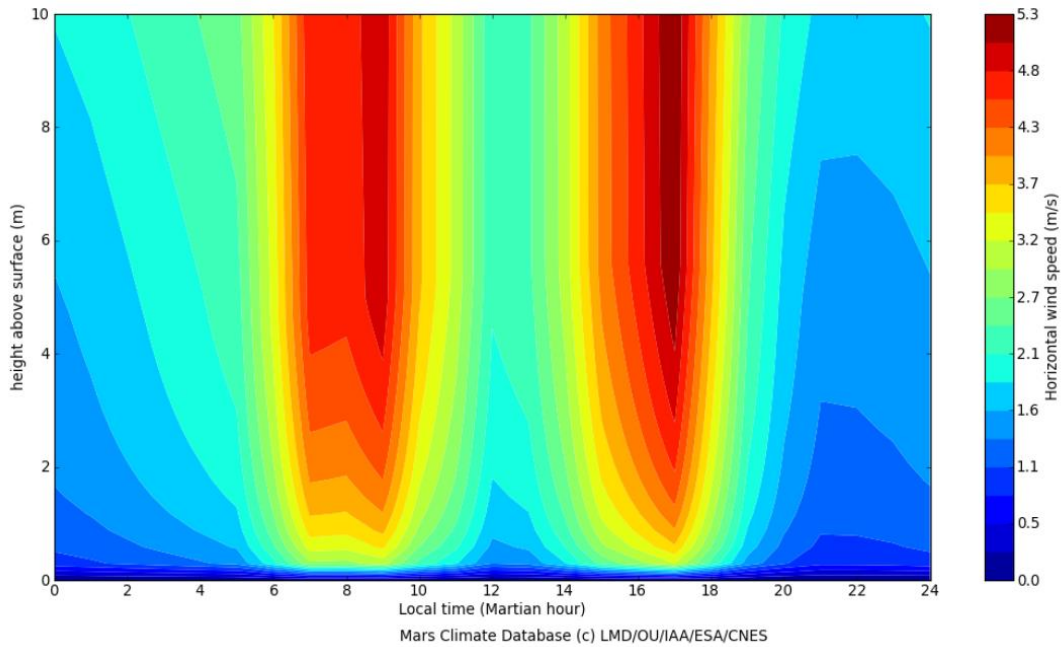
(c)

MCD v5.2 with climatology average solar scenario. Ls 97.0deg.
Latitude 22.48N Longitude -49.97E



(d)

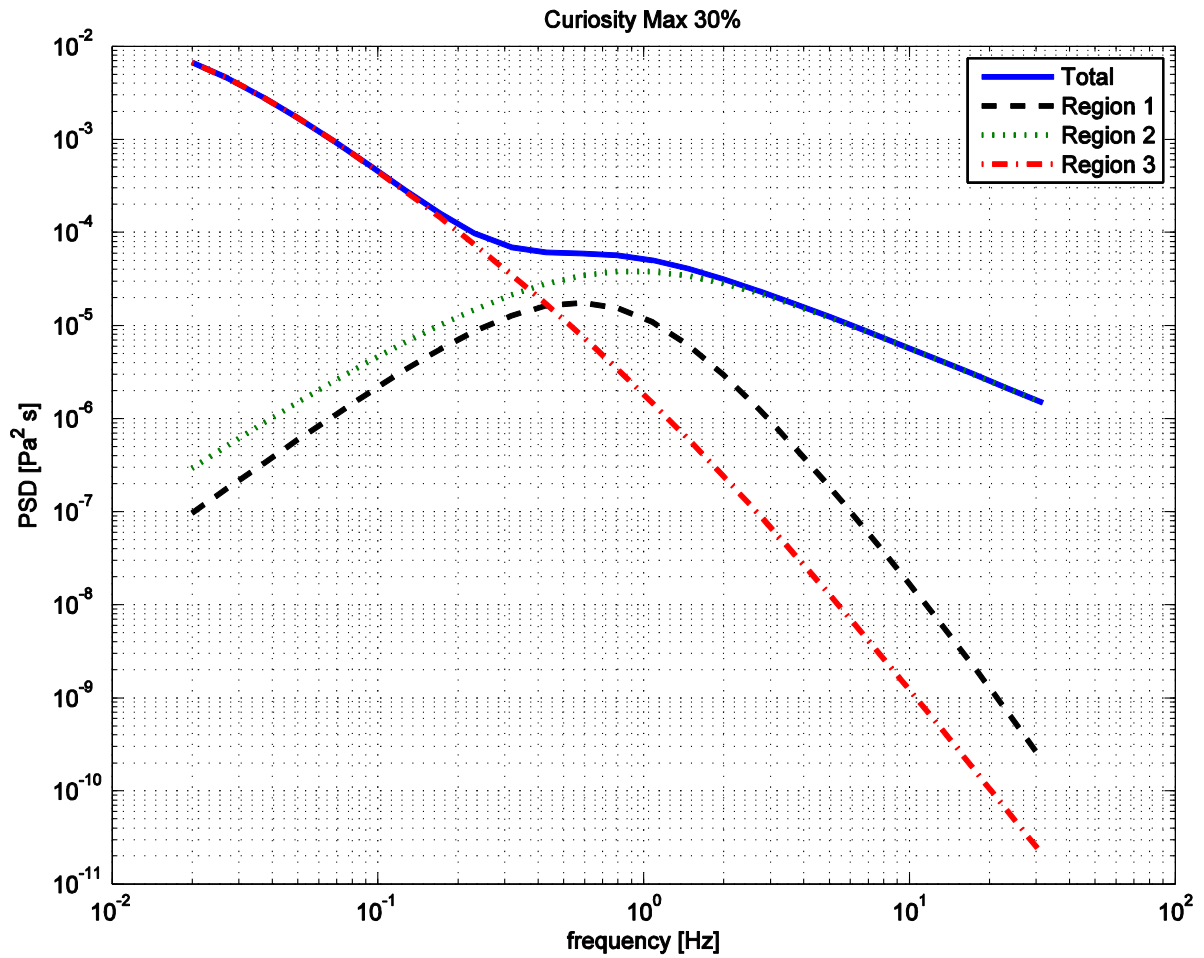
MCD v5.2 with climatology average solar scenario. Ls 117.6deg.
Latitude 47.97N Longitude -225.74E



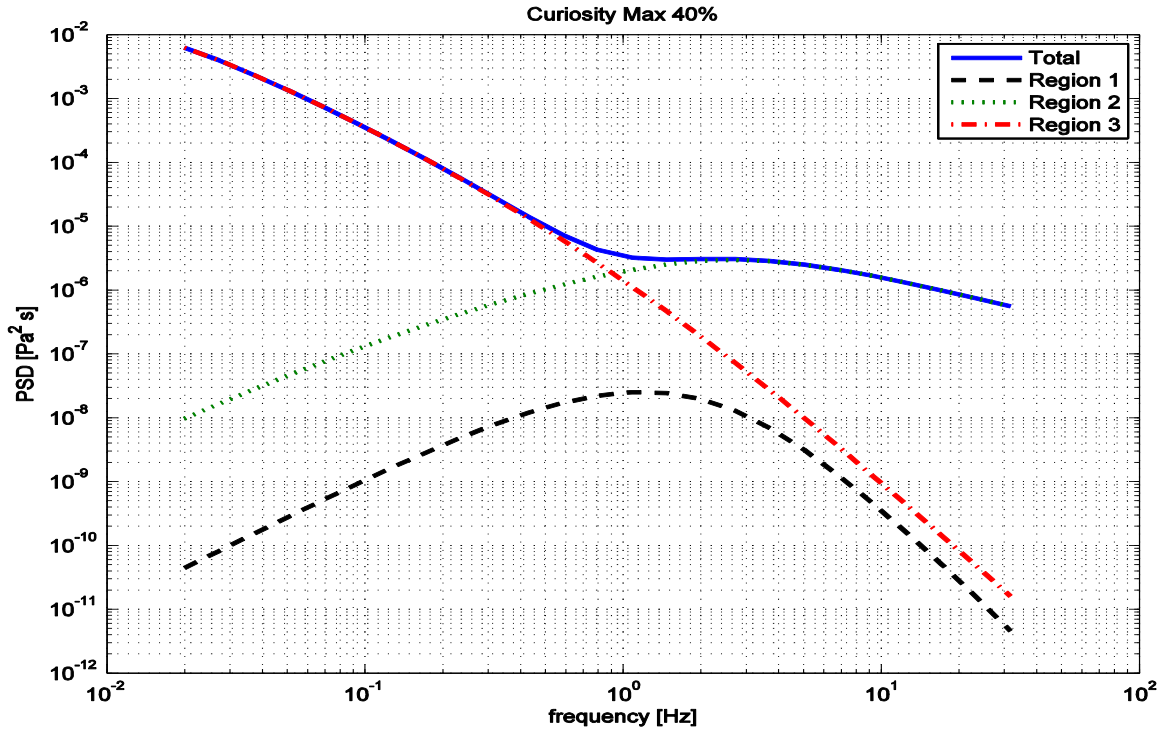
(e)

Figure 4.1. Velocity as a function of time and height above Martian surface modeled at each mission location over a 25 hour Martian day. (a) Curiosity, (b) Pathfinder, (c) Phoenix, (d) Viking Lander 1, (e) Viking Lander 2.

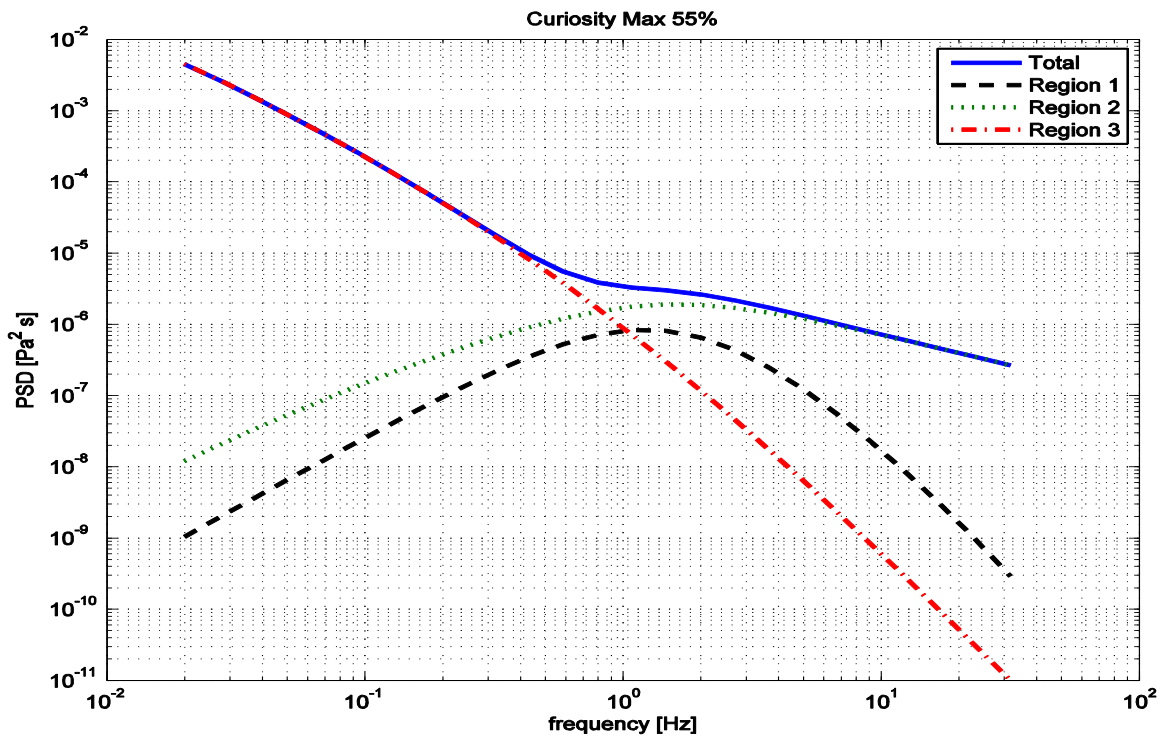
Based on observations from Figure 4.1, the Curiosity landing site is predicted to experience the highest winds of roughly 12 m/s during the 9th hour of the Martian day. Figure 4.2 shows predictions for power spectral densities with varying filter porosities (data for other missions has been placed in the appendix for reference).



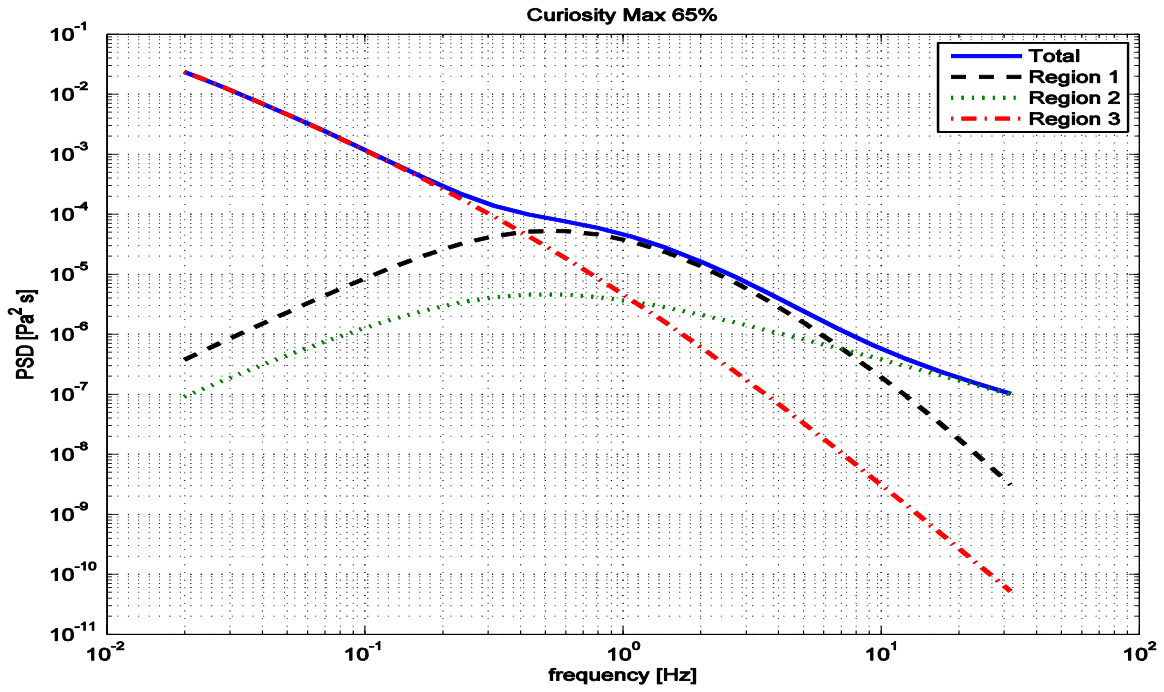
(a)



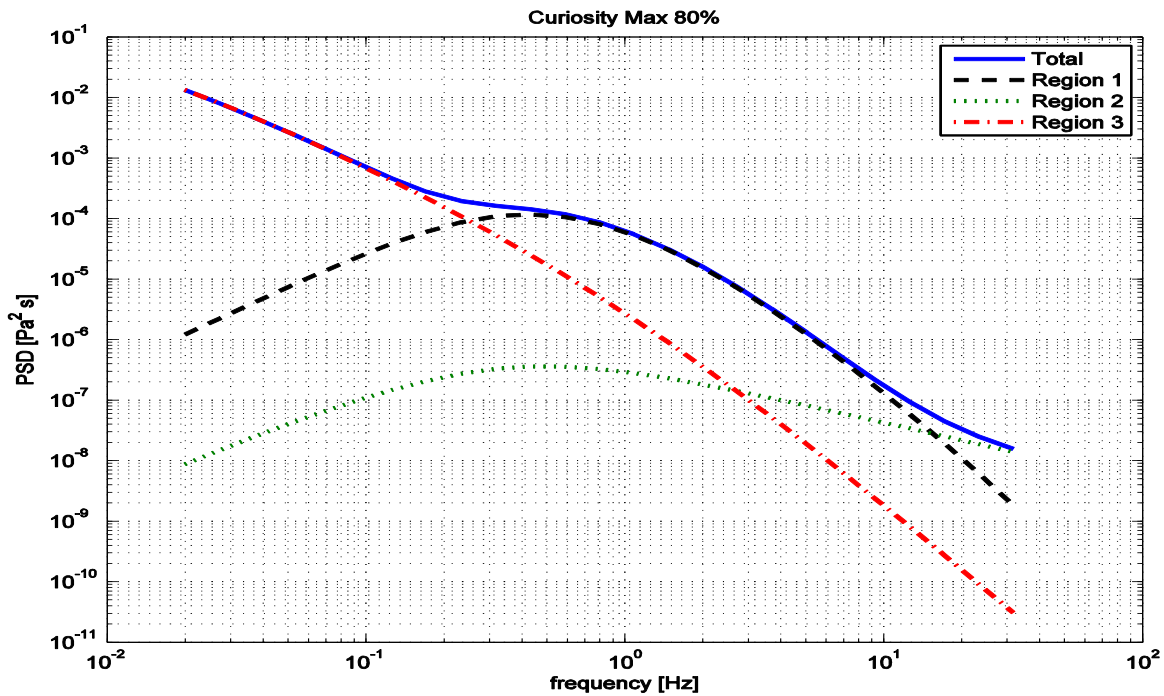
(b)



(c)



(d)



(e)

Figure 4.2. Power Spectral Density predictions of noise floor for Curiosity landing site with maximum velocity predictions utilized for fitting the velocity gradient. (a) 30%, (b) 40%, (c) 55%, (d) 65%, (e) 85% porosity.

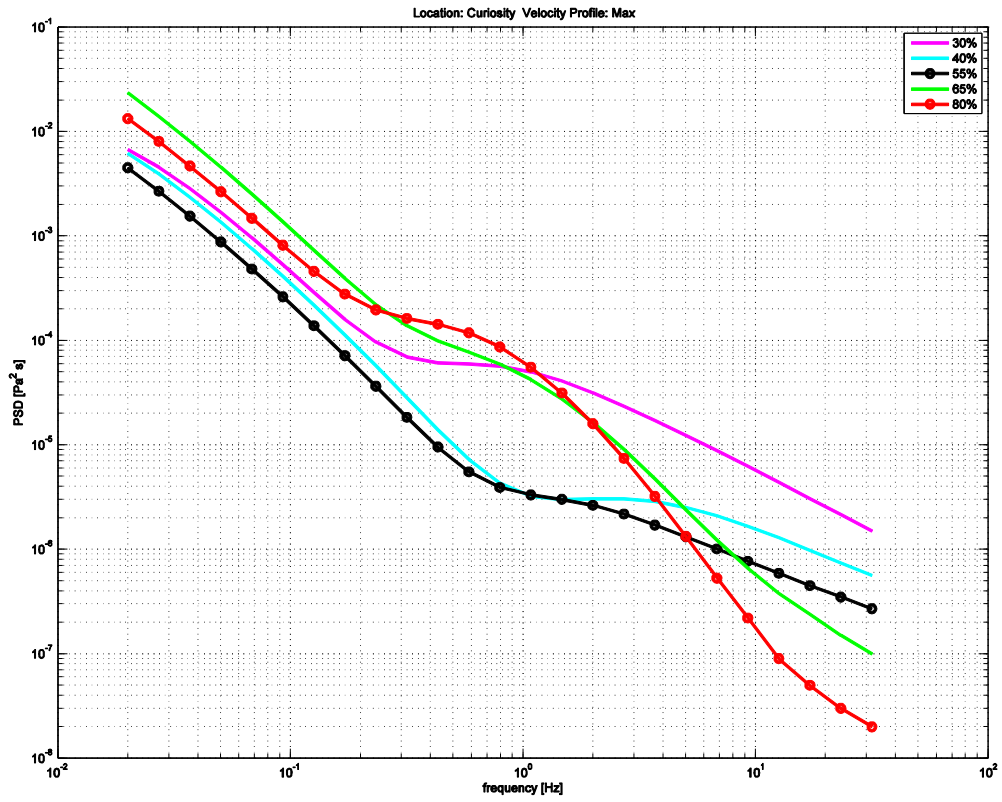


Figure 4.3. Comparisons of total wind noise contributions at center of domes of varying porosities.

Chapter 5: Discussion and Conclusion

We now have predicted power spectral density values for various locations, filter design, and wind scenarios on Mars. This allows us to gain an initial understanding of what type of intensities to expect from wind noise due to turbulence in Mars' lower atmosphere for infrasound through use of a porous dome filter. This information is pertinent in capturing and filtering infrasound at the Martian surface to study natural events. The results also provide future empirical studies with a theoretical estimation of baseline noise floor to compare measured values to when appropriate experimental data becomes available.

After close examination of the results presented in the previous chapter for the chosen location, it is clear that there are two filter porosities that mitigate wind noise the most, that being 55% and 80%. When examining data in the range of 0.02 to 5 Hz, the 55% porosity filter performed better yielding noise power spectral densities lower than that of the other porosities. For the range of 3 to 5 Hz, the 55% and 80% filters provide nearly the same value of predicted intensity. However, it is at the frequency of 6 Hz where the 80% filter begins to show signs of improvement over the 55% porosity and continues this trend up to 20 Hz. Further analysis of data at other locations appears to follow a similar trend where 55% works best for 0.02 to 5 Hz and 80% for 6 to 20 Hz. Since the 80% filter produces a lower reading over a larger range of frequencies, it would make it the ideal choice for use when listening for a multitude of infrasound sources in the respective range. If one's interest is in the 0 to 5 Hz range then the 55% filter would be a better option.

A prevalent feature throughout most locations and velocity profiles is that below 1 Hz Region 3 plays a dominating role in contribution to wind noise. The main mechanism for producing noise in this region is one of turbulence-turbulence and turbulence-shear interactions. Also within this frequency range it can be seen that for porosities of 30%, 40%, and 55% production mechanisms from Region 2, the fluctuating stagnation pressure, dominate those from Region 1, turbulence-turbulence and turbulence-shear inside the dome. Noticeable also are the facts that as the percentage increases from 30 to 55 percent contributions from Region 1 and Region 2 grow closer together. For the 65% porosity, contributions from Regions 1 and 2 become even closer where either of the two may dominate each other depending on the location and velocity profile utilized. It is then with 80% porosity where mechanisms from Region 1 are either dominant or match those of Region 2. This makes sense because as the surface area that makes up the porous dome decreases so does the stagnation pressure. For this reason, we should expect Region 1 mechanisms to become more dominate over Region 2 as porosity increases. Beyond 1 Hz either Region 1 or Region 2, based on filter porosity, will play the major role in predicted wind noise production versus that of Region 3.

An interesting application after analysis of these results would be to perform measurements on Earth with multiple domes nested inside one another. A possible set up to improve filtering over the entire infrasonic range would be to nest a 55% porous dome inside of an 80% porous dome and vice versa. After performing measurements on Earth one could adjust the values to Mars' atmosphere and generate what might be better wind noise reduction predictions as opposed to the use of only one filter. Though, the most ideal application for this data would be to compare it to measured data taken on Mars through 2-

meter dome filters of the varying porosities. Improvements to this data can also be made through use of measured wind profiles on Mars as opposed to theoretical ones generated by our general circulation model; however, at the present no known data of this kind exist.

Bibliography

- Abbott JohnPaul and Richard Raspet. 2015. Calculated wind noise for an infrasonic wind noise enclosure. *The Journal of the Acoustical Society of America* 138, no.1 (July): 332-43.
- Abbott JohnPaul. 2014. Optimization of Wind Fence Enclosures for Infrasonic Wind Noise Reduction. PhD diss., University of Mississippi.
- Anderson Jr. John D. 2010. *Fundamentals of Aerodynamics*. 5th ed. New York: The McGraw Hill Companies.
- Batchelor G. K. 1951. Pressure fluctuations in isotropic turbulence. *Mathematical Proceedings of the Cambridge Philosophical Society* 47:359-74.
http://journals.cambridge.org/abstract_S0305004100026712.
- Colaitis A., A. Spiga, F. Hourdin, C. Rio, F. Forget, and E. Millour. A thermal plume model for the Martian convective boundary layer. *Journal of Geophysical Research: Planets* 118, no. 7 (July): 1468-87.
- Cole G. H. A. 1962. *Fluid Dynamics*. New York: John Wiley & Sons Inc.
- Daniels Fred B. 1958. Noise-Reducing Line Microphone for Frequencies below 1 cps. *The Journal of the Acoustical Society of America* 31, no. 4 (April): 529-31.
- De Groot-Hedlin, C.D., Hedlin, M.A.H., and Drob, D., 2010, Atmospheric variability and infrasound monitoring, in “Infrasound Monitoring for Atmospheric Studies”, eds. A. Le Pichon, E. Blanc, and A. Hauchecorne, Springer Geosciences, 475-507

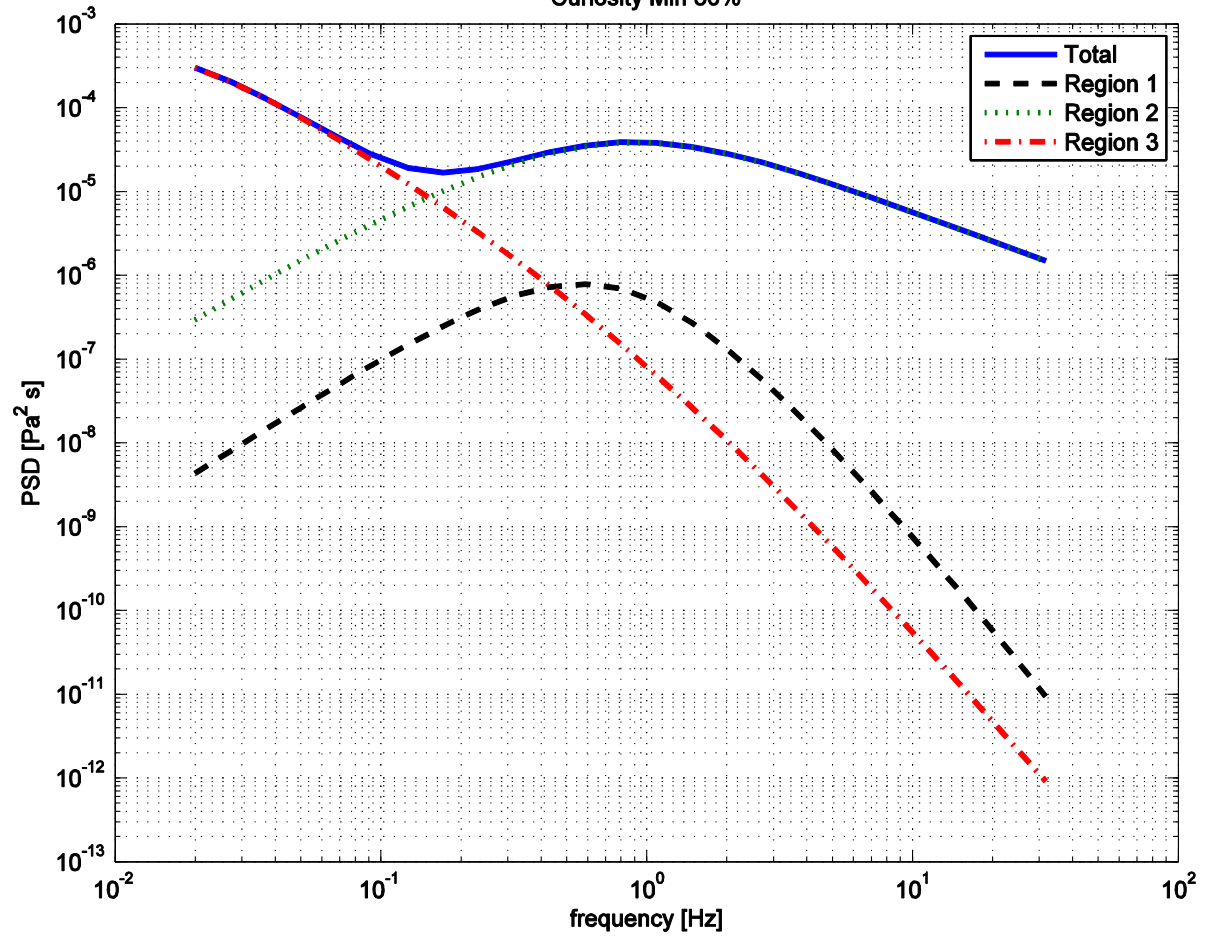
- Dolas Prakash M. and Kumar Karanam Kishore. 2009. Retrieval of static stability parameter from the radiosonde/rawinsonde ascent rate profiles: a wavelet approach. *Annales Geophysicae* 27:547-53. www.ann-geophys.net/27/547/2009.
- Francois Forget, Frederic Hourdin, Richard Fournier, Christophe Houdin, Olivier Talagrand, Mathew Collins, Stephen R. Lewis, Peter L. Read, and Jean-Paul Huot. Improved general circulation models of the Martian atmosphere from the surface to above 80 km. *Journal of Geophysical Research* 104, no. E10 (October): 24155-76.
- George William K., Paul D. Beuther, and Roger E. A. Arndt. 1984. Pressure spectra in turbulent free shear flows. *Journal of Fluid Mechanics* 148:155-91.
- Kármán Theodore von. 1948. Progress in the Statistical Theory of Turbulence. *Proceeding of the National Academy of Sciences of the United States of America* 34, no. 11 (November): 530-39.
- Kraichnan Robert H. 1955. Pressure Field within Homogeneous Anisotropic Turbulence. *The Journal of the Acoustical Society of America* 28, no. 1 (January): 64-72.
- Kraichnan Robert H. 1955a. Pressure Fluctuations in Turbulent Flow over a Flat Plate. *The Journal of the Acoustical Society of America* 28, no. 3 (May): 378-90.
- Landau L. D. and Lifshitz E. M. 1959. *Fluid Mechanics*. 3rd ed. Vol. 6 of *Course of Theoretical Physics*. Long Island City: Pergamon Press.
- Mars Climate Database. www-mars.lmd.jussieu.fr/mcd_python/ (accessed June 2015-October 2016).
- Martinez German, Francisco Valero, Luis Vazquez. 2009. Characterization of the Martian Convective Boundary Layer. *Journal of Atmospheric Sciences* 66:2044-58.

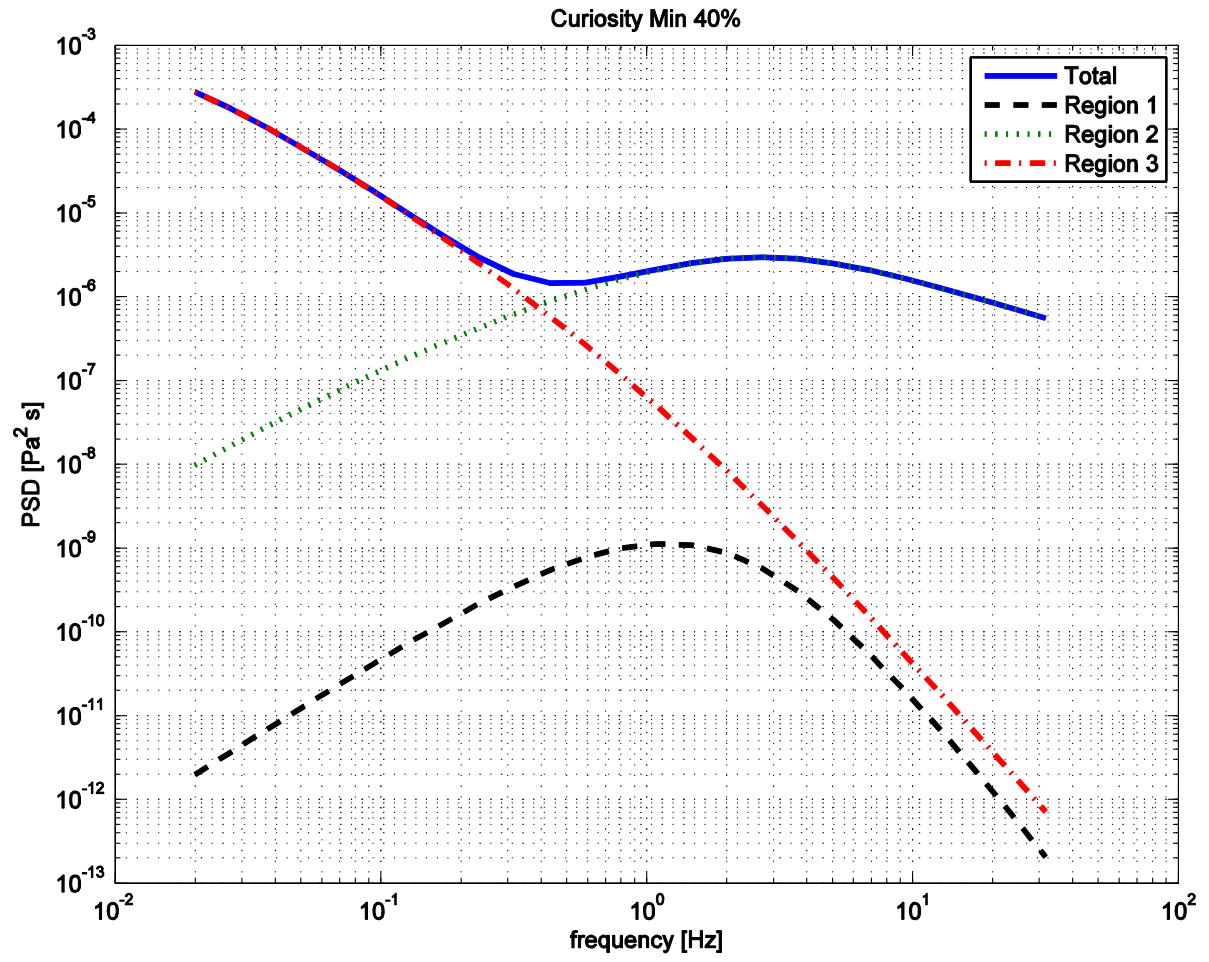
- McIlveen Robin. 1992. *Fundamentals of Weather and Climate*. 2nd ed. London: Chapman & Hall.
- Millour E. The Mars Climate Database (MCD version 5.2). *European Planetary Science Congress 10*, no. EPSC2015-438.
- Monin A. S. and Yaglom A. M. 1971. *Statistical Fluid Mechanics*. Cambridge: The MIT Press.
- NASA Planetary Data System. <https://pds.nasa.gov> (accessed June 2015-October 2016).
- Noble John M., W.C. Kirkpatrick Alberts II, Sandra L. Collier, Richard Raspet, and Mark A. Coleman. 2014. *Wind Noise Suppression for Infrasound Sensors*. Adelphi: Army Research Laboratory.
- Panofsky Hans A. and Dutton John A. 1984. *Atmospheric Turbulence*. New York: John Wiley & Sons.
- Petrosyan A., B. Glaperin, S. E. Larsen, S. R. Lewis, A. Maattanen, P. L. Read, N. Renno, L. P. H. T. Rogberg, H. Savijarvi, T. Siili, A. Spiga, A. Toigo, and L. Vazquez. 2011. The Martian Atmospheric Boundary Layer. *Reviews of Geophysics* 49, no. RG3005 (2011): 1-46.
- Pope Stephen B. *Turbulent Flows*. 2000. Cambridge: Cambridge University Press.
- Raspet Richard, Jeremy Webster, and Kevin Dillion. 2006. Framework for wind noise studies. *The Journal of the Acoustical Society of America* 119, no. 2 (February): 834-43.
- Raspet Richard, Jiao Yu, and Jeremy Webster. 2007. Low frequency wind noise contributions in measurement microphones. *The Journal of the Acoustical Society of America* 123, no. 3 (March): 1260-69.

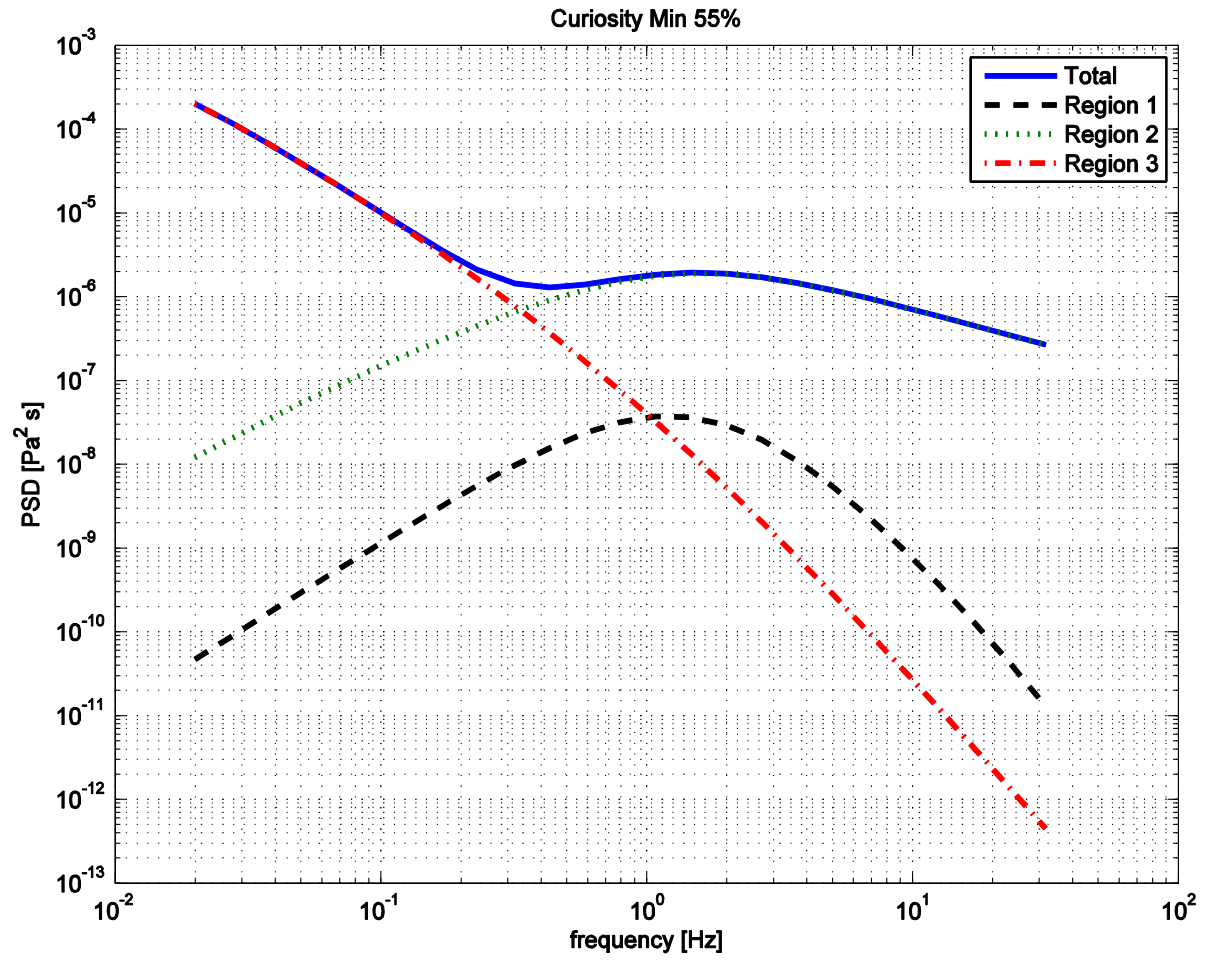
- Raspet Richard, Collier L. Sandra, Noble M. John, Kirkpatrick W.C. Alberts II, Webster Jeremy, and Abbott JohnPaul. 2014. Analysis of Wind Noise Reduction by Semi-Porous Fabric Domes. *Journal of the Acoustical Society of America* 136.
- Savijarvi Hannu and Janne Kauhanen. 2008. Surface and boundary-layer modeling for the Mars Exploration Rover sites. *Quarterly Journal of the Royal Meteorological Society* 134 (April): 635-41.
- Shields Douglas F. 2005. Low-frequency wind noise correlation in microphone arrays. *Journal of the Acoustical Society of America* 117 no. 6 (June): 3489-96.
- Taylor G. I. 1937. The spectrum of turbulence. *Proceedings of the Royal Society of London. Series A, Mathematical and Physical Sciences* 919 (February): 476-90.
- Tennekes H. and J. L. Lumley. 1972. *A First Course in Turbulence*. Cambridge: The MIT Press.
- Walker Kristoffer T. and Michael A. H. Hedlin. 2010. "A Review of Wind-Noise Reduction Methodologies." In *Infrasound Monitoring for Atmospheric Studies*, 141-82. New York: Springer Science.
- Yu Jiao. 2009. Calculation of Wind Noise Measured at the Surface under Turbulent Wind Fields. PhD diss. University of Mississippi.
- Yu Jiao, Richard Raspet, Jeremy Webster, and JohnPaul Abbott. 2011. Improved prediction of the turbulence shear contribution to wind noise pressure spectra. *The Journal of the Acoustical Society of America* 130, no. 6 (December): 3590-94.
- Yu Jiao, Richard Raspet, Jeremy Webster, and JohnPaul Abbott. 2010. Wind noise measured at the ground surface. *The Journal of the Acoustical Society of America* 129, no. 2 (February): 622-32.

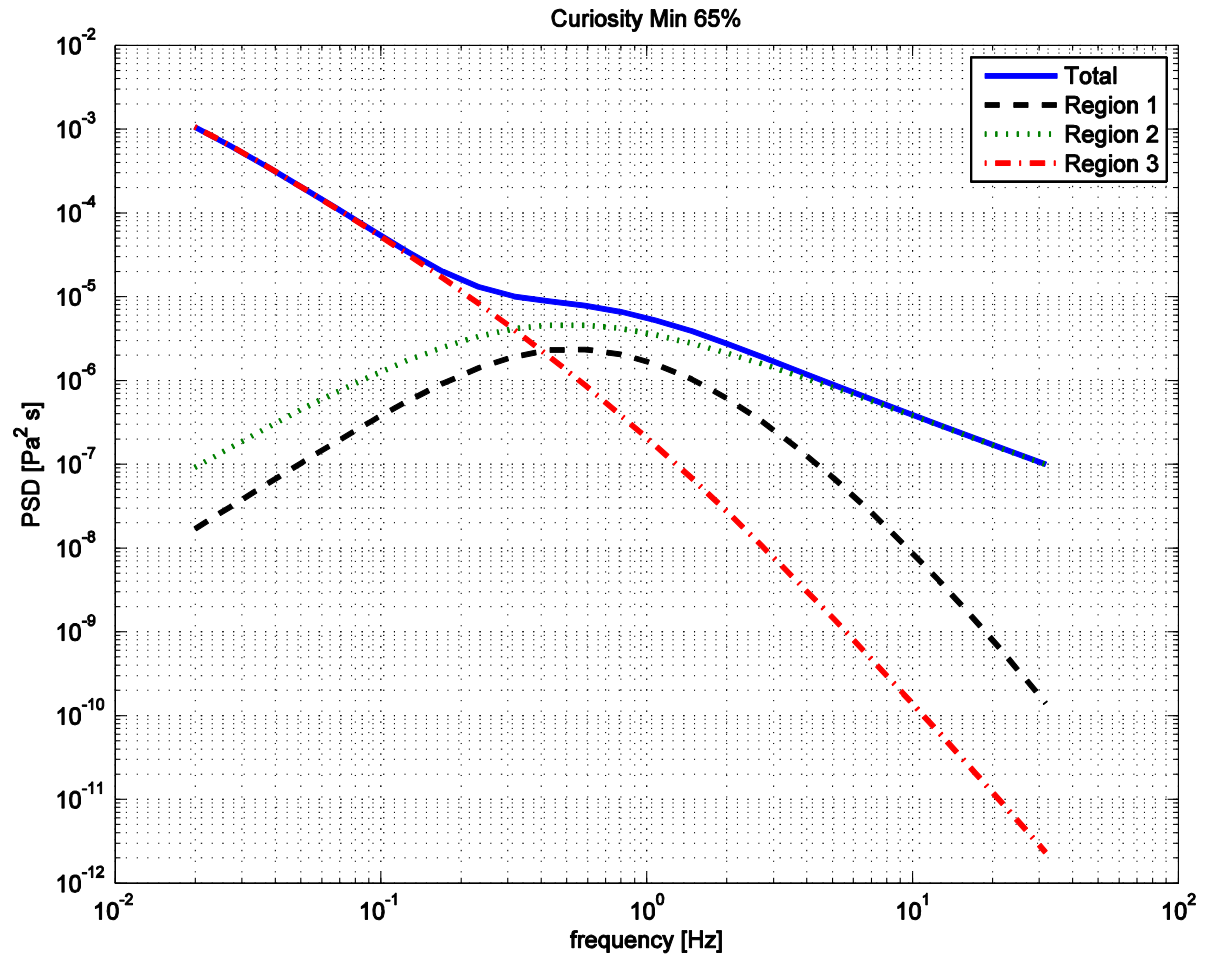
Appendix

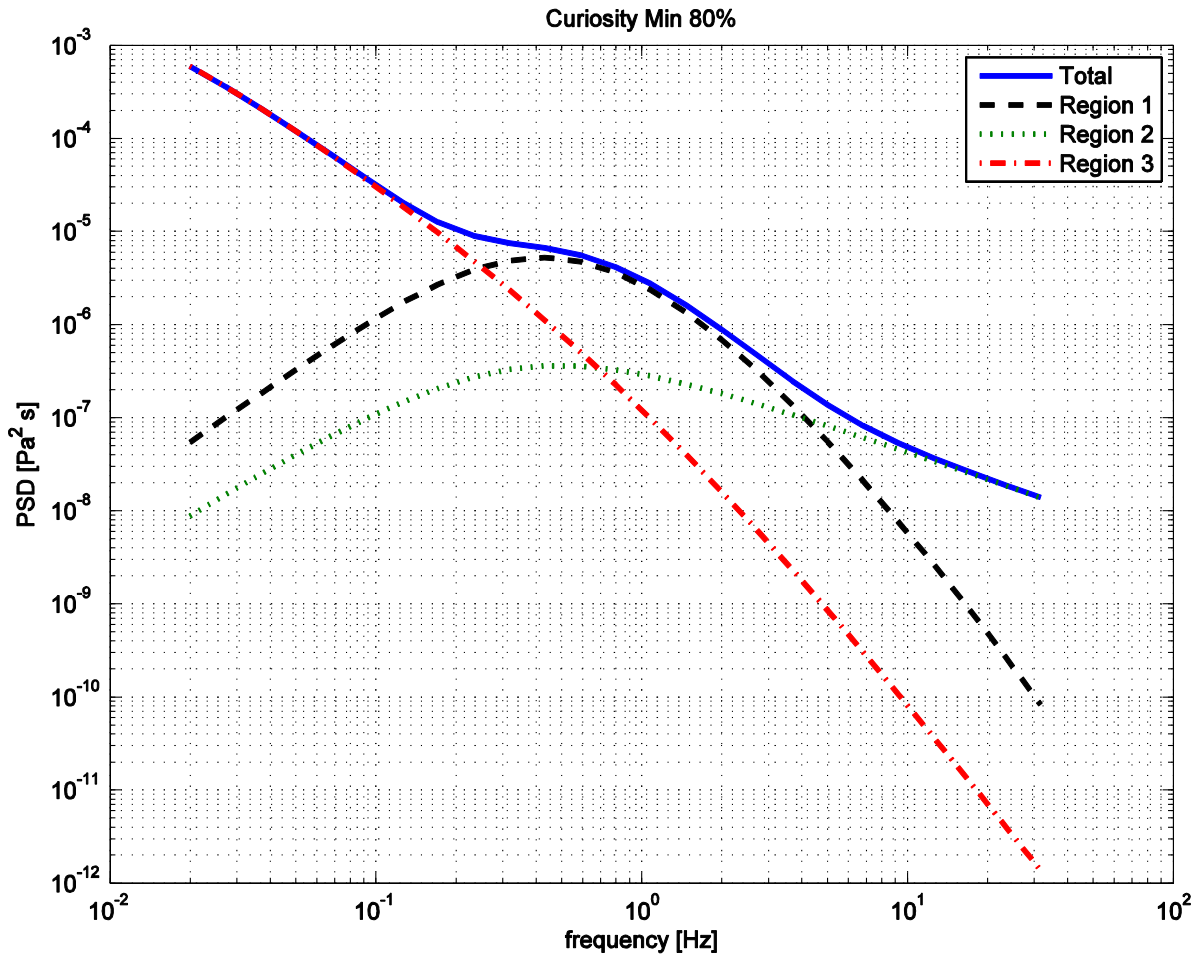
Curiosity Min 30%

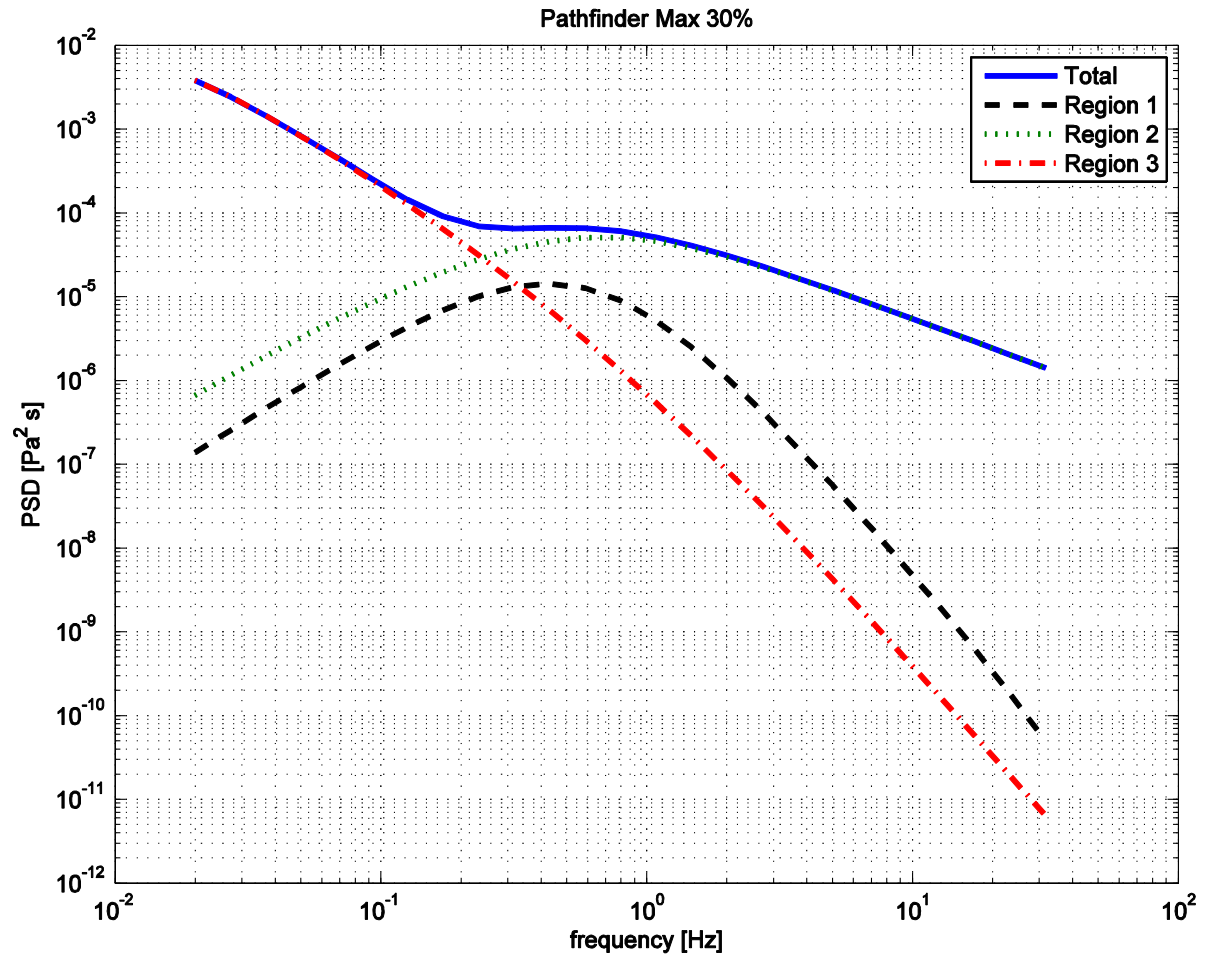


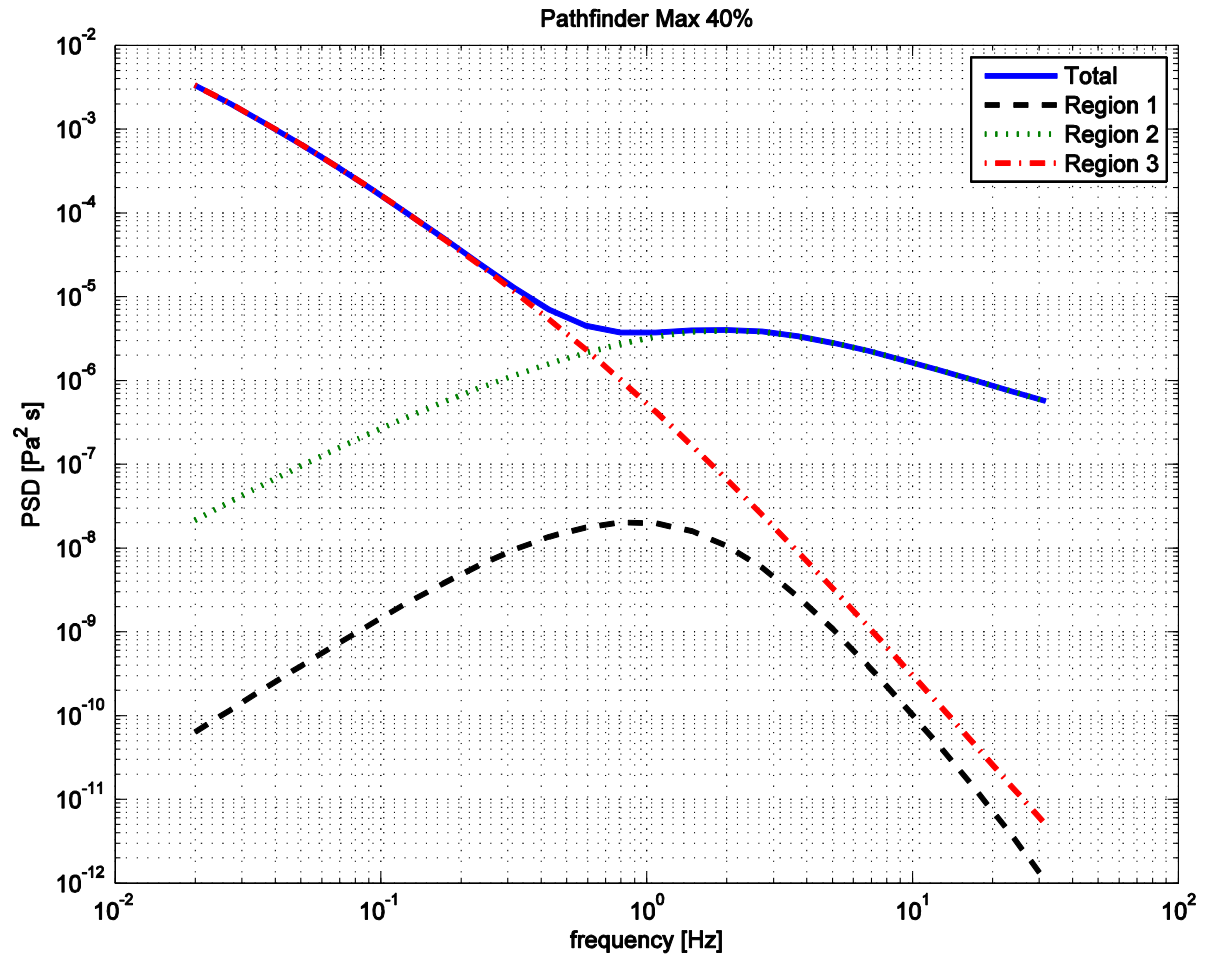


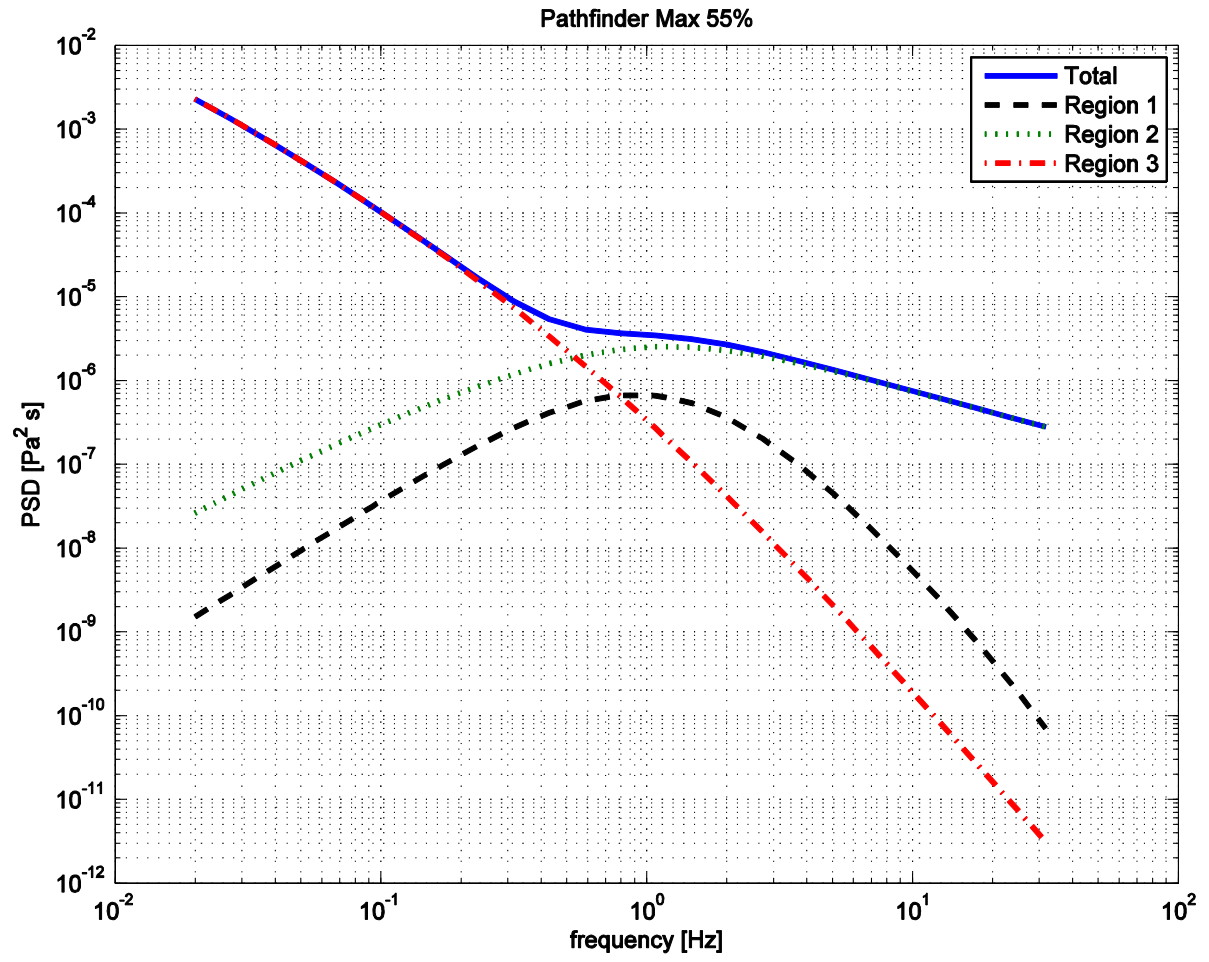


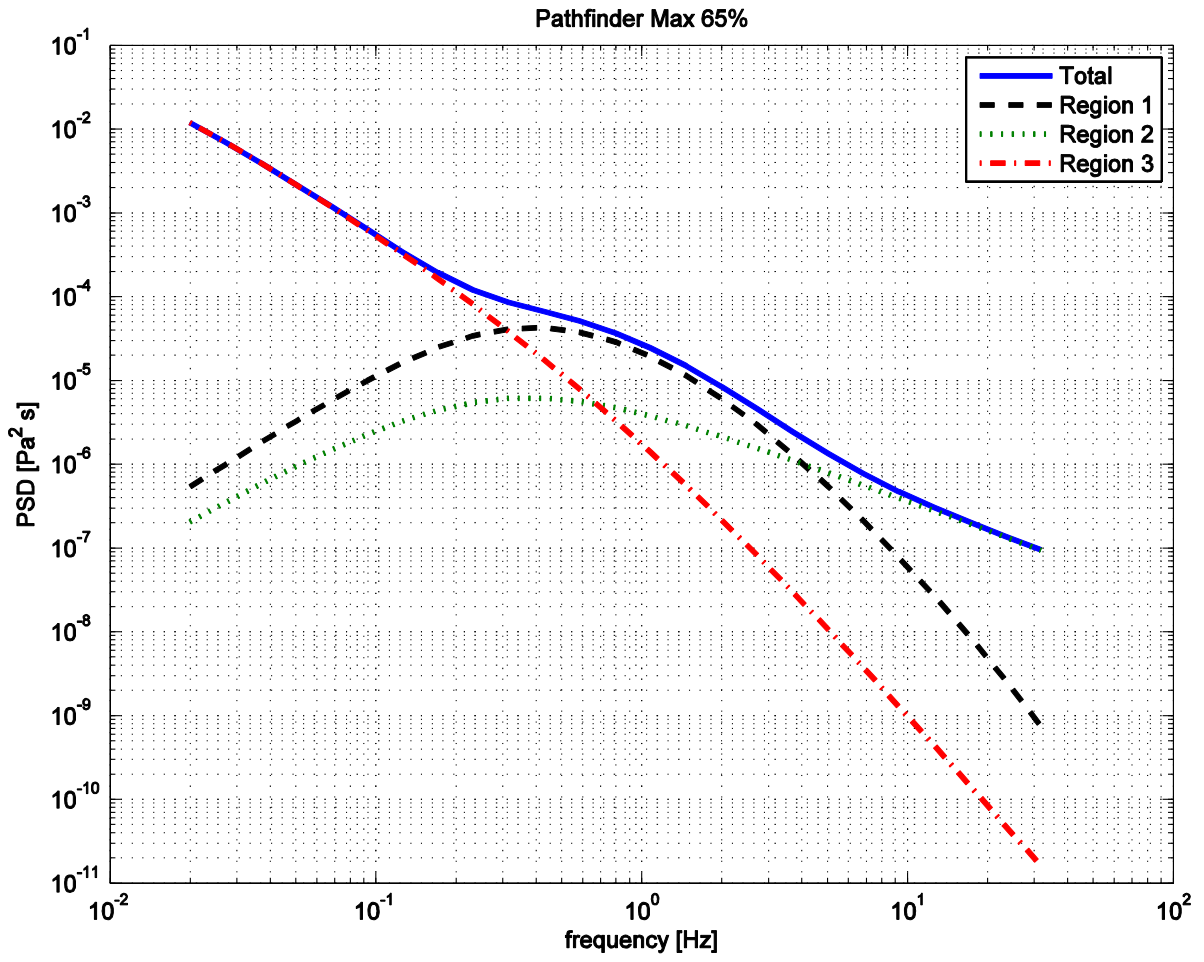


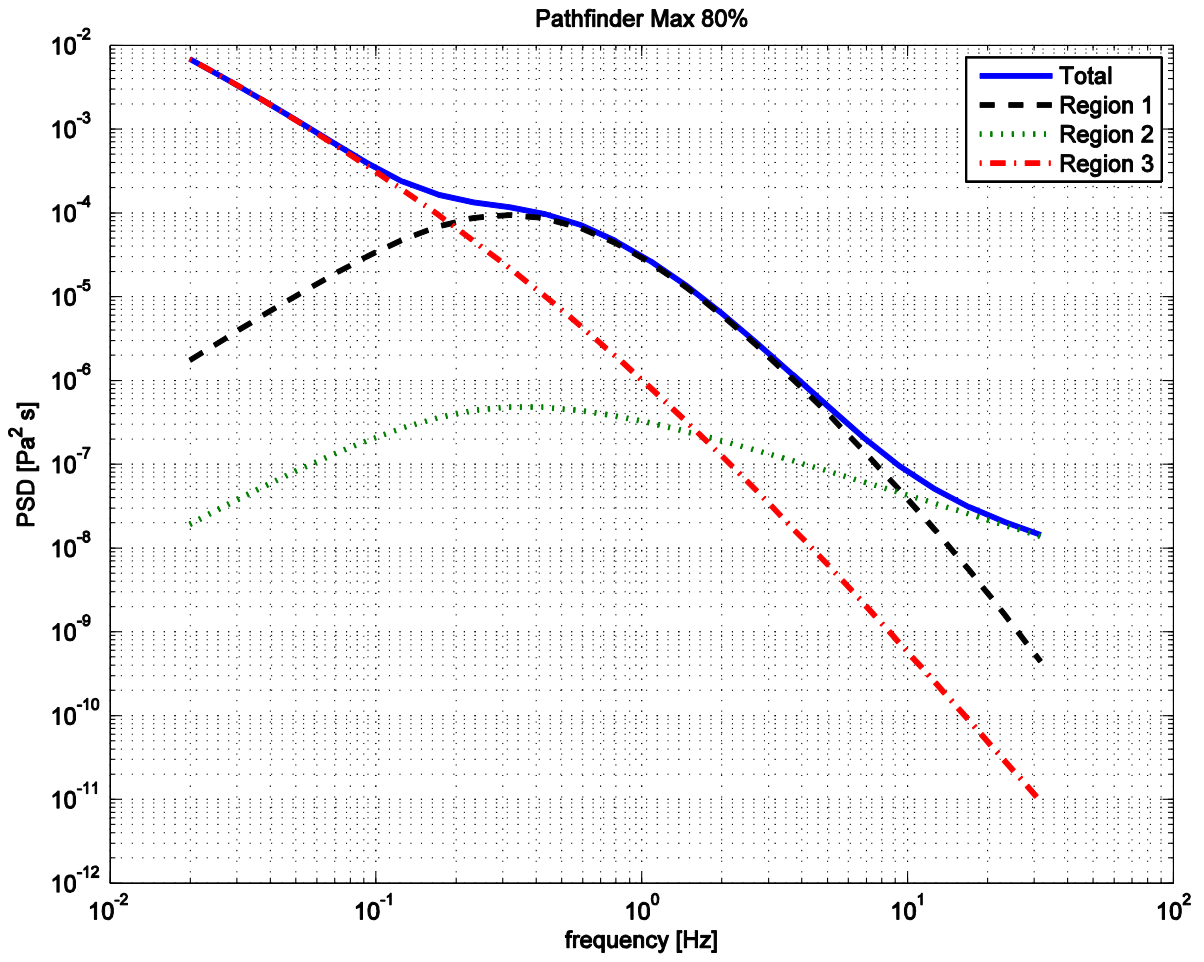


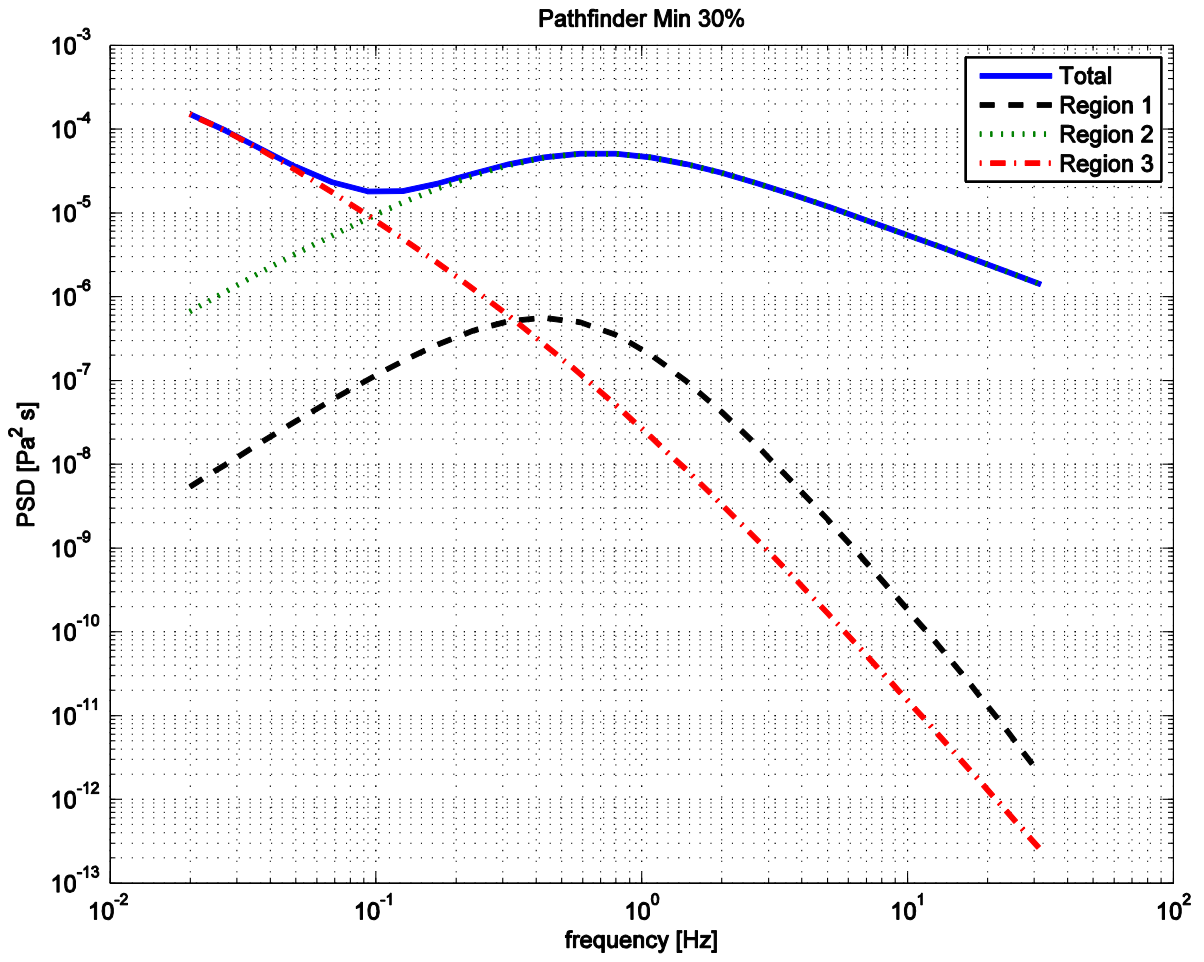


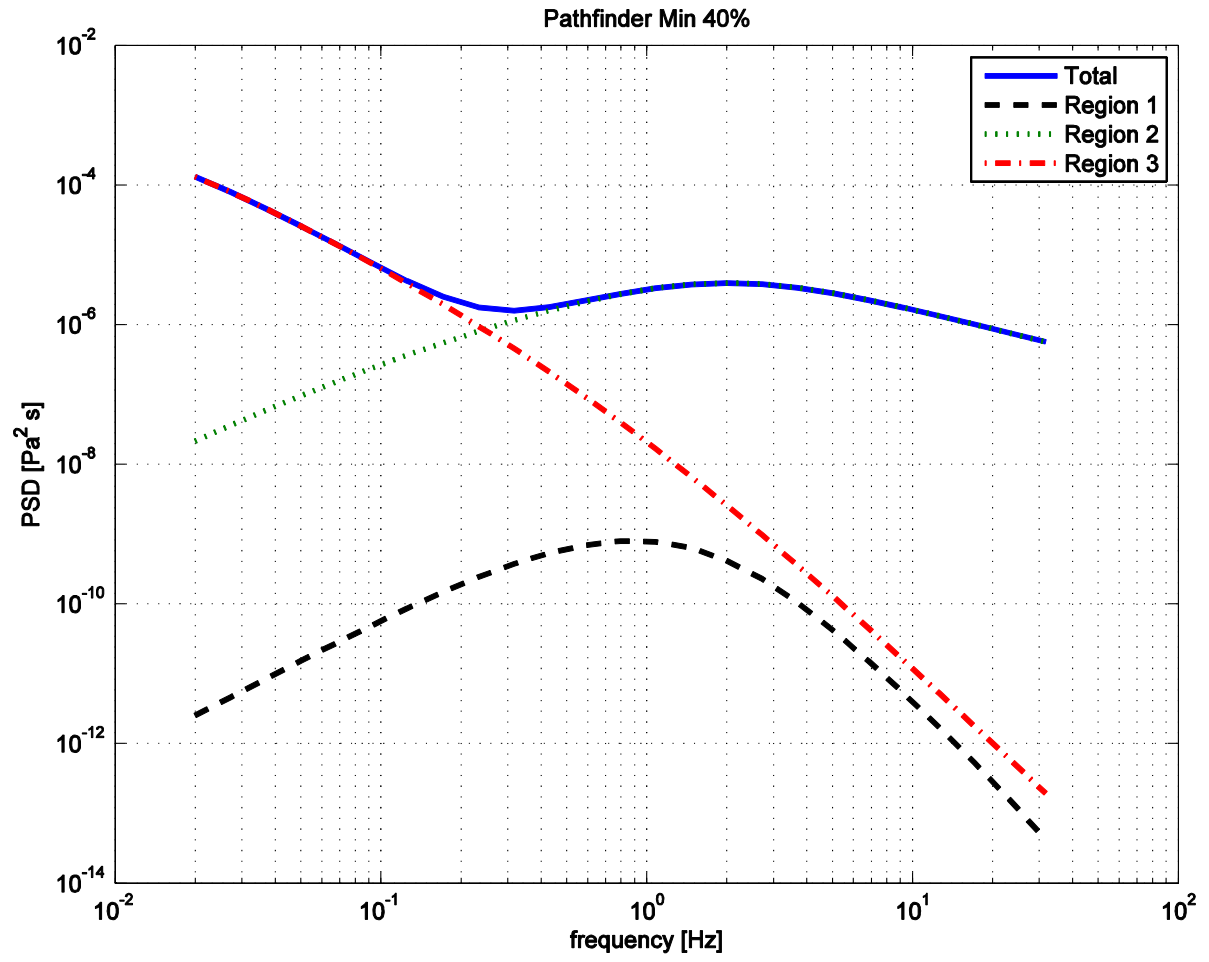


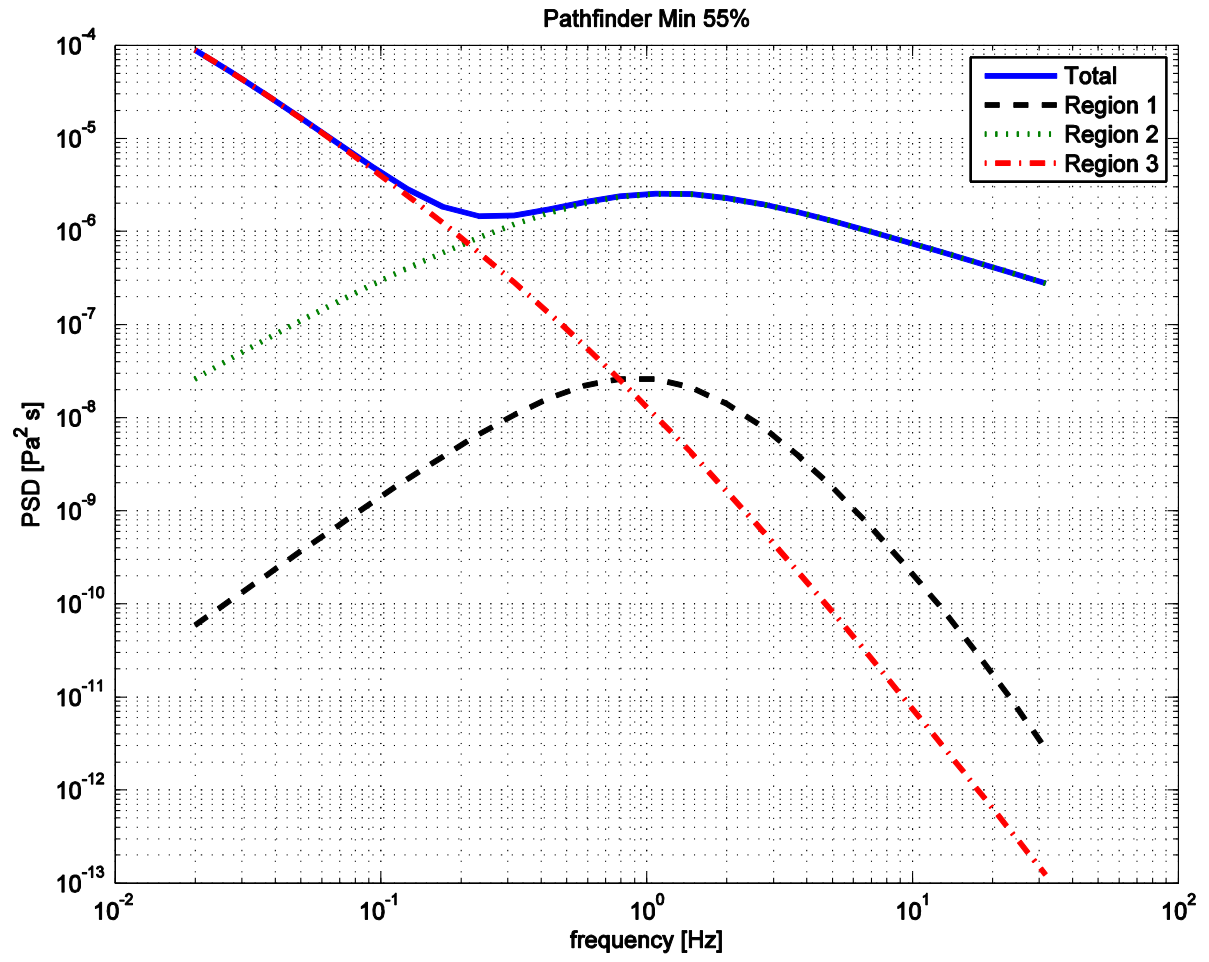


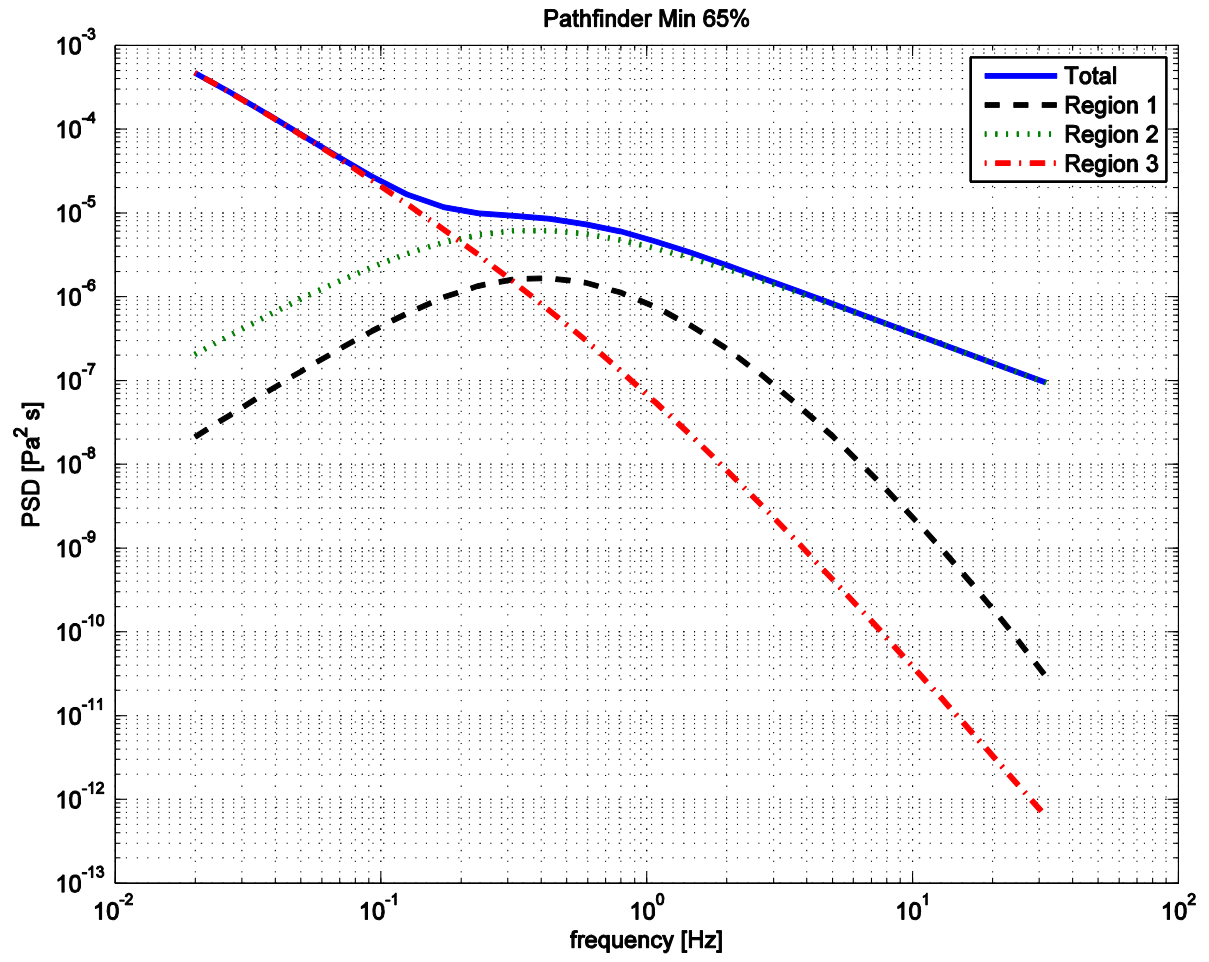


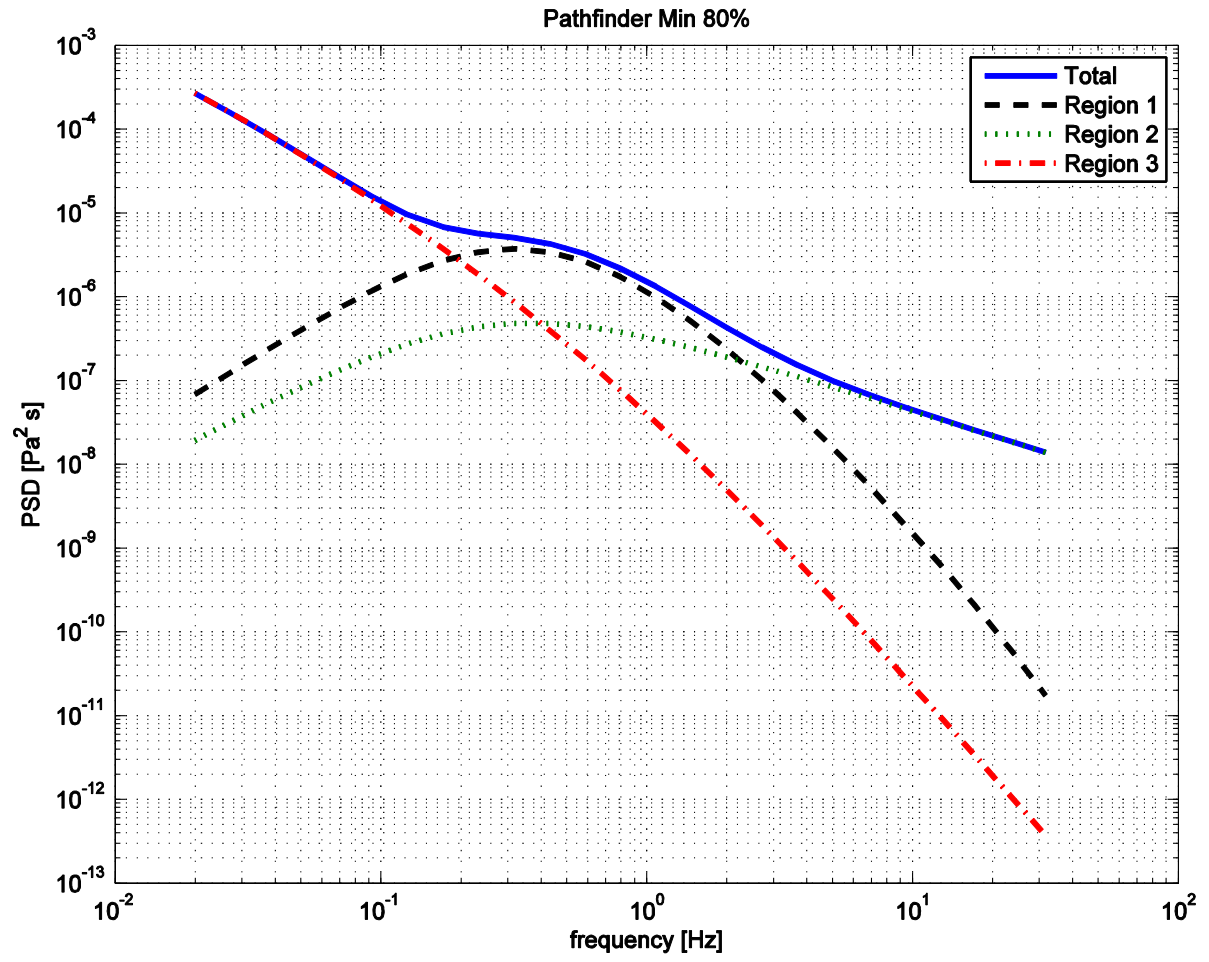


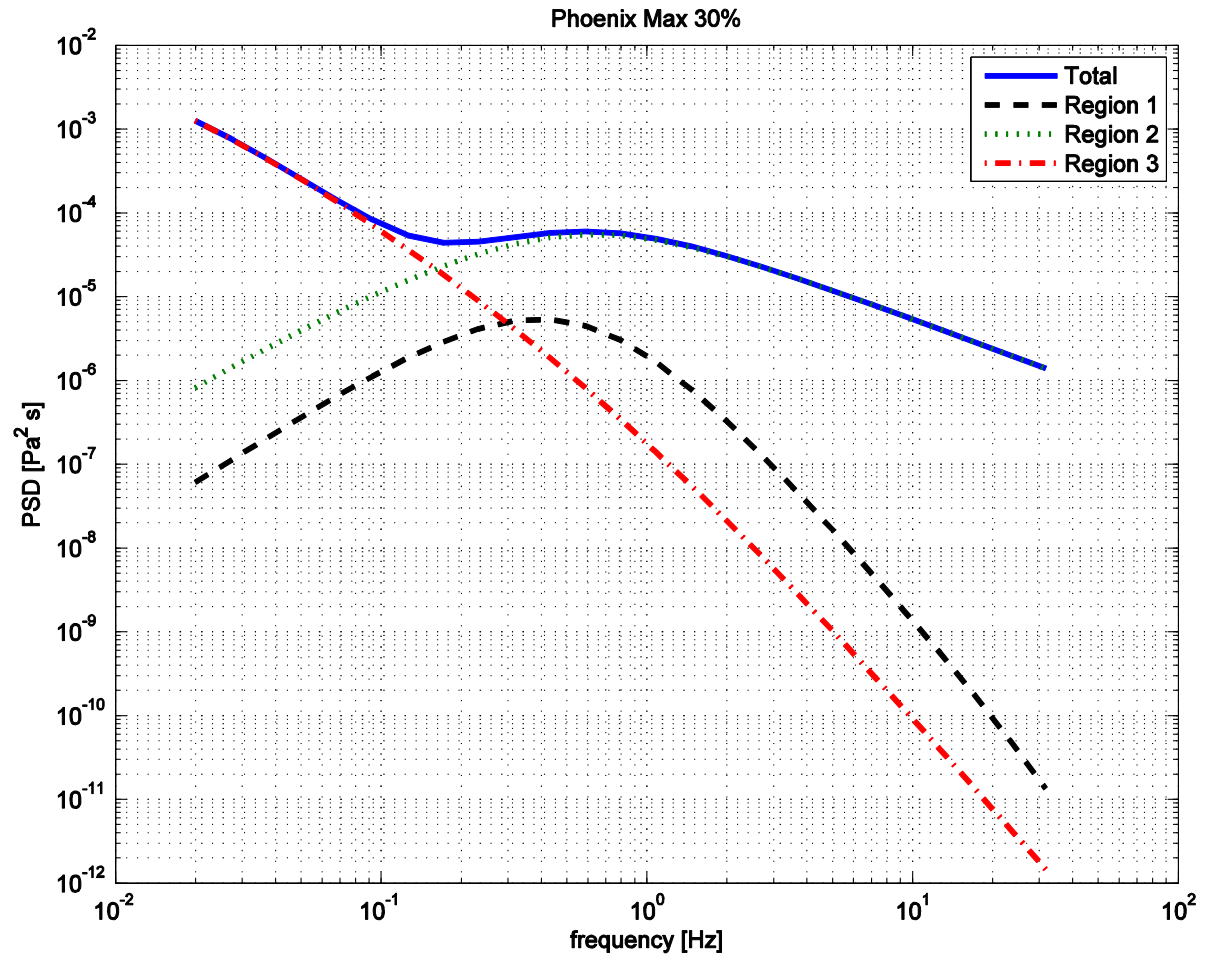


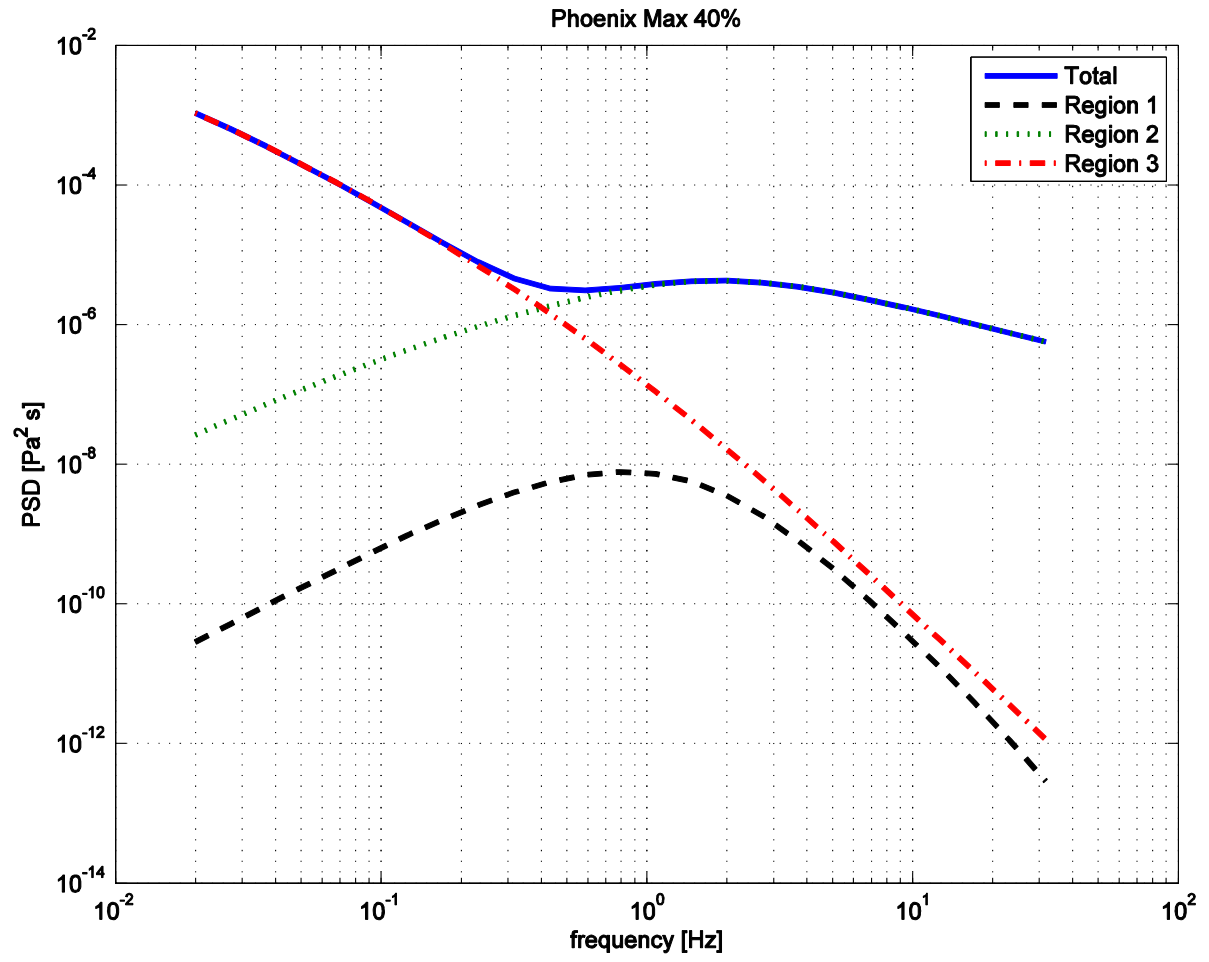


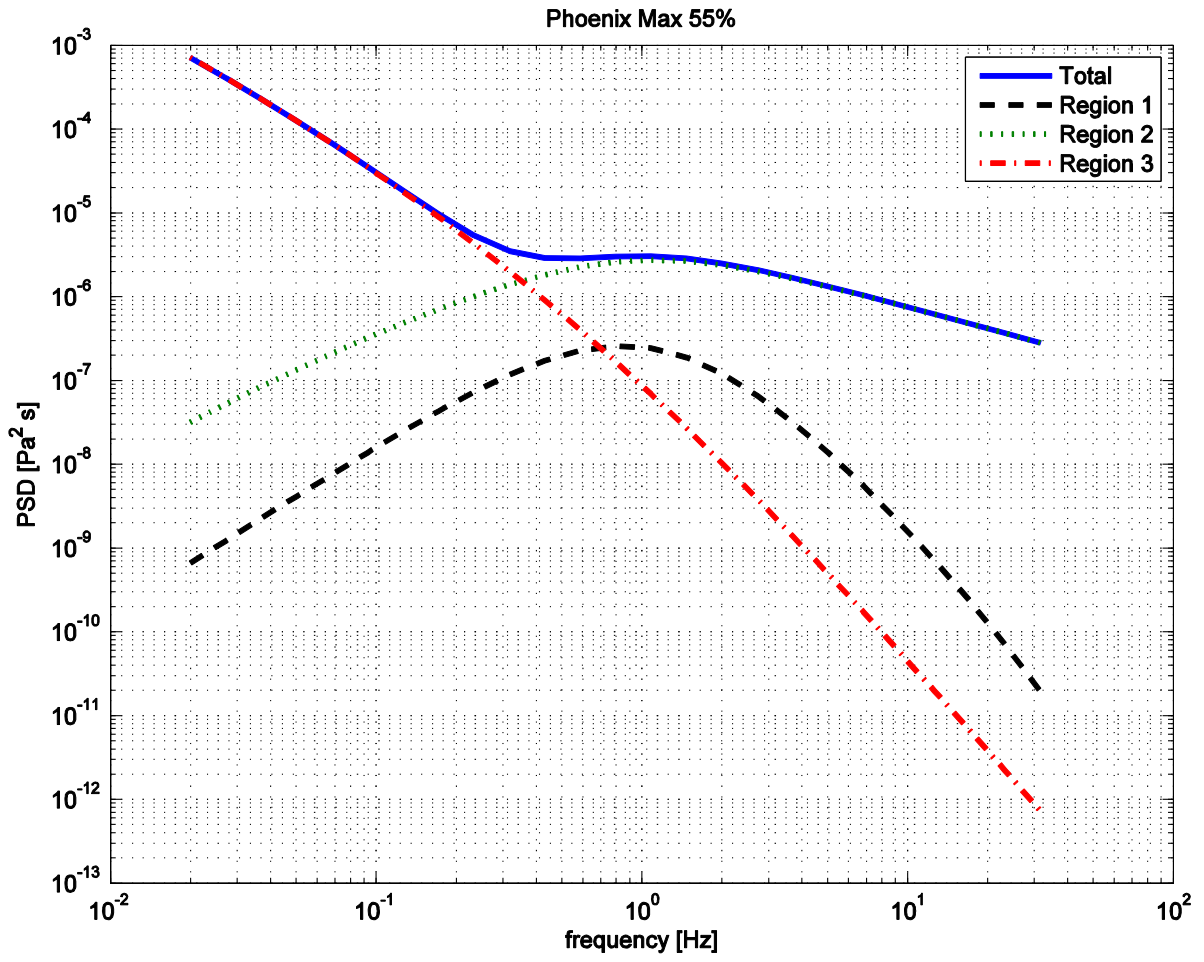


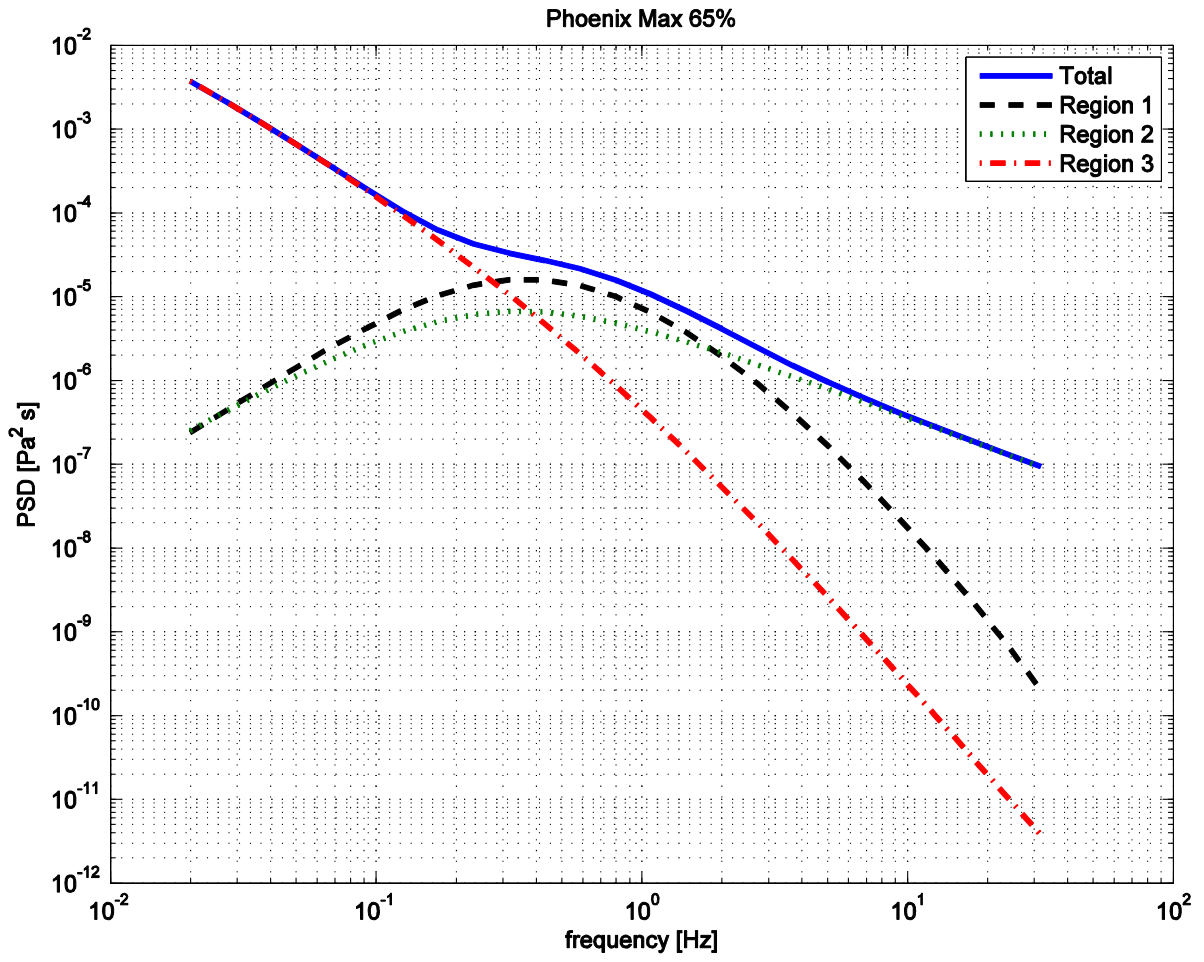




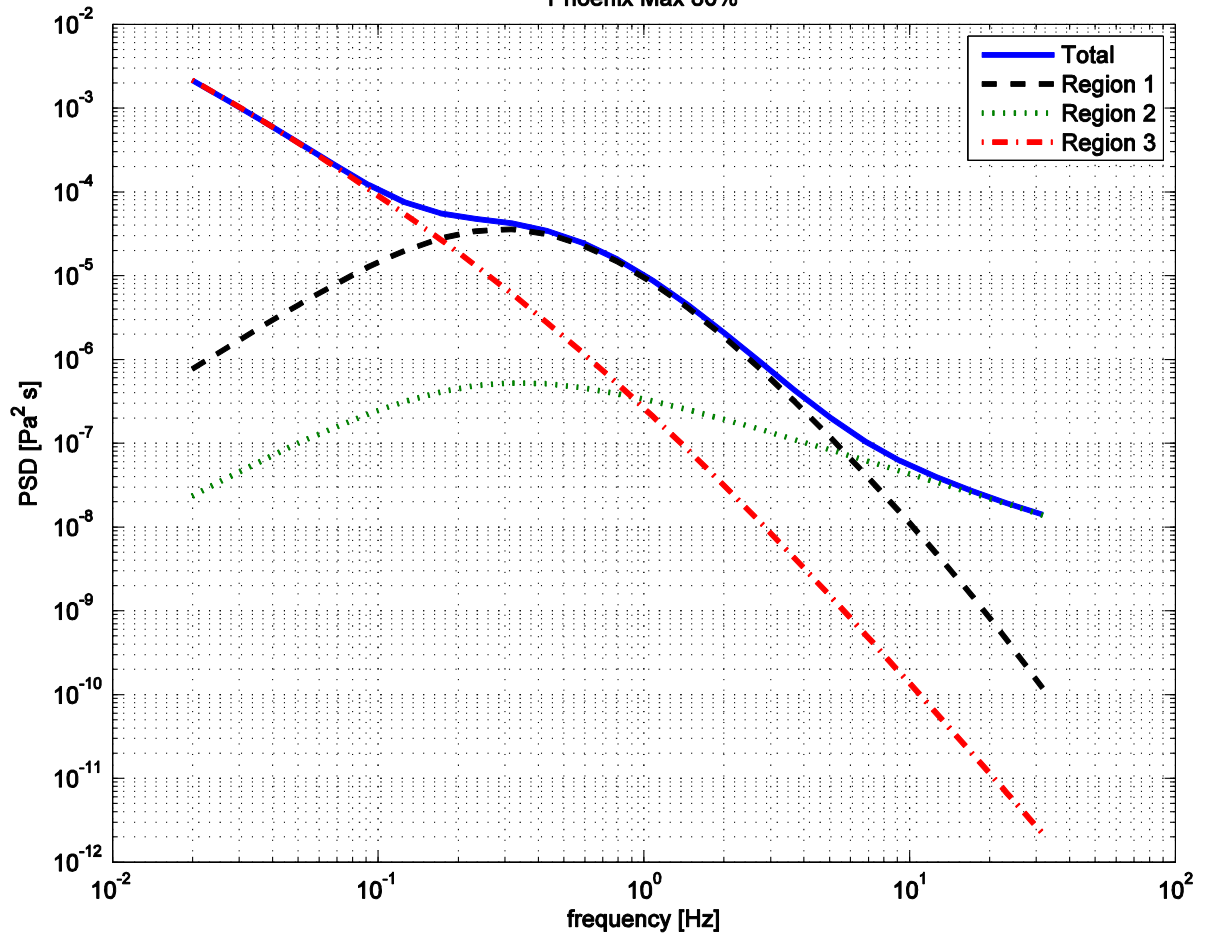


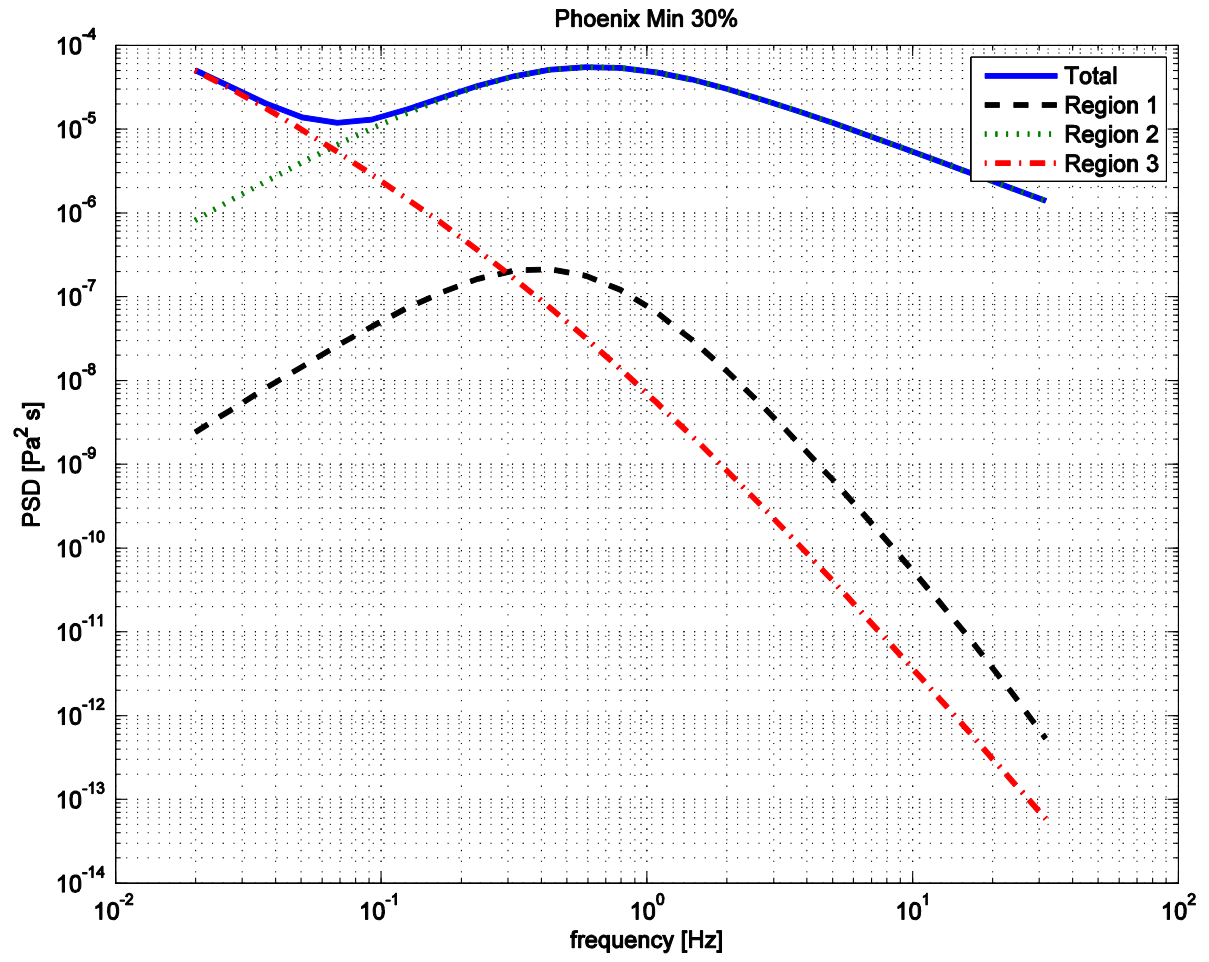


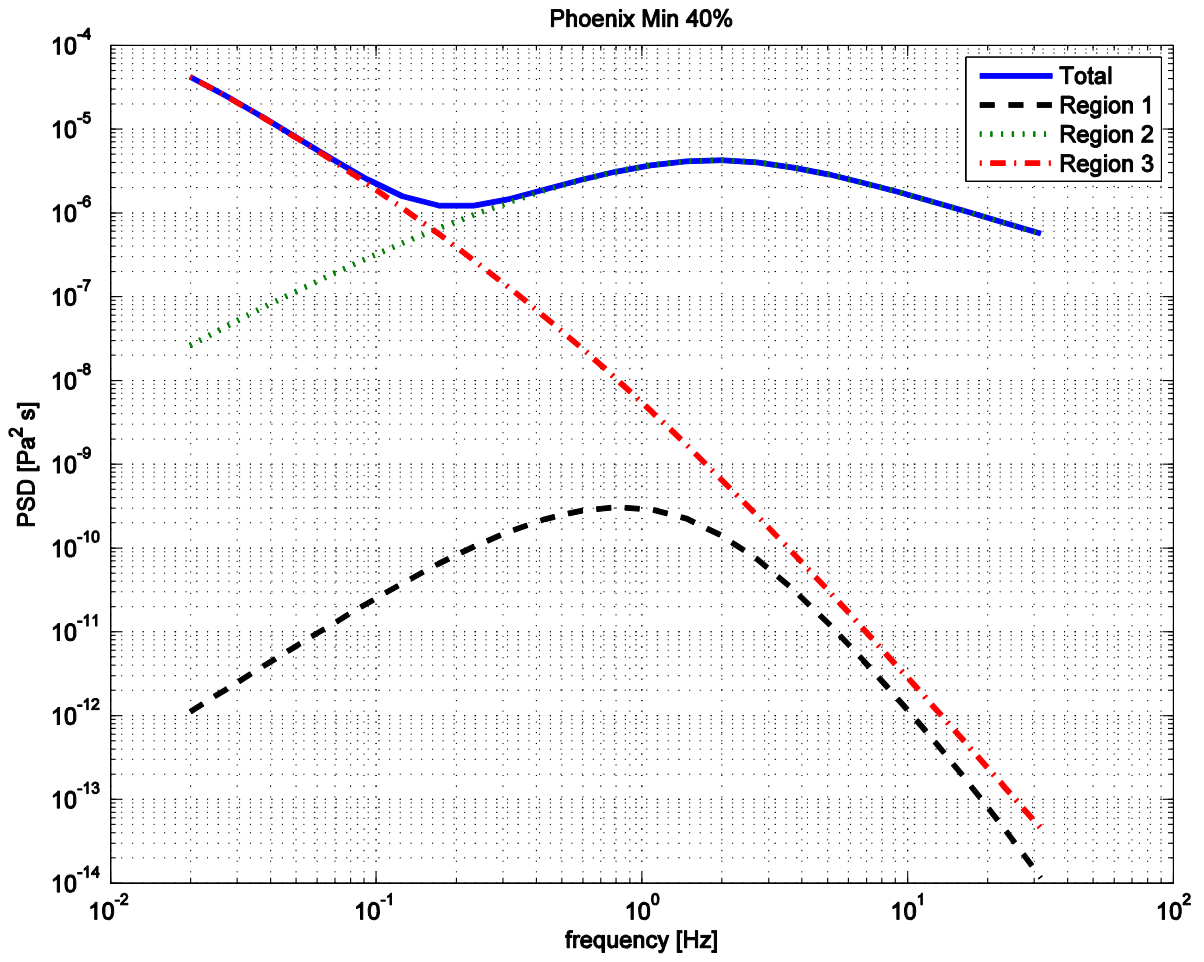


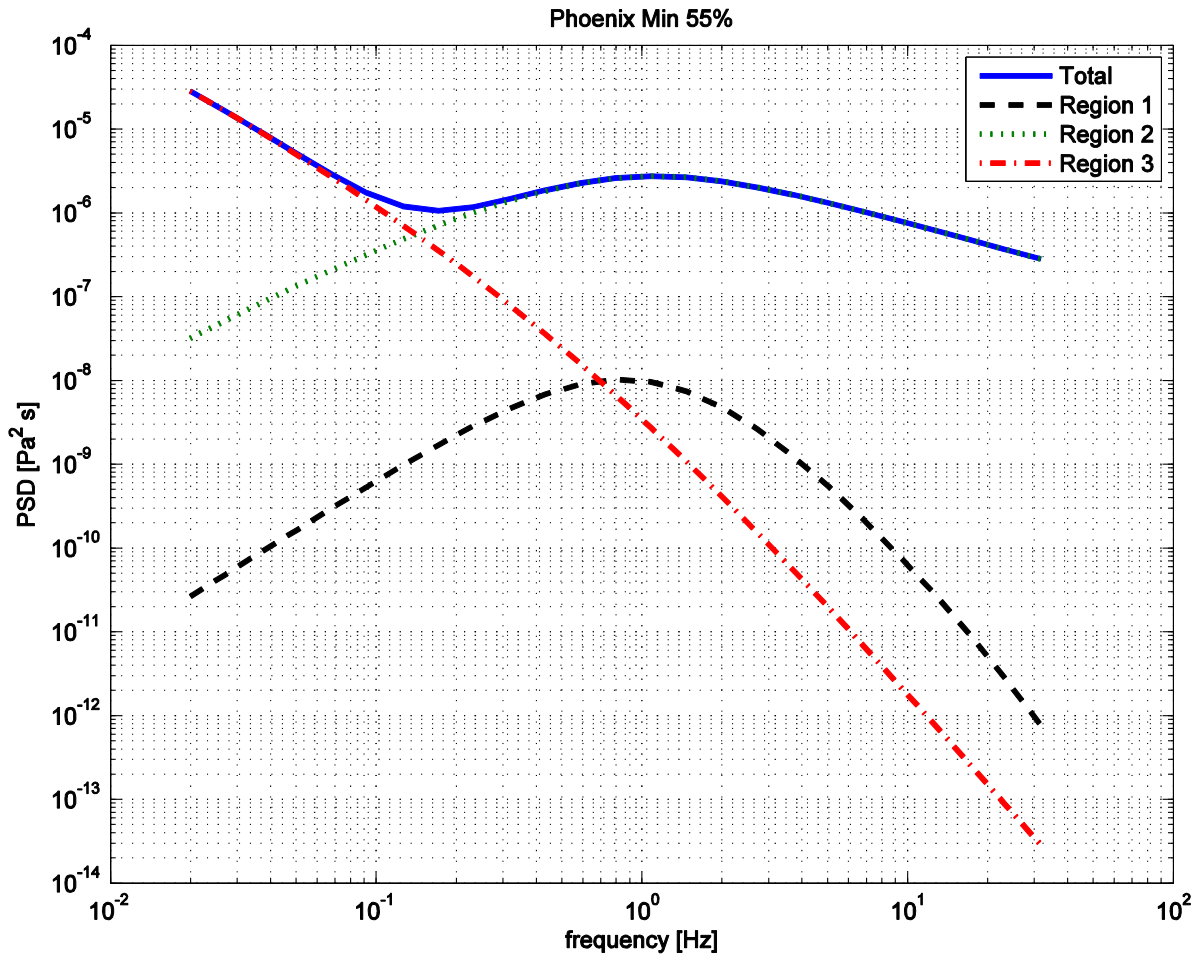


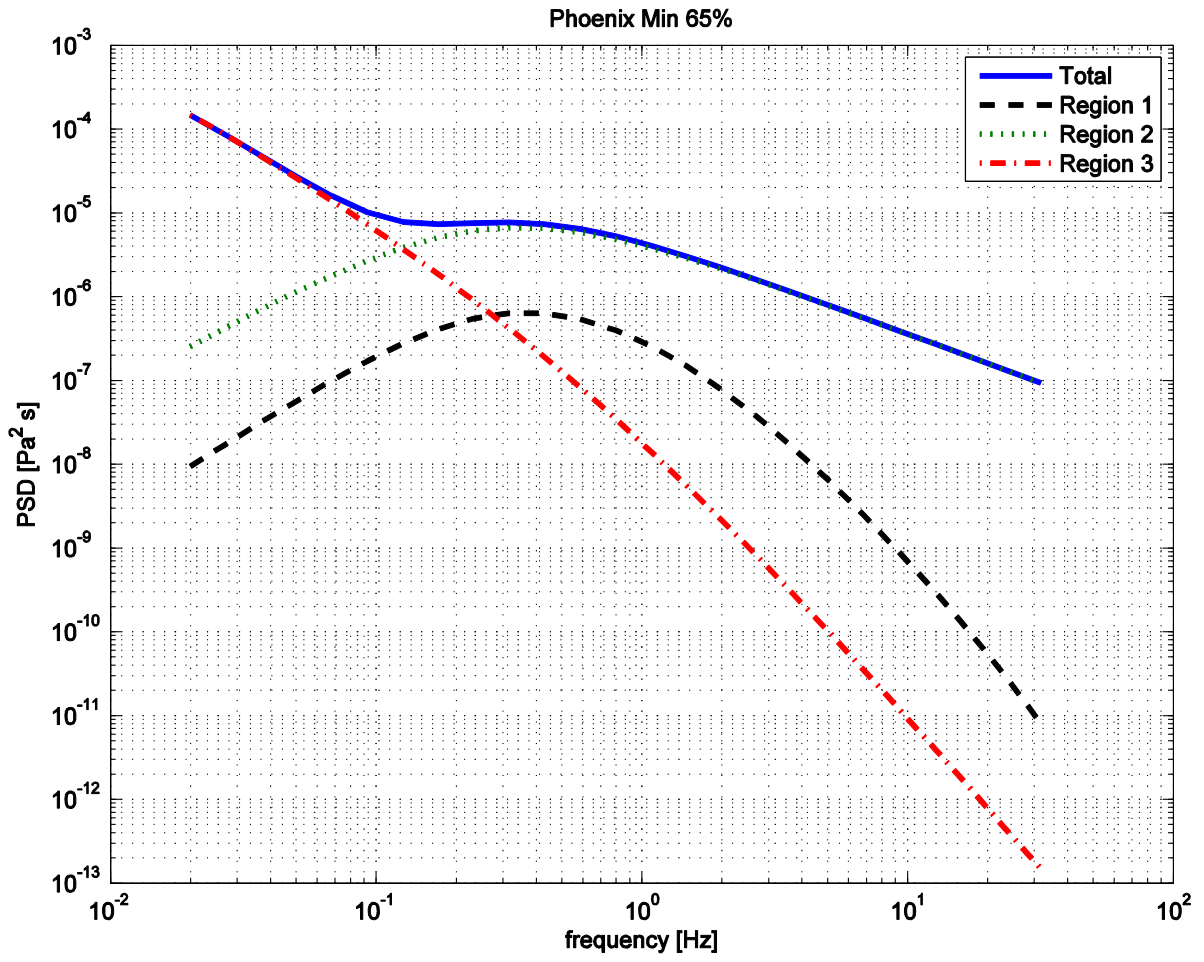
Phoenix Max 80%

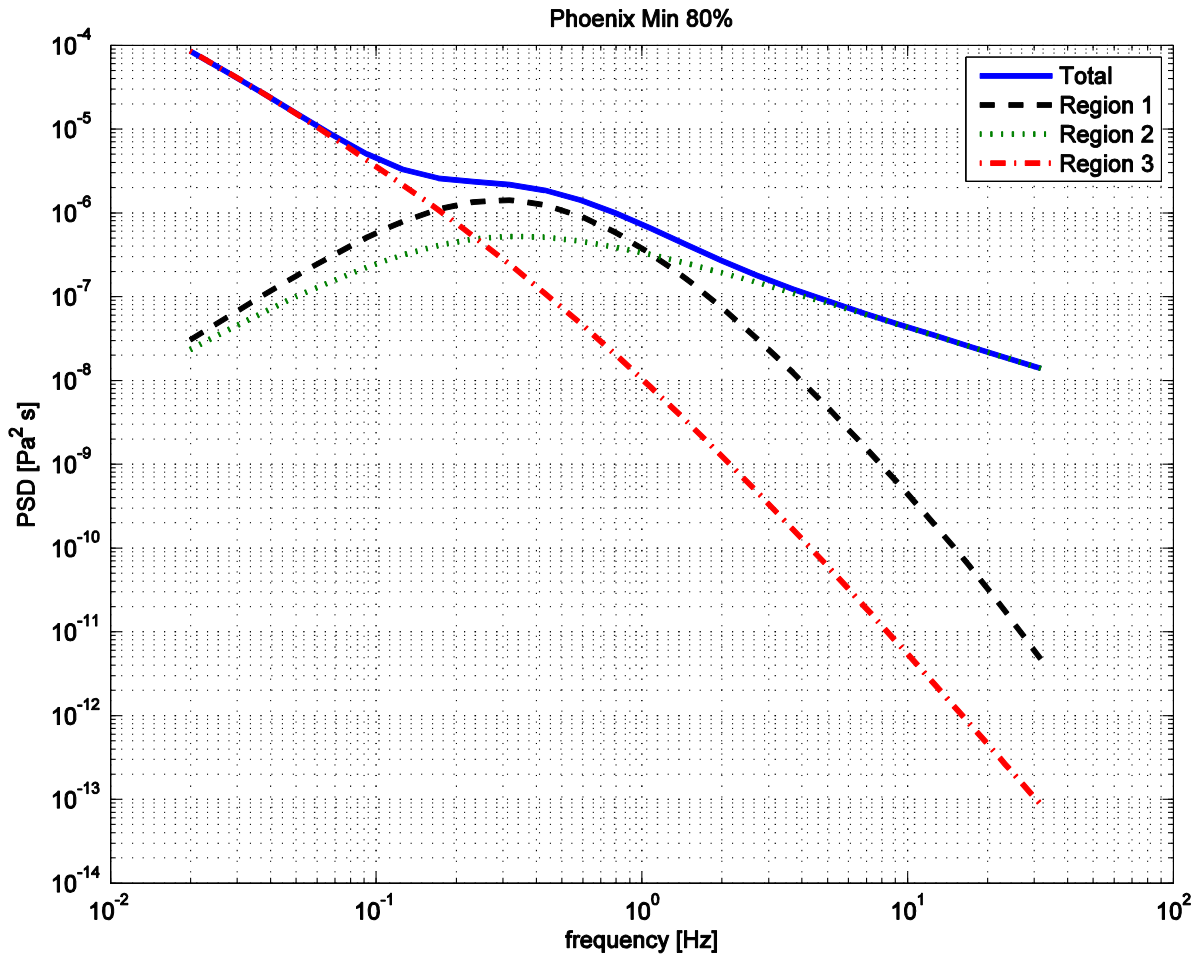


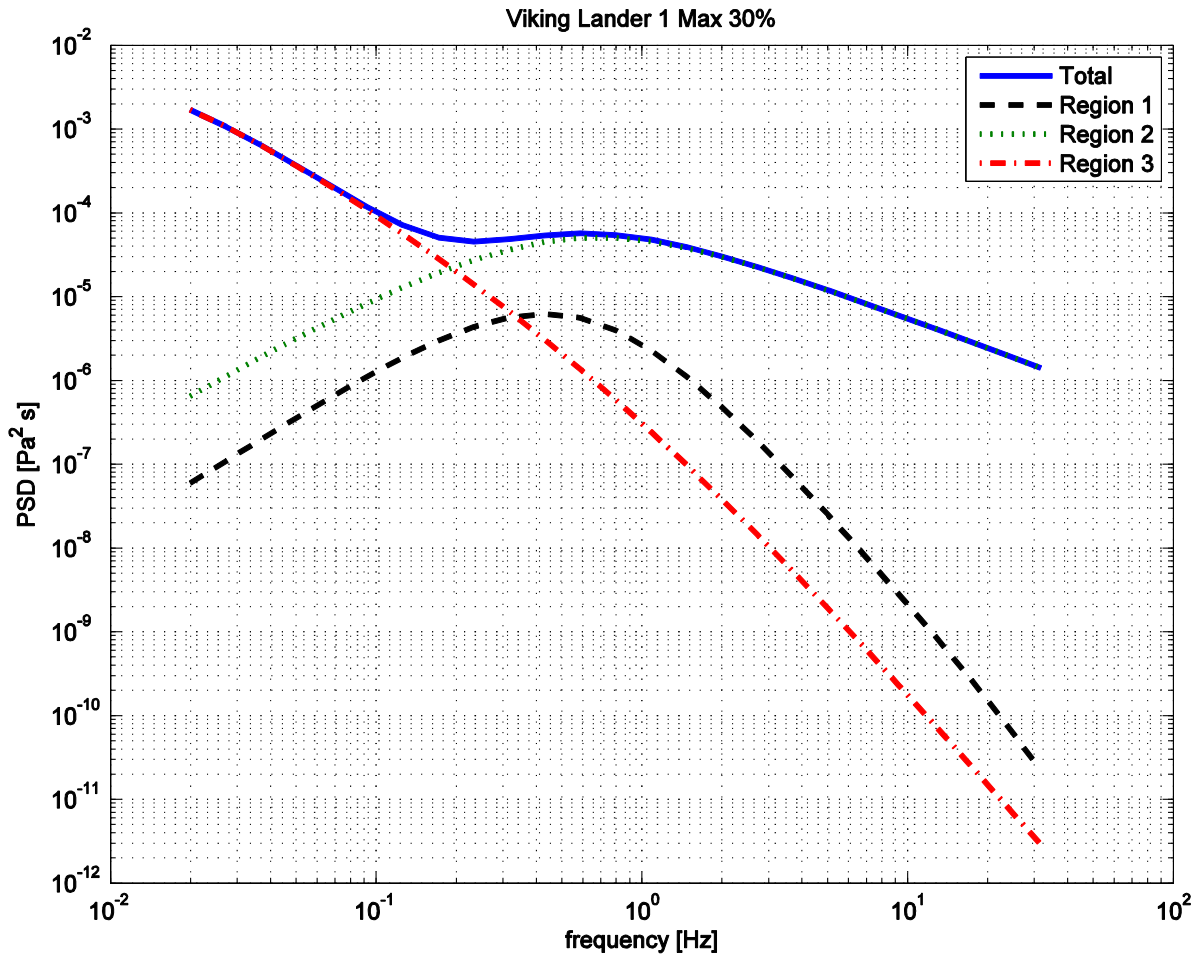


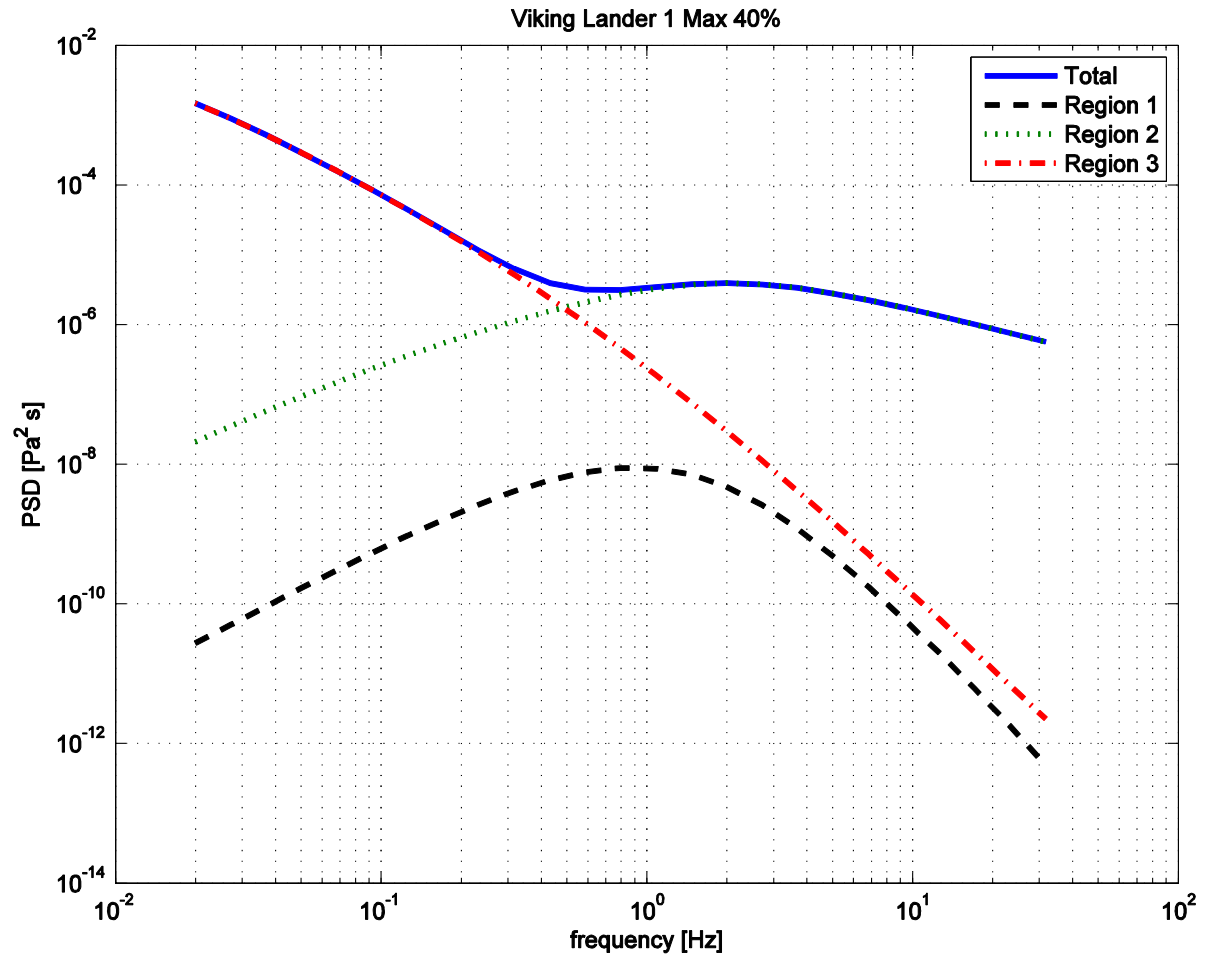




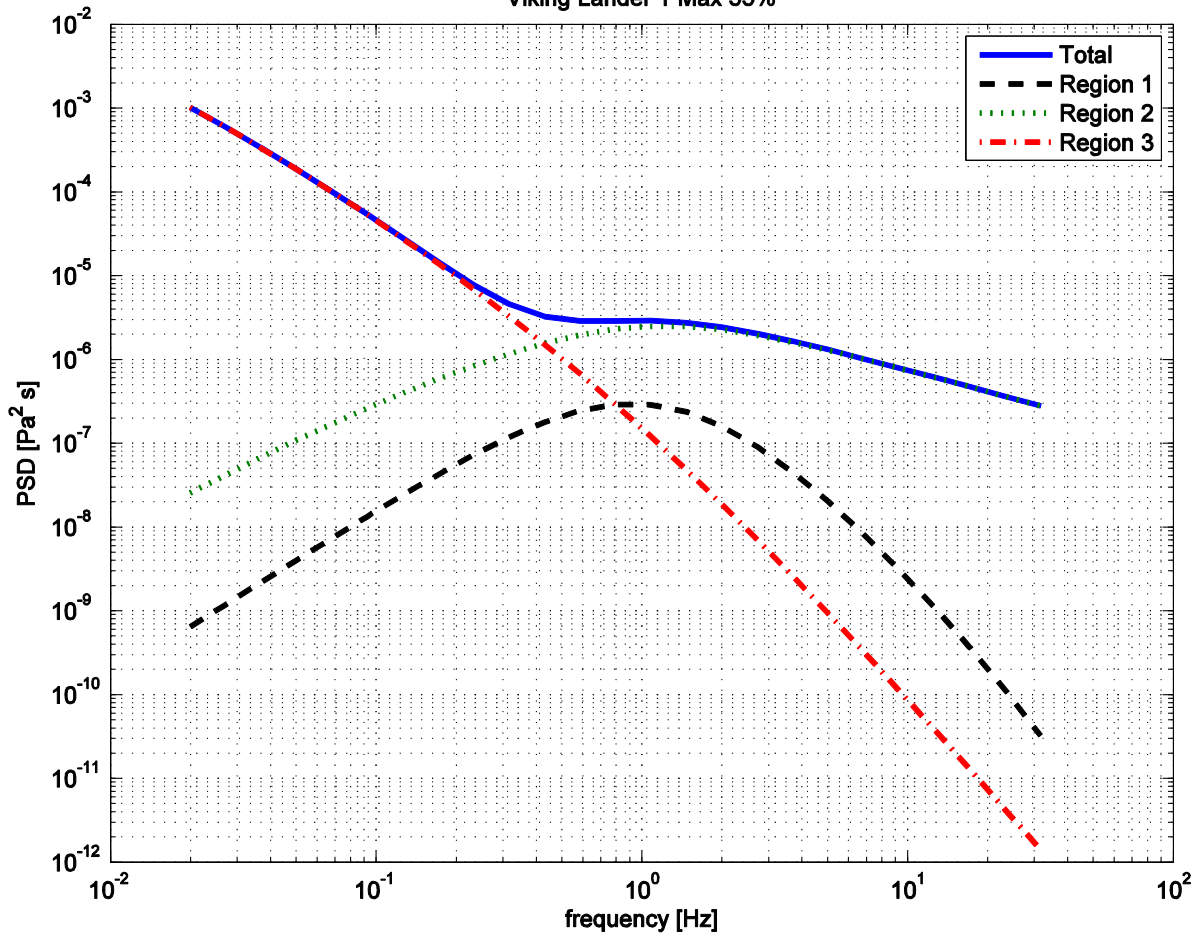


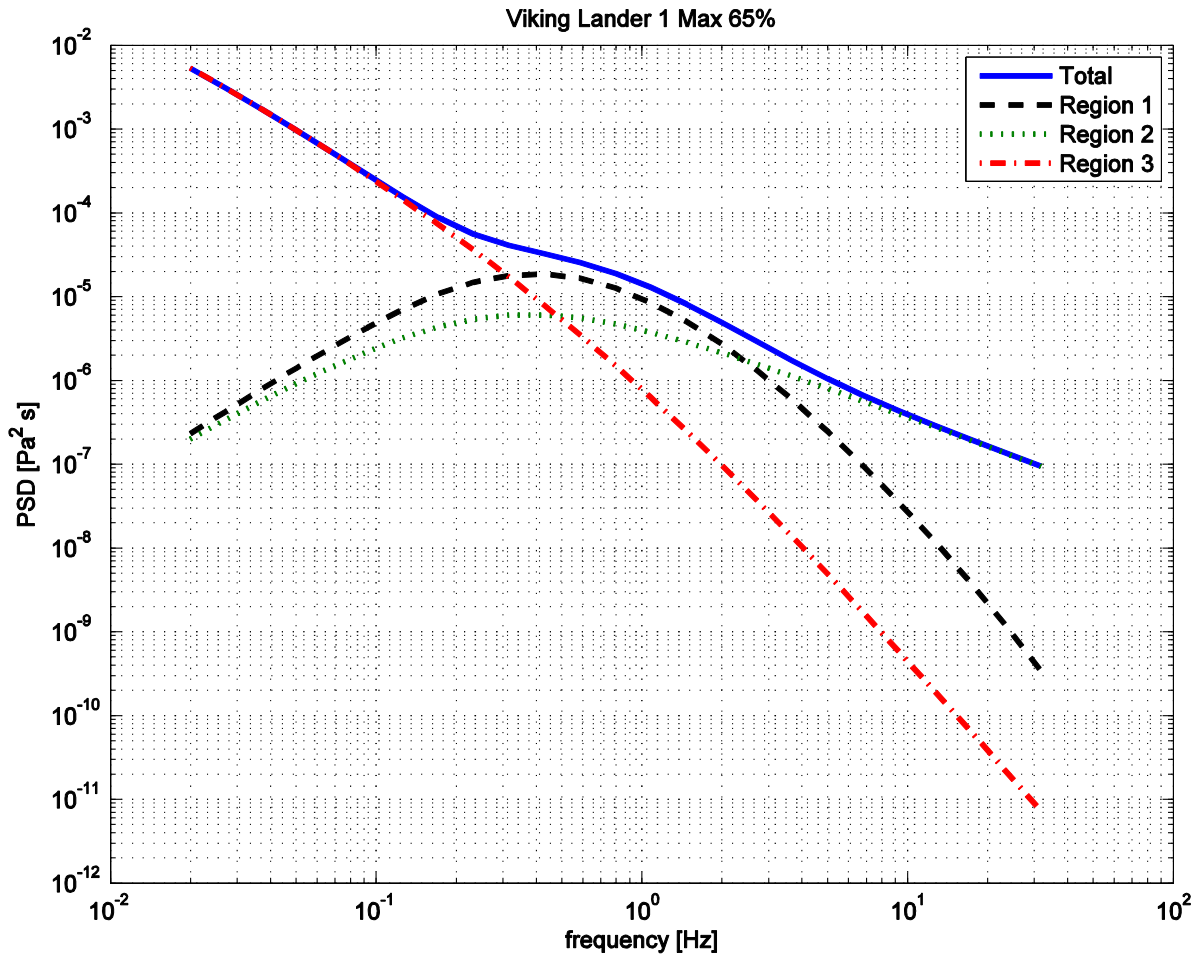


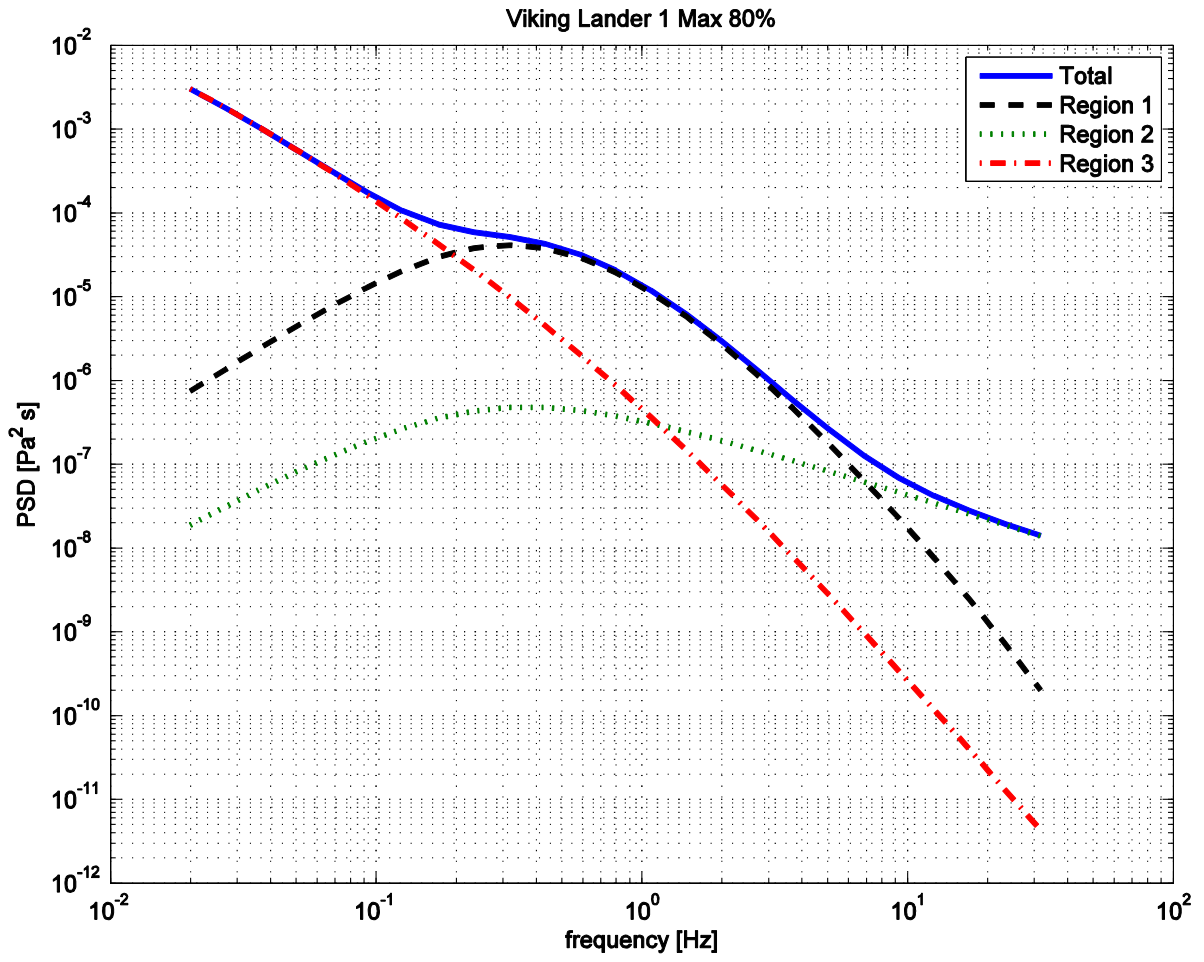


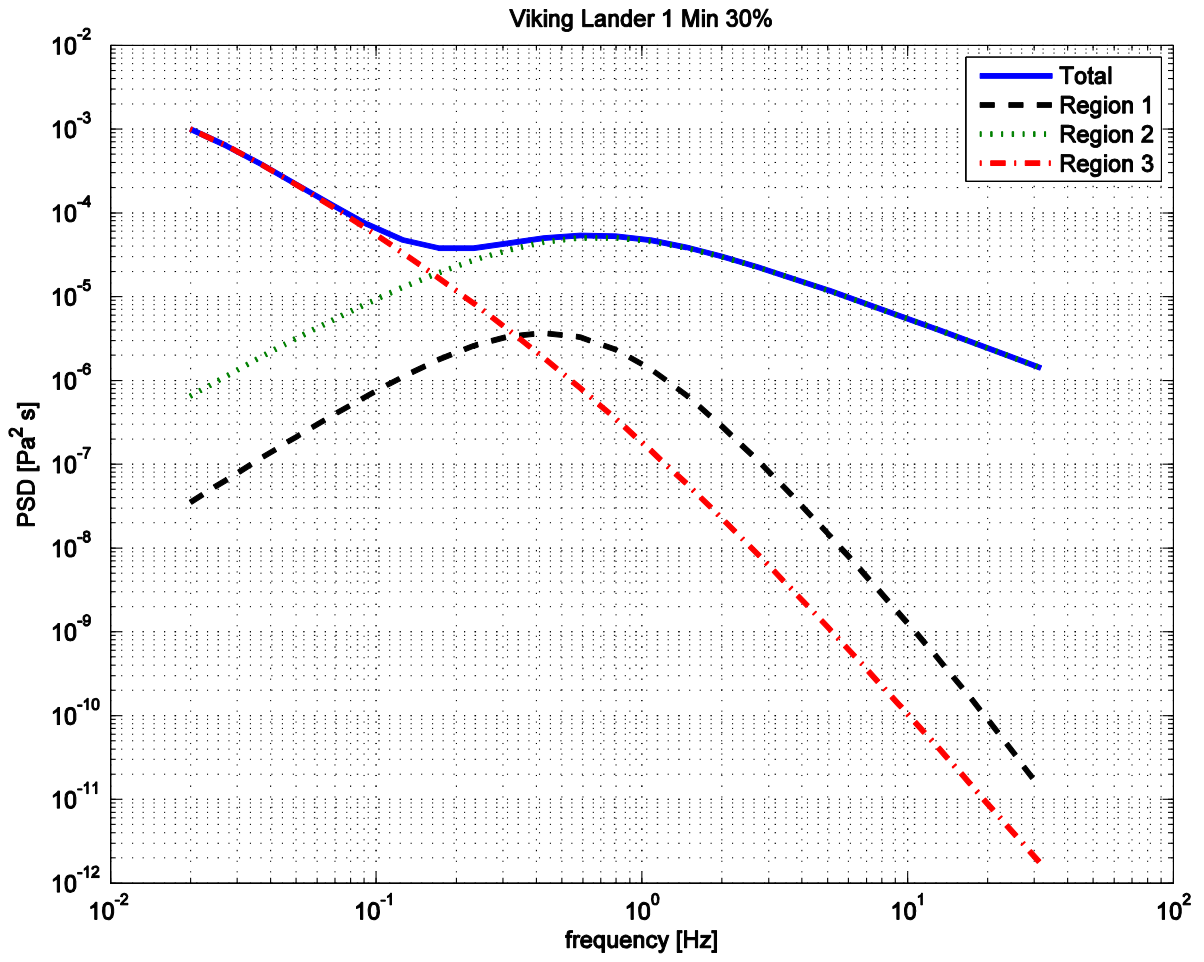


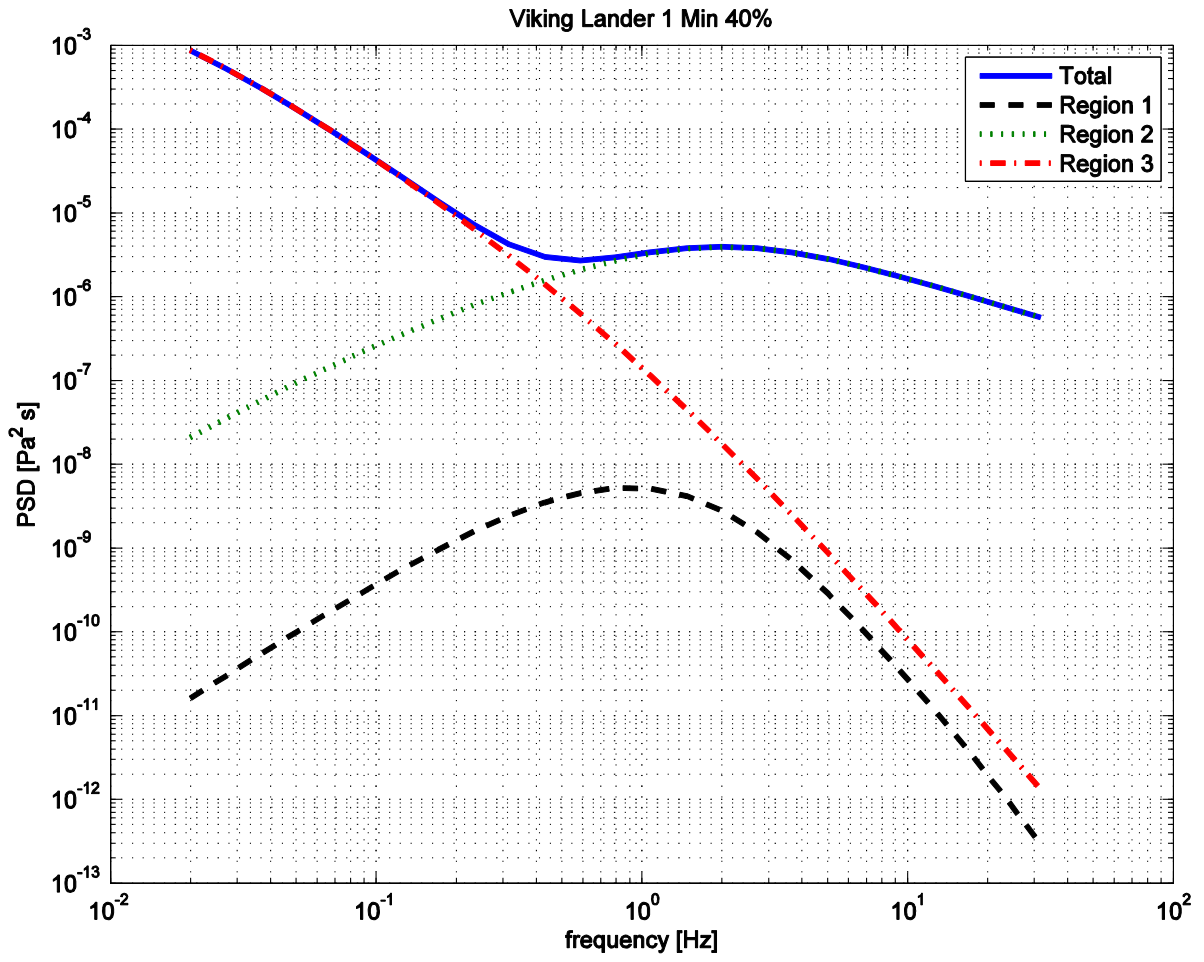
Viking Lander 1 Max 55%

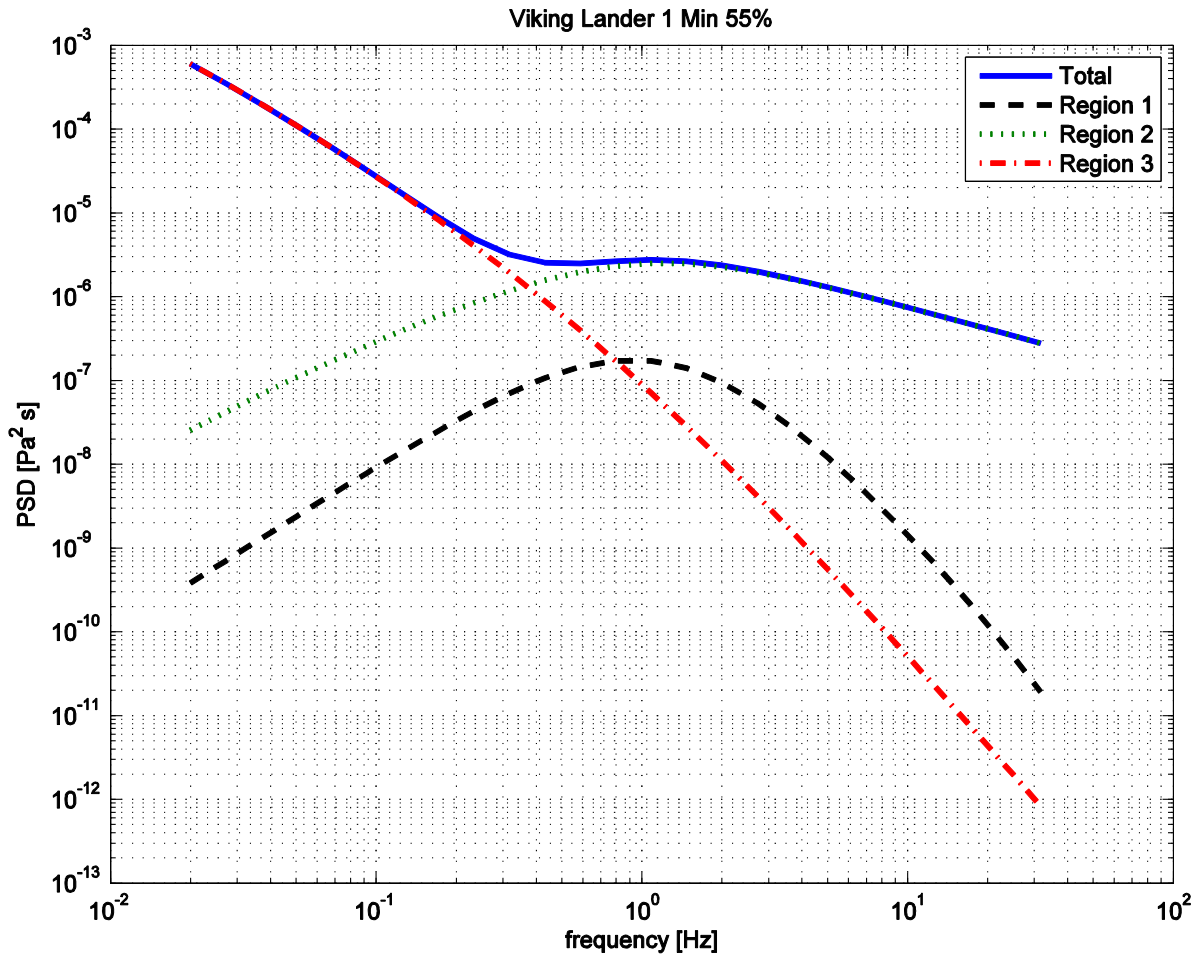


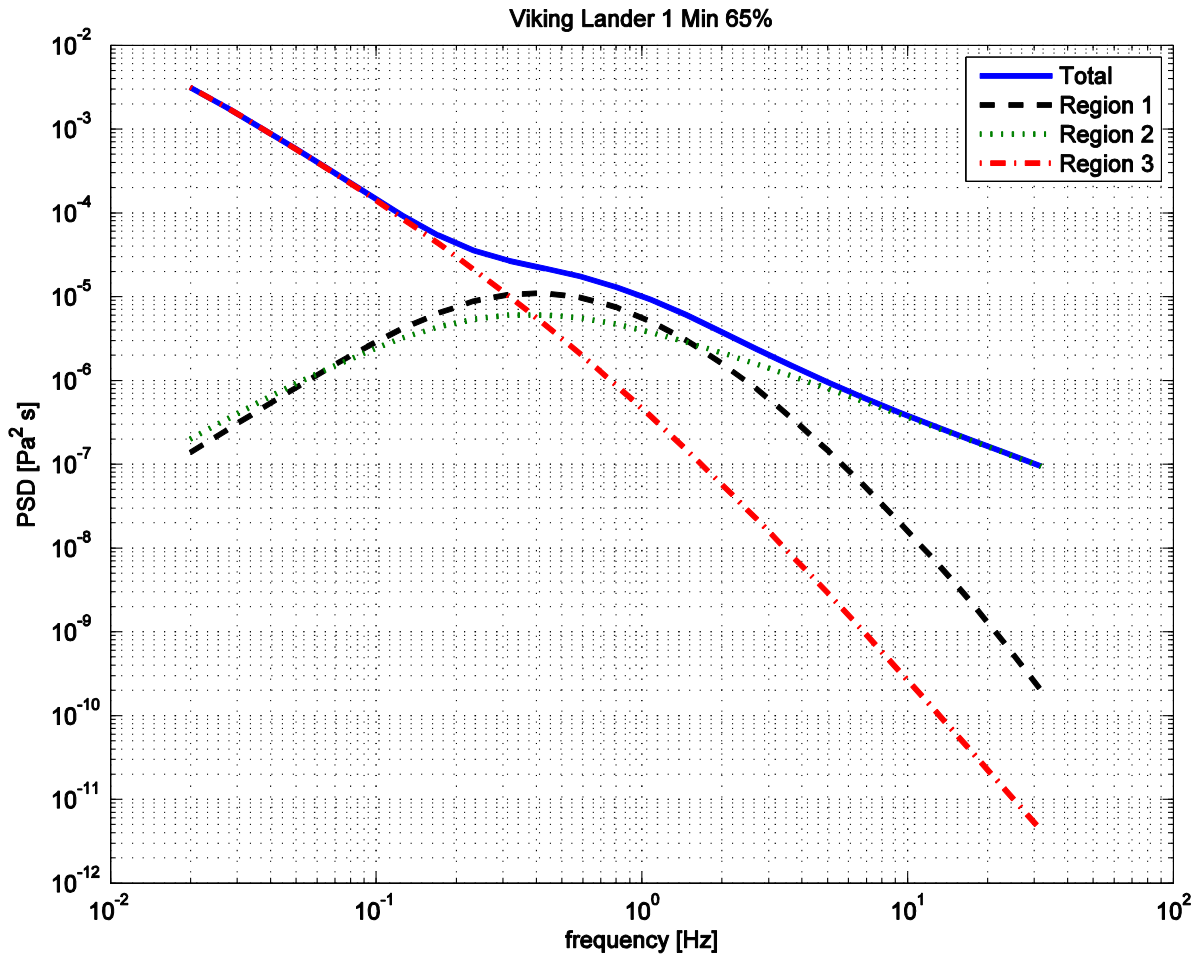


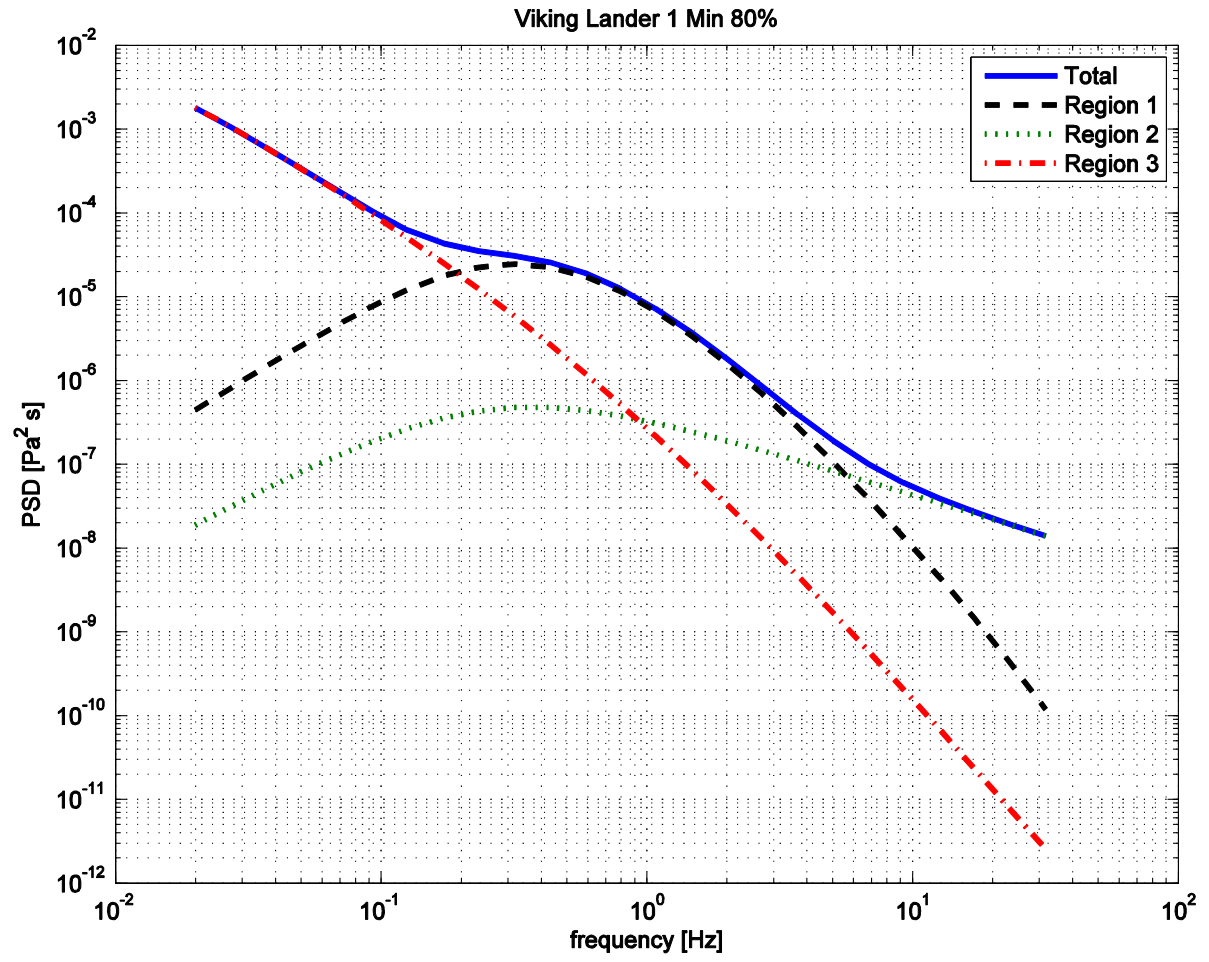


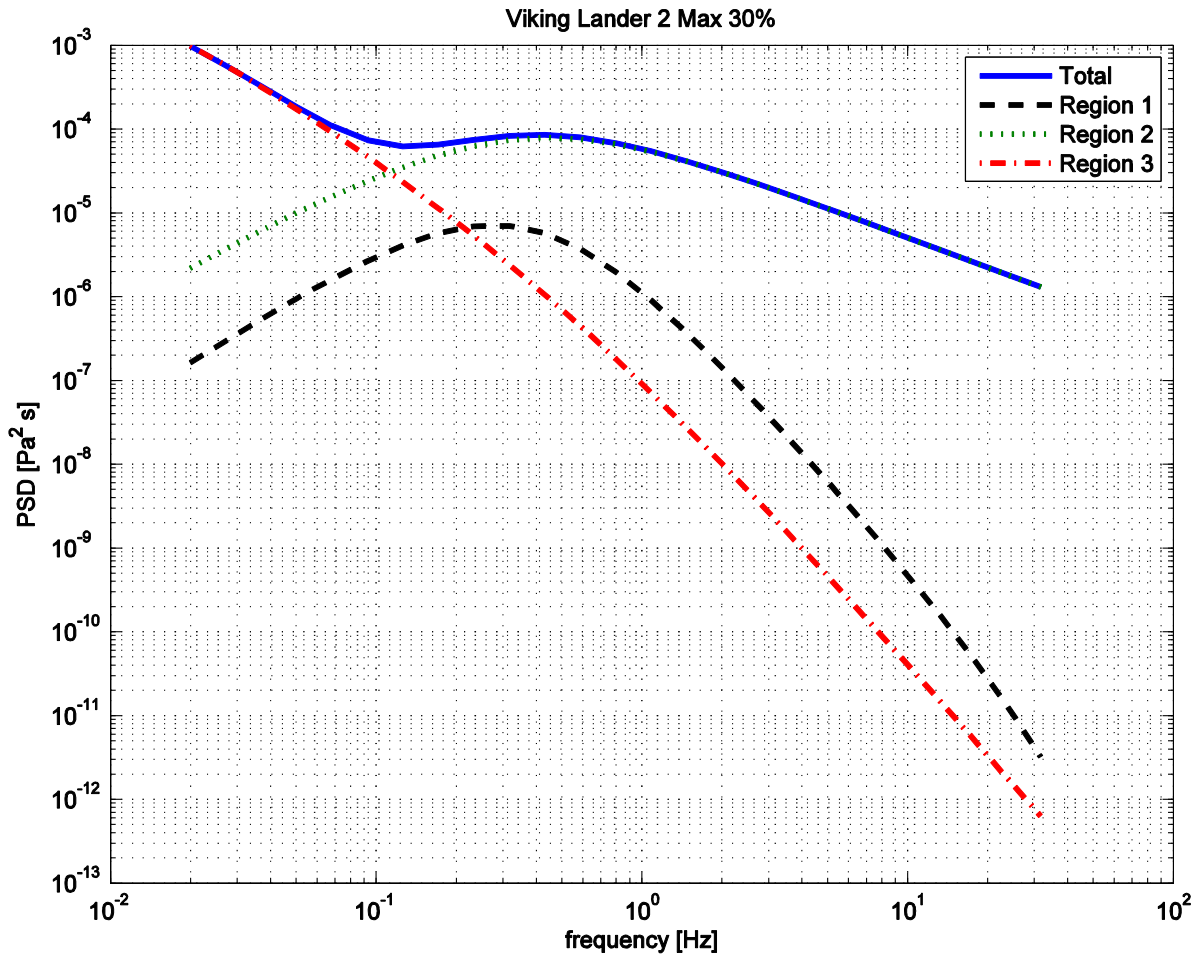


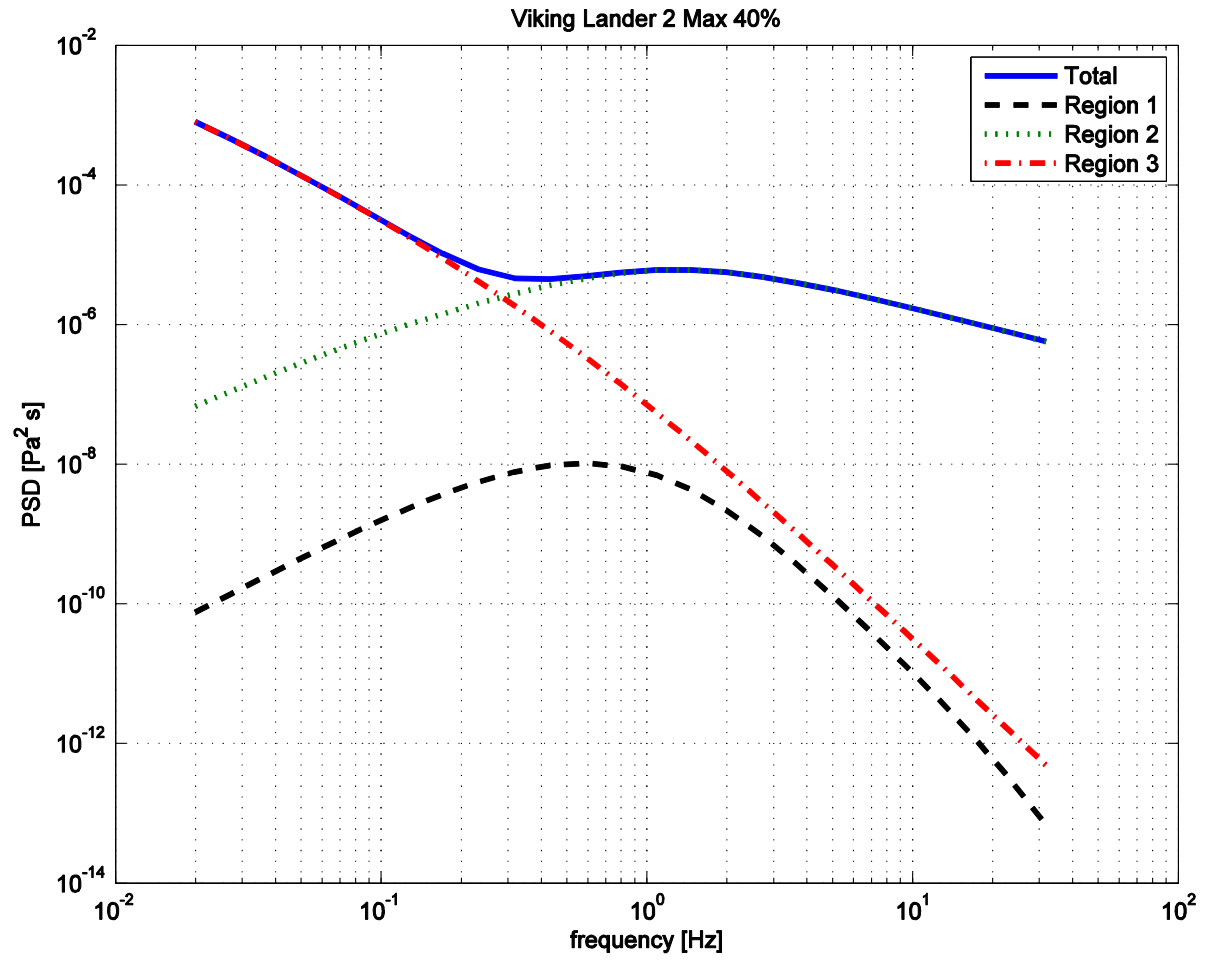




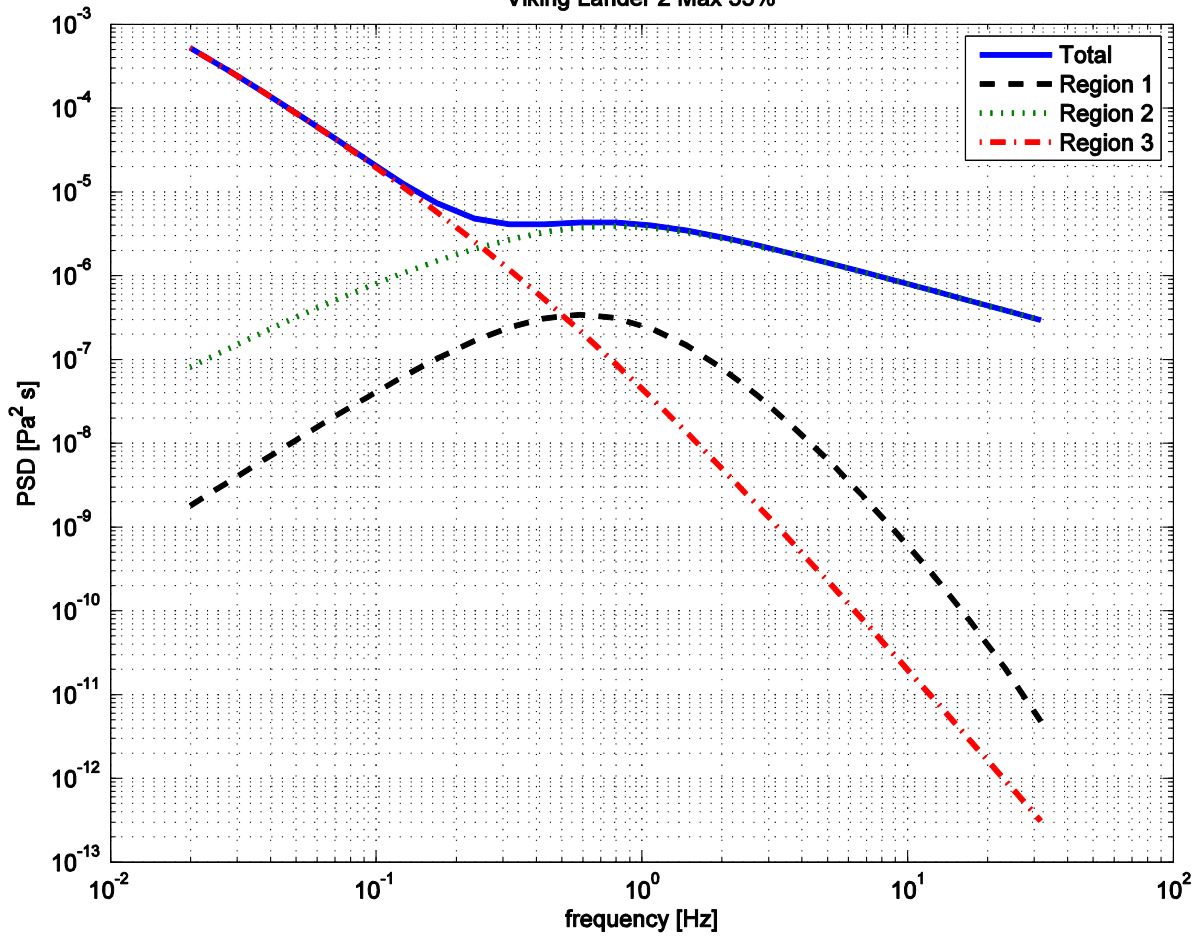




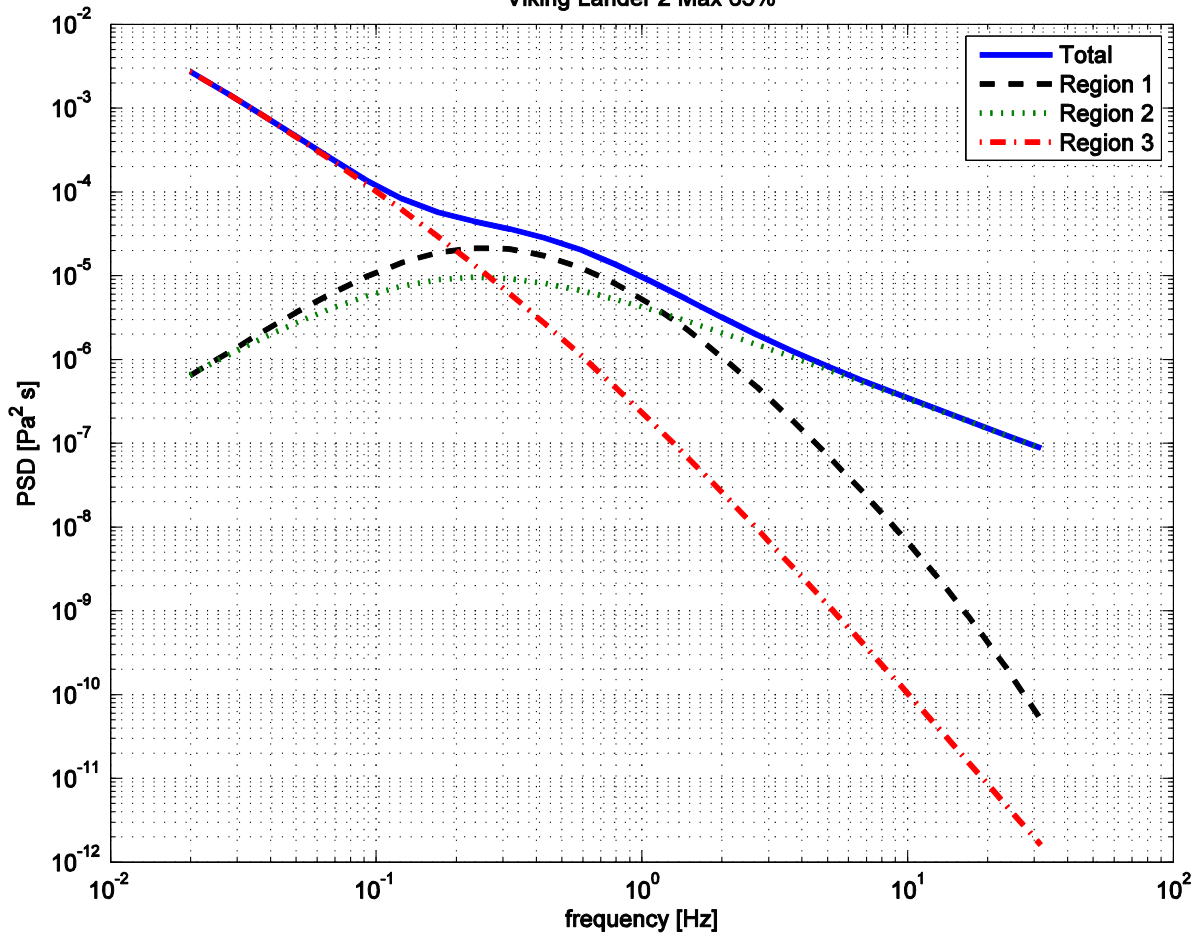


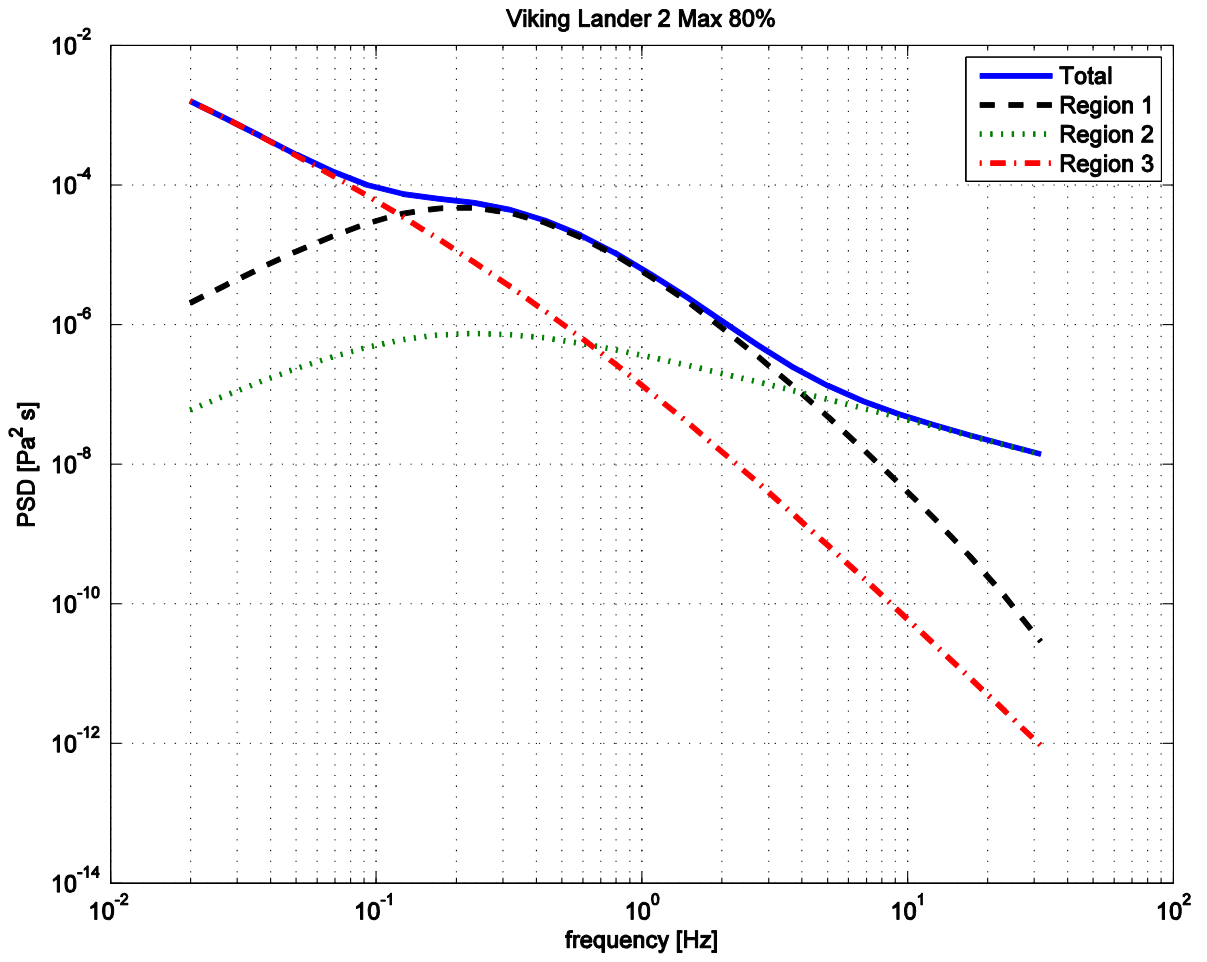


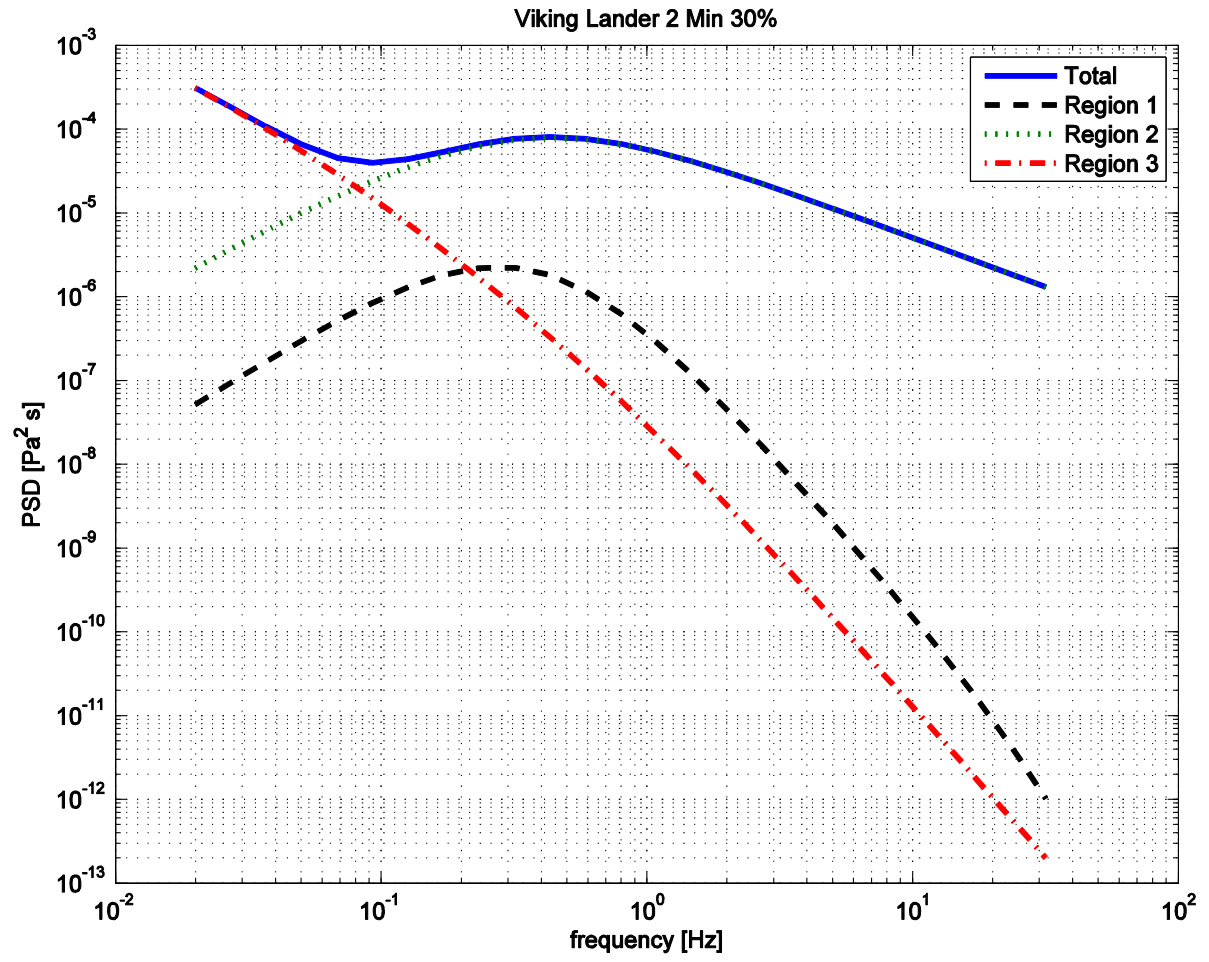
Viking Lander 2 Max 55%

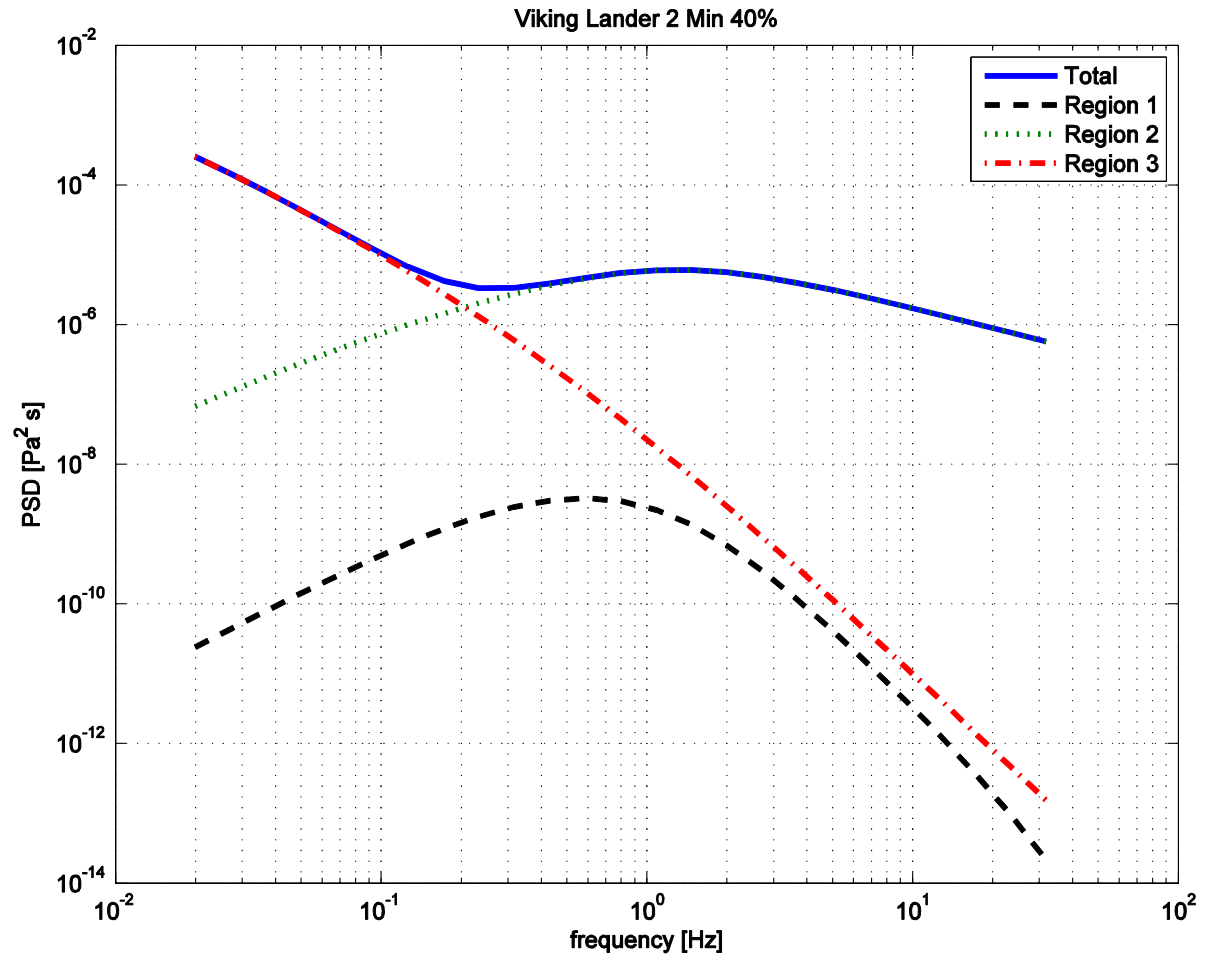


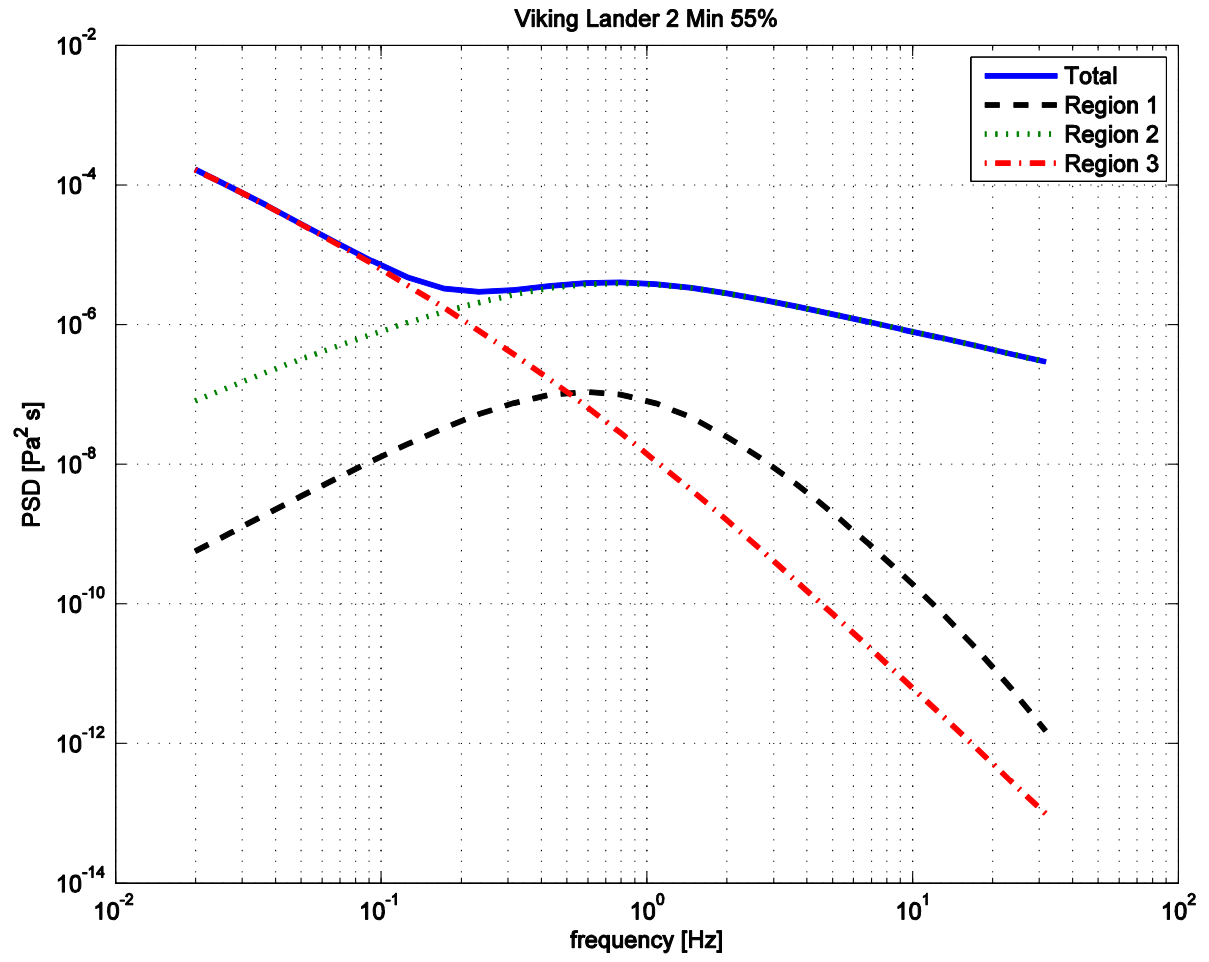
Viking Lander 2 Max 65%

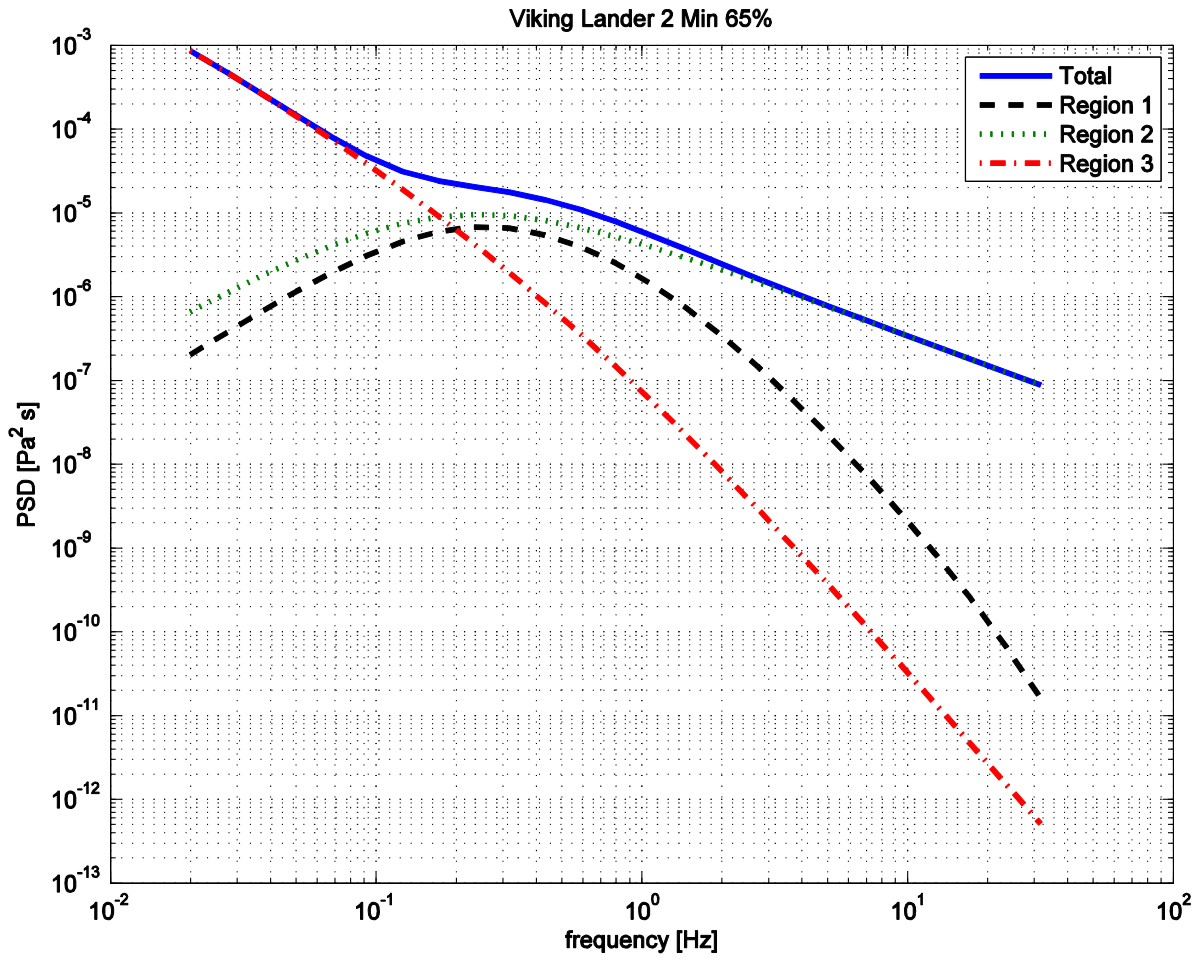


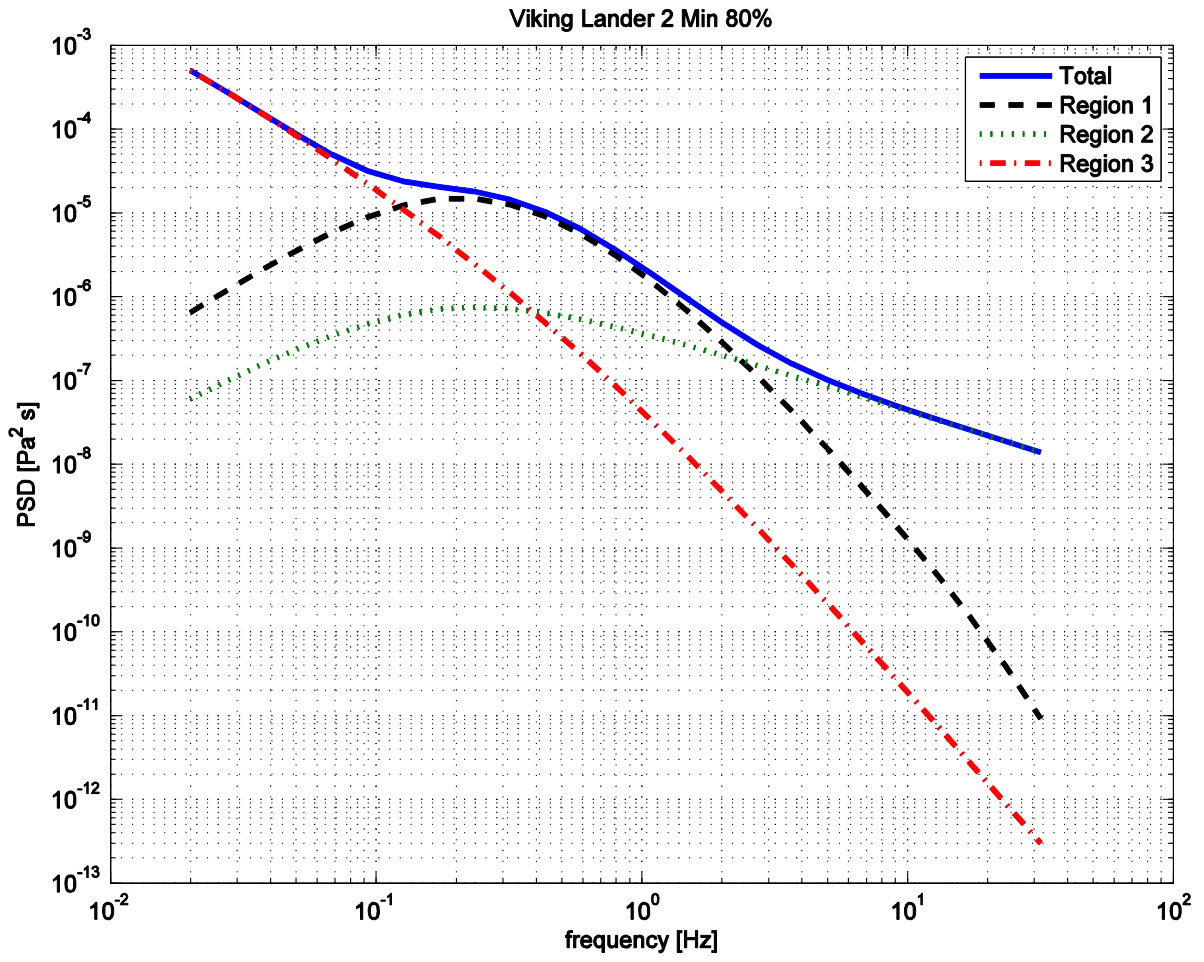












Pitre, Kevin M. Bachelor of Science, University of Louisiana at Lafayette, Fall 2011; Master of Science, University of Louisiana at Lafayette, Fall 2016

Major: Physics

Title of Thesis: Predicting Wind Noise Inside Porous Dome Filters for Infrasound Sensing on Mars

Thesis Director: Dr. Andi Petculescu

Pages in Thesis: 109; Words in Abstract: 298

ABSTRACT

The study described in this thesis aims to assess the effects of wind-generated noise on potential infrasound measurements on future Mars missions. Infrasonic sensing on Mars is being considered as a means to probe the long-scale atmospheric dynamics, thermal balance, and also to infer bolide impact statistics. In this study, a preliminary framework for predicting the principal wind noise mechanisms to the signal detected by a sensor placed inside a hemispherical porous dome on the Martian surface is developed. The method involves calculating the pressure power density spectra in the infrasonic range generated by turbulent interactions and filtered by dome shaped filters of varying porosities. Knowing the overall noise power spectrum will allow it to be subtracted from raw signals of interest and aid in the development of infrasound sensors for the Martian environment. In order to make these power spectral predictions, the study utilizes the Martian Climate Database (MCD) global circulation model, developed by Laboratoire de Meteorologie Dynamique in Paris, France. Velocity profiles are generated and used in semi empirical functions generated by

von Kármán along with equations for describing the physical turbulent interactions. With these, turbulent interactions in the free atmosphere above the Martian surface are described. For interactions of turbulence with the porous filter, semi-empirical formulations are adapted to the Martian parameters generated by the MCD and plotted alongside contributions in the free atmosphere outside and inside the dome to obtain the total wind noise contribution from turbulence. In conclusion, the plots of power spectral densities versus frequency are analyzed to determine what porosity filter would provide the best wind-noise suppression when measured at the center the dome. The study shows that 55% (0.02 to 5 Hz) and 80% (6 to 20 Hz) porosities prove to be the better of the five porosities tested.

Biographical Sketch

Kevin Pitre was born on July 14, 1989. He was raised by Louis and Monica Pitre and has spent his life residing in south Louisiana. Here, he attended North Vermilion High School in Leroy, Louisiana, where he attained his high school diploma and then went on to study Industrial Technology at the University of Louisiana at Lafayette, where he received his Bachelor of Science in 2011. After graduating in 2011, he was employed by Halliburton Energy Services as a field engineer. In the fall of 2015, he gained acceptance to the Master of Physics program at the University of Louisiana at Lafayette.